BIODEGRADABLE ENZYMATICALLY ACTIVATED NANOPROBES

FOR DUAL IMAGING AND THERAPY OF BREAST CANCER

by

Tugba Yildiz, B.S., M.S.

A dissertation submitted to the Graduate Council of
Texas State University in partial fulfillment
of the requirements for the degree of
Doctor of Philosophy
with a Major in Materials Science, Engineering, and Commercialization
August 2017

Committee Members:

Tania Betancourt, Chair

Gary W. Beall

Jason Cook

Jennifer A. Irvin

Shannon E. Weigum

FAIR USE AND AUTHOR'S PERMISSION STATEMENT

Fair Use

Duplication Permission

DEDICATION

To my grandmother, mother, father, brother, love, and advisor.

For your constant support and love.

ACKNOWLEDGEMENTS

First and foremost, I would like to thank my advisor Dr. Tania Betancourt for her constant support, encouragement, guidance, and patience during my PhD studies. I appreciate all her contributions of time, ideas, and approach to make my Ph.D. experience productive and stimulating. I've learned lots of things that I wouldn't have imagined over the past three years from her. She is not only a good professor, but also a great mentor, and friend to me. The energy, enthusiasm and joy she has for her research was contagious and motivational for me, especially tough times in my Ph.D. I am also thankful for the excellent example she has provided as a successful woman chemical engineer and professor. I could not wish for a better or friendlier supervisor.

I would like to thank Dr. Gary Beall and Dr. Thomas Myers for encouraging me to apply to MSEC Program and trusting me to complete it at the beginning of my PhD journey. I am very thankful for the support, guidance, time, interest, and helpful comments of Dr. Jennifer Irvin and Dr. Shannon Weigum who gave me during my PhD. I feel lucky to have them in my committee. I would also thank to Dr. Jason Cook for his time to be in my committee, giving helpful feedback on my research, giving me an opportunity to work in NanoHybrids as an intern and taught new approaches in the field. I am also thankful to Dr. Mary Jane Patterson for being a great laboratory coordinator during my teaching experience.

I would like to thank Karla Pizana in MSEC and Maria Elena Martinez in Chemistry & Biochemistry for helping me all time and their kindness. I also want to thank

the students in the Betancourt research group, Janet Vela Ross, Gabriela Herrera, Madeline Huff, Travis Cantu, Karolyn Barker, Cally Moore, Jose Dominguez, Ron Hall, and, Kyle Walsh for their friendships as well as good advice and collaboration. I would also like to thank the students and researchers Edith De Leon, Hyunhwan Kim, Devanda Lek, Anwar Siddique, Pulin Patel, Zhenze Zao, and Shiva Rastogi for their contributions.

I would also like to my lifelong friends who I love forever; Reycan Cantas Cakir, Yasemin Asik, Zeynep Gultekin, Betul Sen Gumus. Texas has brought great people in my life; Esperanza Baltazar, Ma Elena Martinez, Esra Satici, Shahrzad Ahangar, Eda Baykal-Caglar, and Ebru Gencturk. I will never forget their friendship and constant support. I am also thankful for being a part of the University of Texas at Austin Middle Eastern Ensemble (Bereket) and my all great musician friends. Music helped me healing and stood up again during my last year in Texas. It is one of the most important things in my life and it is going to be with me all my life. I am thankful my parents to transfer this gifted gene to me.

I want to thank my grandmother Vesile Onar for taking care of me during my childhood. Thank you for being wonderful listener, teacher, mom, father, friend, and my everything. I feel your absence in depth of my soul every day. I want to thank my parents Suzan and Ali Hidir Yildiz, and my brother Emrah Savas Yildiz with all my heart for their continuous support and love. Thanks to the rest of my family for their thoughts and encouragement.

Finally, I want to thank my loving, supportive, encouraging, and patient soulmate Sercan Gungor. Thank you for encouraging and believe in me to do the best I can in every way. I feel so lucky to have you in my life.

TABLE OF CONTENTS

Page

LIST OF TABLES

Table **Page**

LIST OF FIGURES

Figure **Page**

ABSTRACT

Breast cancer is the most commonly diagnosed cancer in women and the second leading cause of cancer deaths in women worldwide. Near infrared optical imaging has emerged recently as a viable alternative for the detection, monitoring, and image-guided therapy of tumors. Enzymatically activated nanoprobes utilize protease-labile polypeptides labeled with near infrared fluorophores as a mean to provide an off-to-on switch for fluorescence development that is triggered by tumor-overexpressed enzymes. Clinical use of doxorubicin is restricted by dose-dependent toxicity, multidrug resistance, and low specificity against cancer cells. Theranostic nanoprobes integrate diagnostic and therapeutic functions within an all-in-one platform.

In this work, theranostic nanoprobes were synthesized with commonly used biocompatible and biodegradable polymers, and was used as cancer contrast and therapeutic agents for optical imaging and treatment of breast cancer. These core-shell structure nanoprobes were prepared with blends of biodegradable and biocompatible amphiphilic copolymers, poly(lactic-*co*-glycolic acid)-*b*-poly(L-lysine), and poly(lactic acid)-*b*-poly(ethylene glycol). The protease cleavable polypeptide, poly(L-lysine), was decorated with the near infrared fluorescent molecule AlexaFluor-750 for optical imaging of breast cancer cells. The chemotherapeutic drug doxorubicin was loaded into the core of nanoprobes for drug delivery.

I. INTRODUCTION

1.1 Motivation

Despite great progress in prevention, detection, and treatment modalities during last couple of decades, cancer remains one of the most common and deadly diseases worldwide, and is the second leading cause of mortality of all Americans.[1] Breast cancer is the most commonly diagnosed cancer in women and the second leading cause of cancer deaths in women worldwide.[2] Specifically, breast cancer represents 30 % of all new cancer cases in the United States.[3] The American Cancer Society estimates that in the U.S. in 2017 there will be approximately 255,710 new cases of breast cancer and approximately 40,610 people will die of this disease. Cancer medical costs were estimated to reach $124.6 billion in 2010, with the highest costs ($16.5 billion) being associated with breast cancer.[4] According to the National Institutes of Health, medical expenses for cancer in the U.S. are projected to hit at least $158 billion in the year 2020.[4]

The most common cancer treatment methods for breast cancer are surgery, chemotherapy, radiation therapy, hormone therapy, or antibody-based therapy. The preferred treatment for breast cancer is surgery followed by chemotherapy. Chemotherapy is most effective when combinations of more than one drug are used. The most common chemotherapeutic drugs used for early breast cancer are anthracyclines (doxorubicin and epirubicin) and taxanes (paclitaxel and docetaxel).[5] Chemotherapeutic drugs affect both tumor and normal cells as well. Due to unspecific drug delivery to all tissues, including healthy ones, chemotherapy often causes systemic toxicity-related side effects. Further, half of all chemotherapy patients develop drug resistance, a situation that also leads to treatment failure.[6] For this reason, efforts to develop alternative chemotherapy treatments

have focused on designing nano-scaled agents that are more specific against cancer cells to minimize toxic side effects and improve therapeutic efficacy.[7–10] The use of nanosized agent enhances tumor selectivity via passive and active targeting.[11] Nanosized agents can reach a given tissue, organ, or cell by the virtue of their intrinsic properties, such as particle size or hydrophobicity vs. hydrophilicity via passive targeting.

The *in vivo* detection of tumors, particularly in early disease stages, is important for effective treatment. Cancer can be diagnosed and monitored by noninvasive molecular imaging techniques, including those based on optical imaging.[12] Optical imaging offers many advantages over other imaging techniques. Because optical imaging is much safer and considerably simpler, it can be used to monitor the progression of cancer and the effectiveness of treatment over time.

Nanoparticles are considered as the future of medicine, allowing for less invasive imaging, detection, and therapy for several diseases. The combination of therapeutic and diagnostic agents within a single nanoscale "*theranostic*" platform offers a significant potential to make personalized nanomedicine a clinical reality for cancer patients.[13] The biodistribution, pharmacokinetics, and tumor accumulation of theranostic nanoparticles could be monitored while at the same time enabling a therapeutic response and obtaining information about the biological characteristics of the tumor tissue (protease overexpression for example which is known to be related to the tumor aggressiveness and therapeutic outcome). Clinicians could then make decisions about dosage, frequency, drug choice, and treatment strategies by tracking therapeutic responses.

1.2 Overall Research Project

Theranostic nanoparticles integrate diagnostic and therapeutic functions within an all-in-one platform. In this work, the research focuses on a theranostic system development that will enable more effective treatment and monitoring of tumor tissue coupled with chemotherapy. Specifically, a novel formulation of theranostic nanoprobes (NPs) can be easily synthesized with commonly used biocompatible and biodegradable polymers, and can be controlled to provide imaging contrast and exert a therapeutic effect to treat breast cancer. *The central hypothesis of this research is that the use of theranostic NPs to improve the tumor targeting and payload of the imaging and therapeutic agents to tumors, combined with the cancer specific enzyme-triggered development of near infrared (NIR) fluorescence signal and chemotherapeutic drug delivery can significantly improve the detection and treatment of tumors.*

In this work, NPs with a core-shell structure (Figure 1-1) were prepared by nanoprecipitation of amphiphilic block copolymers. The hydrophobic core is used to load the chemotherapeutic agent doxorubicin free base (DOX) for drug delivery. The core was made of the biodegradable and biocompatible polymers poly(lactic-*co*-glycolic acid) (PLGA) and poly(lactic acid) (PLA). The surface of the NPs contained the hydrophilic polymers poly(ethylene glycol) (PEG) and a protease-specific polypeptide such as poly-L-lysine (PLL). The polypeptide was used as a site for conjugation of NIR fluorescent molecules for imaging of tumor cells. The enzymatically cleavable polypeptide PLL was covalently decorated with the near infrared (NIR) fluorescent molecule AlexaFluor-750 (AF750). The close-packed NIR fluorescent molecules self-quenched one another. However, these molecules became fluorescent when PLL chains were cleaved

enzymatically by tumor proteases.[14] Two types of PEG polymers were used on the surface of the NPs. PEG-OMe was used for stabilizing of NP suspensions, preventing adsorption of plasma proteins, and minimizing recognition of the NPs by the immune system. PEG-COOH will be used to provide a site for covalently binding anti-HER2 (human epidermal growth factor receptor 2) aptamer to the NPs in future studies.

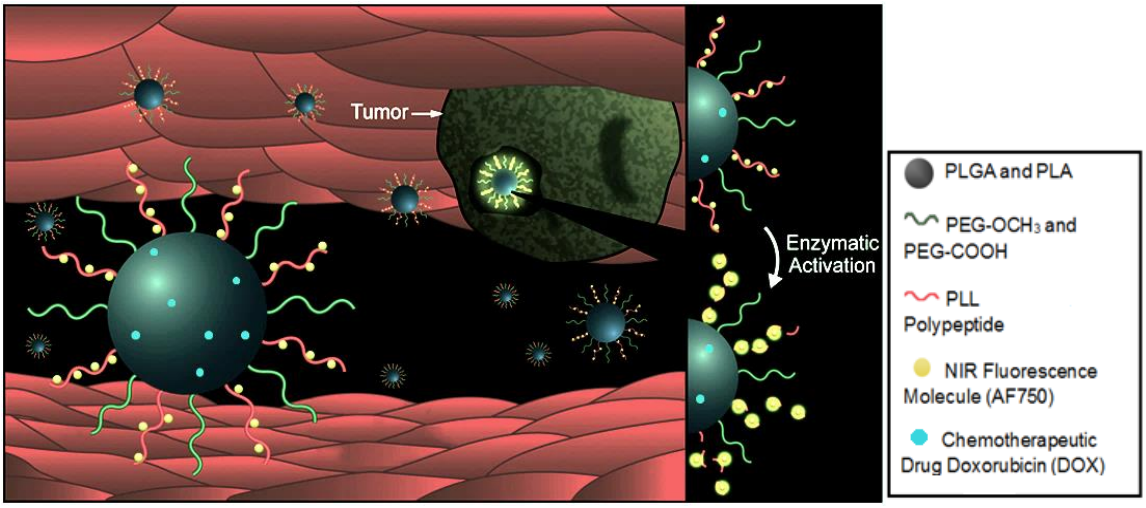

Figure 1-1. General structure of the NPs and its function as a contrast and therapeutic agents. The NIR fluorescent AF750 molecules are initially quenched due to close packing. These molecules became fluorescent when PLL chains were cleaved enzymatically by tumor-overexpressed proteases. Abbreviations: PLGA, poly(lactic-co-glycolic acid); PLA, poly(lactic acid); PEG, poly(ethylene glycol); PLL, poly-L-lysine; AF750, Alexa Fluor 750.

1.3 Specific Aims

The following aims were completed in this project:

1. **Design and synthesize NPs for drug delivery and NIR fluorescence development.**

   NPs were prepared by nanoprecipitation of biodegradable and biocompatible amphiphilic block copolymer blends. The hydrophobic core of NPs was used as carrier of the chemotherapeutic drug. The hydrophilic surface of NPs contained enzymatically cleavable tumor-specific polypeptides that provided tumor-triggered NIR fluorescence

development. The size, morphology, zeta potential, and drug loading within the nanoparticles were determined. The rate and pattern of drug release and NIR fluorescence enhancement upon activation by tumor-specific proteolytic enzymes were studied.

2. ***In vitro* studies to demonstrate the cytocompatibility and theranostic potential of the NPs.** The cytocompatibility of drug-free NPs was evaluated using the luminescence and MTT assays for cell viability. The therapeutic efficacy of DOX-loaded NPs was investigated with a luminescence assay to prevent interference from DOX absorption. Finally, the interaction of the NPs with the cells was studied with the purpose of evaluated the potential to use the NPs as NIR fluorescent optical imaging agents and drug delivery carriers.

1.4 Dissertation Outline

Chapter 2 describes background relevant to the imaging and drug delivery aspects of this work. Chapter 3 describes our previously published work[14] on the polymer synthesis and characterization, the preparation and characterization of nanoparticles used as imaging agent and *in vitro* imaging studies. Chapter 4 describes the preparation and characterization of chemotherapeutic agent doxorubicin-loaded NIR imaging agent-labeled nanoparticles (theranostic) and *in vitro* evaluation on breast cancer cells. Finally, Chapter 5 summarizes the work of the previous chapters and explores the future potential of this research.

II. BACKGROUND

2.1 Nanoparticles in Diagnostic and Treatment Applications

Nanomedicine is a rising discipline that encompasses a broad area of diagnostic, imaging, drug delivery, targeting, and therapeutic strategies that utilize nano-scaled materials. Clinically relevant examples of such nano-sized carrier materials and nanodevices are polymeric nanomaterials, liposomes, quantum dots, magnetic and gold nanoparticles, carbon nanotubes, and many more.[15] These nanomaterials typically range from 10 to 500 nm, which makes them over 100-fold smaller than cells.[16]

Nanoparticles can be used therapeutically as drug carriers in which the therapeutic agent is dissolved, entrapped, encapsulated, adsorbed, or chemically attached. Nanoparticles also enable non-invasive administration routes such as oral, nasal, and ocular. Nanoencapsulation of therapeutic drug increases drug efficacy, specificity, and tolerability.[17] In addition to therapeutic applications, nanoparticles are being used for noninvasive imaging, for early cancer detection, and for visualizing various important aspects of the drug delivery process.[15,16]

An ideal design of nanoparticles can allow pharmacokinetic and optical tuning, and minimize the chances of side effects. Although a variety of novel nanomaterials have been developed, clinical applications of many of them are absent due to many clinical concerns and a lack of understanding of their toxicity and elimination.[18]

Polymeric nanoparticles in medicine are one of the most studied organic strategies that can transform the current therapeutic, diagnostic, and biological challenges to more effective and reliable solutions. Polymers in therapeutic applications have design flexibility based on functionalization, macromolecular synthesis methods, and polymer diversity.

Polymer-based drug delivery systems can be tailored based on the features such as polymer composition, solubility, crystallinity, molecular weight, backbone stability, hydrophobicity and polydispersity for best interaction with the physiochemical properties (molecular weight and charge for example) of a specific cargo.[19–21]

One of the most commonly used polymers for drug delivery and imaging applications is poly(lactic-co-glycolic acid), PLGA, which is a polyester copolymer of lactic acid and glycolic acid. PLGA is an FDA-approved synthetic, biodegradable, biocompatible and nontoxic polymer. Numerous examples of the use of PLGA-based NPs for therapeutic or imaging agent delivery via passive and active tumor targeting have been reported in the literature, providing key insights into the safety, degradability, and carrier potential of such systems.[21–27] In the work described in this dissertation, PLGA is used to form the core of the NPs which acts as a depot for the entrapment and controlled release of the chemotherapeutic agent doxorubicin (DOX), as described in Chapter IV.

2.2 Drug Delivery

The use of nano-sized probes enhances tumor selectivity via passive and active targeting. Nano-sized agents can reach a given tissue, organ, or cell by the virtue of their intrinsic properties, such as particle size or hydrophobicity/hydrophilicity via passive targeting. In passive targeting, the nanocarriers take advantage of the enhanced permeability and retention (EPR) effect.[28,29] The EPR effect refers to the ability of nanocarriers to passively accumulate in tumor tissue because of extravasation (leakage from blood vessels into the tissue around it) across leaky tumor blood vessels and retention due to poor lymphatic drainage. Tumors generate angiogenesis-stimulating growth factors

that stimulate the formation of new leaky blood vessels to maintain their nutrient supply in a process known as angiogenesis. These leaky blood vessels have fenestrations in the size range of 100 nm to 2 μm.[30] In addition, the local compressive forces generated by tumor cell proliferation leads to contraction of blood vessels that contributes to increased interstitial fluid pressure and poor lymphatic drainage.[31] The combination of these tumor characteristics enables nanocarriers to passively leak into tumor tissue and then be retained there for long periods of time due to reduced lymphatic function.[31]

In addition, nanocarriers can be further modified to achieve molecular specificity to tumors through active targeting. Active targeting aims to increase the delivery of drug to a target using specific interactions that can allow for nanocarriers to bind specifically to the cell.[32] Active targeting moieties may include carbohydrates, peptides, antibodies, or antibody fragments; these moieties can be covalently attached directly to the surface of nanocarriers or by using linker molecules.[33]

Table 2-1 shows particle sizes that are useful for NP applications such as drug delivery, detection, and imaging. An ideal size of NP depends on the type of tumor, material, and properties of NP such as shape, charge, polydispersity values, complexity of targeted area, etc. The table also shows their method of clearance from the blood.

Nanoparticles enter the vascular system via intravenous administration and they are distributed to the organs and peripheral tissues of the body. They may undergo adsorption or opsonization by blood plasma proteins (opsonins). These proteins immediately bind to unprotected (for example, non-PEGylated) nanoparticles. Macrophages can easily recognize and remove them via phagocytosis before they reach to the site where they are designed for treatment.[34] Polymeric nanoparticles usually are isolated in the mononuclear

phagocytic system organs such as spleen, liver, and lymph nodes. Non-biodegradable polymeric nanoparticles commonly accumulate in the liver and spleen, and they can lead to toxicity and other negative side effects.[34,35]

Table 2-1. Particle size relative to clearance and application.

Particle Size	Nanomedicine Applications	Method of Clearance From the Circulation	References
<10 nm	Contrast agents for detection/imaging	Rapidly cleared from the blood via extravasation or renal clearance	[36]
10-20 nm	Contrast agents for detection/imaging	Renal and lymphatic clearance	[37]
20-100 nm	Drug/gene delivery, cancer therapy, sites of inflammation	Optimal range to escape physiological barriers; high circulation potential, reduced filtration by liver and spleen	[36–38]
100-200 nm	Drug/gene delivery	High potential for prolonged circulation	[37,39]
200-600 nm	Drug delivery	Generally cleared by the spleen	[38,40]

Large particles, bigger than >1 μm, are usually opsonized and accumulate in the liver and spleen. They may aggregate and block capillary of mononuclear phagocytic system organs. Because they are cleared from blood circulation immediately, large particles are usually administered nasally or orally for inhalation therapy, or implanted for long-term drug delivery.[36,37]

As a result, the optimal nanoparticle size referred by many studies is range of approximately 100–200 nm to take advantage of EPR effect and to efficiently escape from the physiological barriers.[41]

Although there are several advantages of using NPs for targeting diseases, encapsulation and release of therapeutics, and personalized medicine, there is a relatively small number of Food and Drug Administration (FDA)-approved NP-based treatments, drugs, and devices. Table 2-2 shows current FDA-approved nanomedicine therapeutics for treatment of breast cancer.[42]

Table 2-2. Nanomedicines approved by the FDA or which are in clinical trials for breast cancer treatment.[42]

Nanomedicine	Encapsulated Drug	Area of Treatment	FDA approval
Doxil®	Doxorubicin	Breast / ovarian cancer	November 1995
Abraxane®	Paclitaxel	Breast, pancreatic, and non-small cell cancer	January 2005
Myocet®	Doxorubicin	Breast cancer	Approved in Europe and Canada, 2000
Genexol®-PM	Paclitaxel	Breast and pancreatic cancer	Marketed in South Korea and Europe
Narekt-102®	Irinotecan	Breast and colorectal cancer	Phase III
LEP-ETU®	Paclitaxel	Breast, ovarian, and lung cancer	Phase II
Endo TAG-1®	Paclitaxel	Breast and pancreatic cancer	Phase II
Lipoplatin®	Cisplatin	Breast, pancreatic, and head and neck cancer	Phase III

2.3 NIR Optical Imaging

While the 5-year relative survival rate of advanced breast cancer patients is only 27%, the survival rate among patients diagnosed with localized breast cancers is much

higher at 98%.[43] Early detection of cancer before metastasis has a significant impact on cancer survival. There are several types of noninvasive bioimaging techniques for cancer such as optical imaging (absorption, reflection, bioluminescence or fluorescence imaging), nuclear imaging (positron emission tomography or single positron emission computed tomography), magnetic resonance imaging (MRI), and ultrasound imaging.[12,44] Optical imaging is a fast, low cost, sensitive imaging approach for the non-invasive detection of cancers using an optical imaging system that uses light to probe cellular and molecular characteristics of cancer in the living body. Optical signal can be detected at a tissue depth of several centimeters with some optical devices depending on a number of factors including signal strength and wavelength, detector sensitivity, and optical properties of tissue.[45] Optical imaging systems have been used in the operating room and clinic for the determination of location and resection of malignant tumors in addition to screening for cancer.[46–48]During surgery, normal and tumor tissue can be distinguished using properly designed optical contrast agents and healthy tissue removal may be avoided.

Although optical imaging has great advantages over the other imaging techniques, it has a major challenge: its poor specificity due to background signal. Optical contrast agents can increase the sensitivity and specificity of cancer detection. If these agents have fluorochromes with a good quantum yield, high molar extinction coefficient, and high specific binding to cancerous tissue, this challenge can be overcome. [45,49]

Near-infrared (NIR) region enables highly sensitive noninvasive *in vivo* imaging with an optical imaging system. The NIR region (700-1000 nm) provides a unique advantage for the imaging of tumors. Water and most biological chromophores do not absorb significant energy in this region.[50–52] As a result, NIR radiation enables best optical

penetration into skin and tissues μm to cm deep.[53] Tumors located close to the surface of skin such as breast tumor can be reached by endoscopic methods and can be detected easily with greater depth penetration using non-invasive or minimally invasive optical imaging approaches.

NIR fluorescence probes have progressed significantly and have been investigated in bioimaging and therapeutics in the last two decades.[49] Various novel NIR fluorescence dyes have been synthesized and developed for imaging and therapy.[49] These dyes can also be conjugated with moieties of interest and used for cancer imaging with high specificity and sensitivity.[54] Indocyanine green (ICG) is a FDA-approved NIR organic dye which is used for various clinical applications at present for optical imaging of biopsies, blood flow evaluation, hepatic function, and lymph node mapping in breast cancer patients.[55,56] Our research group has recently published an article focusing on the biodegradable NIR aza-BODIPY dye loaded nanoparticles for optical cancer imaging.[57]

Besides imaging properties of NIR fluorescence dyes, they can also be applied as effective agents for photothermal therapy. The phthalocyanine-aggregated pluronic NPs[58] and IR780-loaded NPs[59] are designed as novel agents for photothermal therapy for clinical use. These dyes stimulate NIR absorption of laser light delivered by a diode laser, inducing thermal damage to solid tumors.

2.4 Theranostics

The field of theranostics encompasses technologies that combine therapeutics and diagnostics on a single platform. Theranostic NPs can be used for diagnosis of diseases followed by therapy to patients who can likely respond to a given treatment, and therapy

followed by diagnosis to monitor early response to treatment and predict treatment efficacy. Theranostics have found wide applications not only in the cancer treatment, but also inflammatory/autoimmune diseases,[60–63] neurodegenerative,[64–66] diabetes,[67,68] lung,[69] and cardiovascular affections.[70,71]

Cancer theranostics is an evolving multidisciplinary field that includes novel biomarkers to advance molecular diagnostics of cancer, molecular imaging probes and techniques for early detection of cancer, molecular image-guided cancer therapy, and nanoplatforms incorporating both cancer imaging and therapeutic components.[13,72–74] Iron oxide nanoparticles,[75] quantum dots,[76] carbon nanotubes,[77] gold nanoparticles,[78] silica nanoparticles,[79] and polymer nanoparticles[80] have been developed as theranostic carriers for imaging and treatment agents.

Yu *et al.* prepared and characterized doxorubicin-loaded thermally cross-linked superparamagnetic iron oxide nanoparticles (TCL-SPION) for cancer imaging and therapy.[75] SPIONs were used as magnetic resonance (MR) contrast agent. Tumors were detected by MR imaging and at the same time doxorubicin chemotherapeutic drug were delivered in sufficient amounts to tumors. In contrast to the potential toxicity risk of metallic or inorganic nanoparticles associated with their long-term residence in body, SPIONs are biodegradable and only show toxicity at very high exposure levels and concentrations of iron *in vivo* studies.[75,81]

Quantum dots (QDs), are fluorescent semi-conductive nanocrystals that have promising features such as low photobleaching, narrow photoluminescence spectra, and high quantum yield for use in cellular imaging with high-resolution, targeting, and diagnostic potential.[82] Due to the long-term stability and brightness of QDs, they are ideal

candidates for live animal targeting and imaging. However, the non-protected core or core/shell QDs shows toxicity due to release of toxic ions such as Cd^{2+}, Se^{2-} from the QDs' core.[83] Bagalkot *et al.* synthesized a QD−aptamer−doxorubicin conjugate as a targeted prostate cancer imaging, therapy, and sensing system. They demonstrated *in vitro* the specificity and sensitivity of prostate cancer imaging, therapy and sensing with this nanoparticle conjugate system.[76]

Single-walled carbon nanotubes (SWCNTs) are being investigated as promising multifunctional imaging and therapeutic agents because they exhibit photoluminescence in the NIR and low toxicity. [84] Liang *et al.* synthesized PEGylated SWCNTs as a theranostic agent for imaging and photothermal therapy (PTT) of metastatic sentinel lymph nodes in an animal tumor model. The intrinsic NIR photoluminescence of SWNTs was used for imaging.[77]

Gold-based nanoparticles can absorb and transfer optical energy into heat with high efficiency, and have been used in the field of PTT of cancer. Huang *et al.* prepared biodegradable gold nanovesicles composed of biocompatible polymers, poly(ethylene glycol)-*b*-poly(ε-caprolactone) with an ultra-strong plasmonic coupling effect for photoacoustic imaging and PTT.[78]

Ceramic nanoparticles are prepared by a simple well-known sol-gel process which requires ambient temperature conditions comparing with preparation of other types of nanoparticles. Their shape, size and porosity can be easily adjusted. They are extremely stable to changes of pH and temperature. Ceramic nanoparticles such as silica, titania, etc., are also known for their compatibility with biological systems.[85] Roy *et al.* synthesized photosensitizer-doped organically modified silica-based nanoparticles. These particles

were irritated and taken up particles by tumor cells resulted in significant cell death through PTT. The entrapped drug 2-(1-hexyloxyethyl)-2-devinyl pyropheophorbide-a (HPPH, or Photochlor®) was also used for fluorescence bioimaging.[79]

Due to biocompatibility and diversity of polymeric nanoparticles, they have become one of the most studied platforms for targeted drug delivery, diagnosis, and imaging. Polymer-based nanoplatforms are appropriate for the development of theranostic nanoparticles. Xiong *et al.* prepared a chemotherapeutic drug cisplatin loaded conjugate based on poly(L-glutamic acid) modified with Cy7 NIR dye for imaging and treatment of cancer.[86] A detailed review on polymer-based nanoparticles will be given in Chapter IV. Similarly, polymeric nanoplatforms have been used in personalized theranostics. Use of personalized theranostics involves optimized treatment protocols tailored to each specific patient. In theory, personalized theranostics would result in the delivery of the right drug to the right cancer patient at the right time, and result in significant improvements of patient's health and a reduction in healthcare costs.

III. ENZYMATICALLY ACTIVATED NPS (EANPS) FOR OPTICAL IMAGING OF BREAST CANCER

This chapter includes text and figures from the previously published article "Özel, T.; White, S.; Nguyen, E.; Moy, A.; Brenes, N.; Choi, B.; Betancourt, T. Enzymatically Activated near Infrared Nanoprobes Based on Amphiphilic Block Copolymers for Optical Detection of Cancer. Lasers Surg. Med. 2015, 47 (7), 579–594" for which permission from the journal has been obtained (see Appendix A).

Unless otherwise noted, all excerpts and figures herein included were obtained or generated by the author of this dissertation. All modifications from the published article are clearly noted in the chapter using italicized font.

3.1 Introduction

Cancer remains one of the most prevalent diseases to date. The average 5-year survival rate for cancer patients is 68%,[87] suggesting that despite great advances in diagnostics and therapeutics, there is still a great need for improved options. Patient survival rates are highly influenced by the stage at which the cancer is diagnosed.[87] Consequently, development of improved methods for detection of cancer at an early stage is of great importance.

NIR optical imaging has emerged recently as a viable alternative for the detection, monitoring, and image-guided resection of tumors.[46,88,89] Imaging in the NIR region (700–1,000 nm) is advantageous since absorption of most biological chromophores, including oxyhemoglobin, deoxyhemoglobin, melanin, and fat in this region is minimal.[50,51] Imaging-based detection of tumors at early stages via fluorescence methods is limited by the low fluorescence contrast between normal and cancerous tissue. Use of probes targeted to or activated by the disease is a promising approach for creating sufficient contrast.[51]

Significant work has been done in the development of fluorescent probes that can provide disease specificity and increased signal-to-noise ratio through an activation mechanism. Among these, macromolecular protease-triggered NIR fluorescent probes have been used as effective triggered fluorescent contrast agents for cancer. Weissleder and co-workers developed NIR conjugate probes for in vivo imaging of tumors with high protease activity by the conjugation of the fluorescent dye Cy5.5 to poly-L-lysine chains.[90,91] This work demonstrated the ability of tumor lysosomal proteases to cleave the conjugate to develop NIR signal in vivo. The effectiveness of these systems has been demonstrated in preclinical models of metastatic ovarian cancer,[92] esophageal cancer,[93] gastric cancer,[94] and sarcoma.[95,96] These systems have also been utilized for detection and imaging of other diseases associated with changes in enzymatic activity of the tissue, including inflammation and vascular disease.[97–105]

Few investigations have been performed in the formulation of activatable NIR fluorescent probes in nanoparticle format.[106–111] The use of nanoparticles can improve tumor targeting via passive and active targeting, taking advantage of the enhanced permeability and retention (EPR) effect, and by permitting concurrent incorporation of targeting moieties with high affinity to tumor cell biomarkers. The EPR effect is due to a combination of leaky angiogenic blood vessels with 100 nm–2 mm pores that allow the extravasation of nano-sized particles,[112] and deficient tumor lymphatics that allow particle accumulation at cancerous tissue.[29,112–114] In addition, because of their macromolecular design, nanoparticles allow incorporation of a range of functionalities into a discrete entity. The benefits of nanoparticles in bioimaging and therapeutic applications have been

previously explored with gold nanoparticles, nanoshells, nanorods, and nanohorns as photothermal agents.[115–120]

In the present work, we developed methods for facile preparation of a contrast agent for fluorescence-based imaging of tumors that could: (i) take advantage of the benefits of nanomedicine, including the ability to carry a high payload of the imaging agent to target tumors, and (ii) provide a mechanism for tumor-mediated activation of fluorescence. Specifically, enzymatically activated nanoprobes (EANPs) that easily assemble from well-characterized biocompatible polymers were developed and evaluated *in vitro* as contrast agents for highly specific fluorescence imaging in cancer. These nanoprobes utilize protease-labile polypeptides labeled with NIR fluorophores as a mean to provide an off-on switch for fluorescence development that is triggered by tumor-overexpressed enzymes.

3.2. Materials and Methods

EANPs, consisting of a core-shell structure (Figure 1-1), were prepared by nanoprecipitation of amphiphilic block copolymers. The hydrophobic core, which could be used for delivery of chemotherapeutic or additional imaging agents, is made of the biodegradable and biocompatible polymers poly(lactic-co-glycolic acid) (PLGA) and poly-(lactic acid) (PLA). The surface of EANPs contains the hydrophilic polymers poly(ethylene glycol) (PEG) and poly-L-lysine (PLL). PEG increases residence time of probes in the circulation[121] by acting as a shield against adsorption of opsonin biomolecules and the consequent rapid recognition and removal by the reticuloendothelial system (Kuppfer cells and macrophages).[122] Because of the high flexibility and water-binding ability of PEG, it can sterically stabilize nanoparticle suspensions and hinder their

interaction with plasma proteins and the immune system.[123–126] Finally, PLL acts as a protease cleavable anchor for NIR fluorophores, as previously utilized in peptide-based NIR probes.[90–92] PLL is a model polypeptide that can be cleaved by proteolytic enzymes commonly overexpressed by tumors, such as cathepsin B and D. Close-packed binding of NIR fluorophores to the PLL backbone results in fluorescence quenching due to processes such as non-radiative energy transfer. Enzymatic cleavage of PLL results in increased mobility and space between fluorophores, resulting in fluorescence activation. (Figure 3-1)

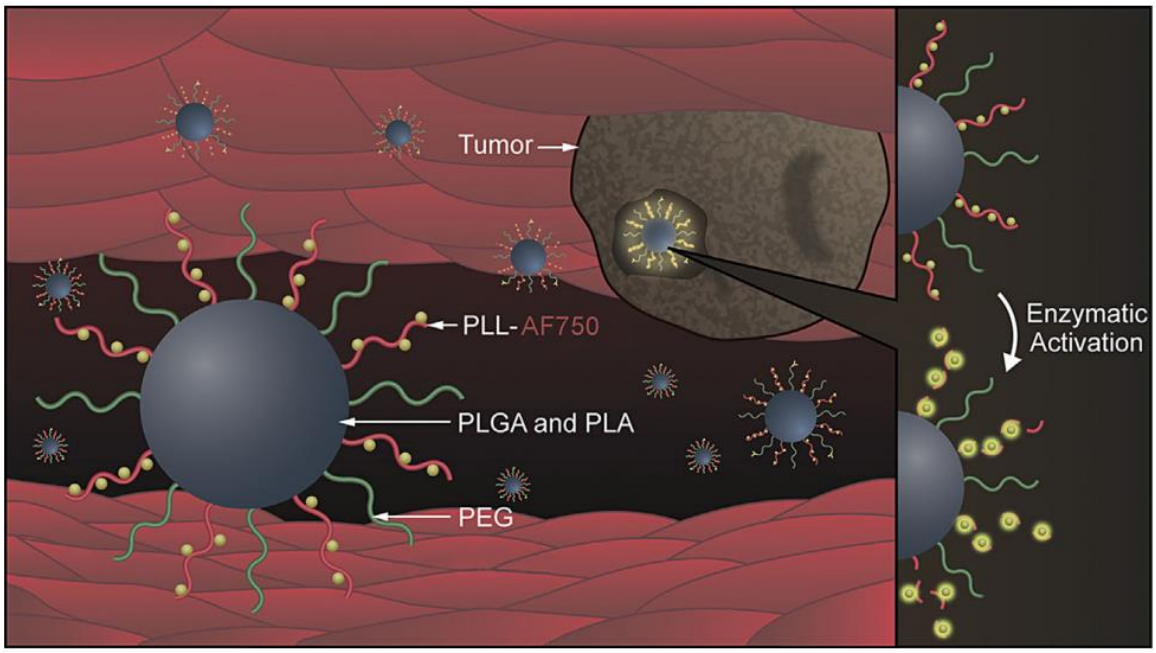

Figure 3-1. Design and function of enzymatically activated nanoprobes (EANPs). EANPs are prepared by nanoprecipitation of blends of amphiphilic PLA-PEG and PLGA-PLL copolymers. Near infrared fluorescent molecules covalently attached to PLL chains are initially quenched. Protease-mediated cleavage of PLL chains induces fluorescence activation by allowing their dispersion in the physiological medium.

3.2.1 Materials

PLGA with terminal carboxylic acid groups (5050 DLG 2A, MW 16,000 Da) was acquired from Lakeshore Biomaterials (Birmingham, AL). Bifunctional poly(ethylene

glycol) with hydroxyl and carboxylic acid terminal groups (OH-PEG-COOH, Mn 3,400 Da) was obtained from Laysan Bio (Arab, AL). Poly(ethylene glycol) methyl ether (OH-PEG-OMe, Mn 5,000 Da), 3,6-dimethyl-1,3-dioxane-2,5-dione (lactide), Trypsin solution from porcine pancreas, *N,N′*-dicyclohexylcarbodiimide (DCC), N-hydroxysuccinimide (NHS), poly-L-lysine hydrobromide (PLL, MW 1,000–5,000 Da), *Nα*-tosyl-L-lysine chloromethyl ketone (TLCK), and *N*-(dimethylaminopropyl)-*N′*-ethylcarbodiimide HCl (EDC) were purchased from Sigma–Aldrich (St. Louis, MO). Alexa Fluor 750 carboxylic acid succinimidyl ester (AF750) was obtained from Molecular Probes (Invitrogen, Carslbad, CA). All organic solvents used were of at least reagent grade. Deionized water (DI H_2O) was produced with a Millipore Direct Q system.

3.2.2 Synthesis of PLGA-PLL

PLGA-PLL copolymers were prepared by activation of carboxylated PLGA into primary amine-reactive *N*-hydroxysuccinimide esters via carbodiimide chemistry (Fig. 3-2). Activated PLGA formed amide bonds upon conjugation with PLL primary amine groups. PLGA (1 g) was dissolved in 10 mL of chloroform. To this solution, 129 mg of DCC and 72 mg of NHS (PLGA: DCC: NHS molar ratio of 1:10:10) were added and allowed to react overnight at room temperature. Urea byproduct was filtered using a 0.2 μm syringe filter. The activated PLGA was recovered from the solution by precipitation in diethyl ether, centrifuged and rapidly dried under vacuum. Activated PLGA (0.8 g) was then immediately dissolved in dimethylsulfoxide or dimethylformamide and reacted with 125 mg of PLL (PLGA/PLL molar ratio of 2:1 using an average PLL molecular weight of 4,000 Da) in the presence of triethylamine (TEA) (PLL: TEA molar ratio of 1:40).

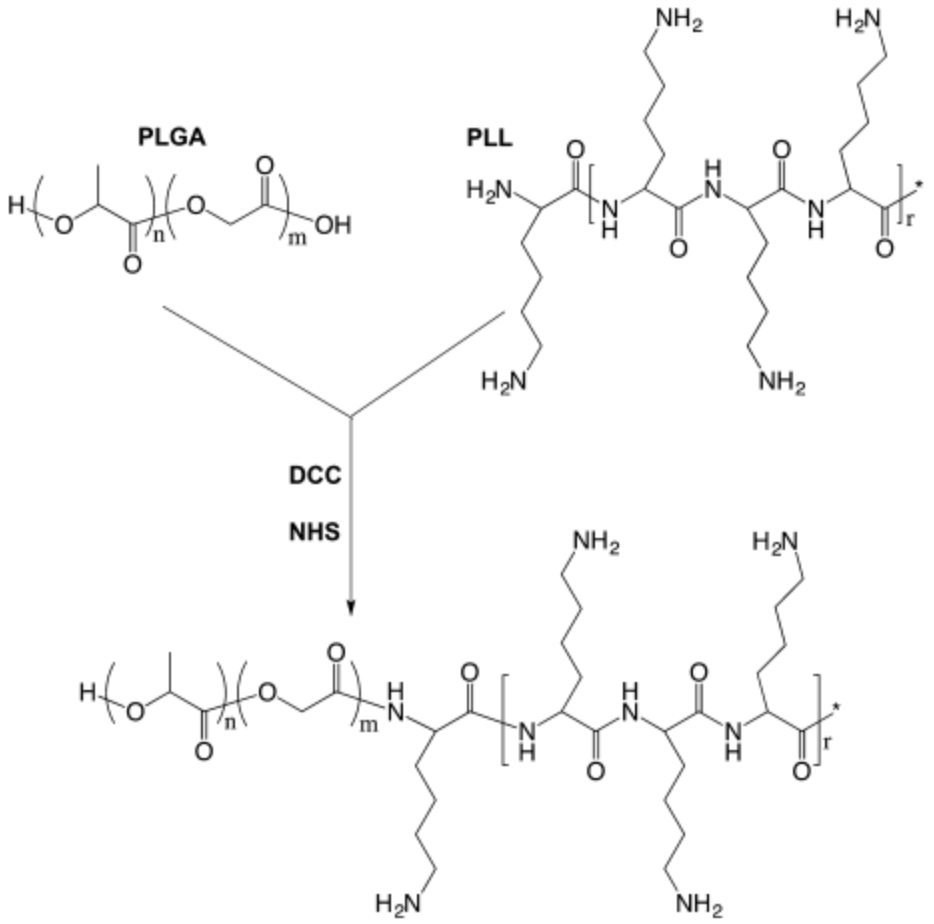

Figure 3-2. Synthesis of PLGA-PLL copolymer. This copolymer was synthesized by carbodiimide-mediated coupling of acid-terminated PLGA and PLL.

After 24 hours, the copolymer was precipitated into DI H_2O and centrifuged. The polymer pellet was dissolved in acetone, precipitated into DI H_2O, and centrifuged two more times to remove unbound, water-soluble PLL and remaining byproducts. The polymer was then dried under vacuum and stored desiccated at -20 ˚C. ^{1}H nuclear magnetic resonance spectroscopy (^{1}H-NMR) was used for characterization of the copolymer. For NMR characterization, a Bruker AMX-500 NMR (Numega Resonance Laboratories, San Diego, CA) and a Bruker Avance 400MHz FT NMR were used.

3.2.3 Synthesis of PLA-PEG-COOH and PLA-PEG-OMe

Two types of PEG were used in the preparation of EANPs: Methoxy (─O─CH_3)-terminated PEG (PEG-OMe) acts as a stabilizing polymer. PEG terminated in carboxylic acid groups (PEG-COOH) was used to provide a site for covalently binding targeting antibodies to EANPs in future work. PLA-PEG-COOH and PLA-PEG-OMe were prepared by the ring opening polymerization of lactide initiated by terminal hydroxyl groups of heterofunctional PEGs (Fig. 3-3).[127] Prior to polymerization, lactide was recrystallized from hot ethyl acetate. Recrystallized lactide and PEG (either PLA-PEG-COOH or PLA-PEG-OMe) were placed in an oven-dried, two-necked reaction flask. Toluene was added and the flask was heated to 110 ˚C with a silicon oil bath. Nitrogen or argon was bubbled into the solution throughout the process. The polymerization was allowed to occur for 2–4 hours, during which an increase in the content's viscosity was observed. The reaction was then stopped by rapid cooling and the polymer was recovered by precipitation in diethyl ether. For further purification, the polymer was re-dissolved in acetone and precipitated in diethyl ether two additional times. The polymer was then dried under vacuum and stored desiccated at -20 ˚C. NMR was used for characterization of the copolymer.

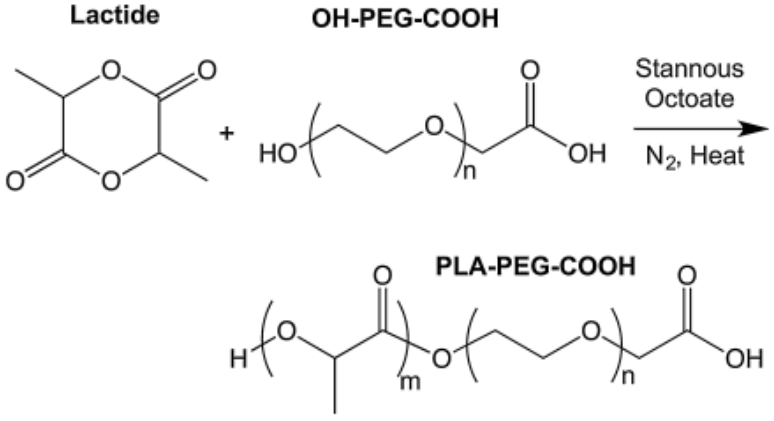

Figure 3-3. Synthesis of PLA-PEG copolymers. PLA-PEGs were prepared by the ring opening polymerization of lactide on terminal PEG hydroxyl groups. Here the reaction is shown for the formation of PLA-PEG-COOH. Polymerization of PLA-PEG-OMe occurs similarly.

3.2.4 Preparation of EANPs

EANPs were prepared via nanoprecipitation[127,128] of copolymer blends. PLGA-PLL, PLA-PEG-COOH, and PLA-PEG-OMe were dissolved in acetone separately at 50 mg/mL. These solutions were combined in the following volume ratios: 500 mL PLGA PLL, 125 mL PLA-PEG-COOH, and 125 mL PLA-PEG-OMe. An additional 2 mL of acetone were added. The copolymer solution was then added dropwise to 5 mL of a stirring aqueous solution of 10 mg/mL bovine serum albumin. EANPs formed spontaneously because of the migration of the water miscible solvents into the aqueous phase, and the consequent precipitation of the hydrophobic regions of the copolymers (PLGA and PLA). The solvent was evaporated under mild vacuum. EANPs were washed three times with DI H_2O by centrifugation at 34,500x*g* for 20 minutes using sonication to resuspend the pellets. EANP suspensions (4.4 mg/mL) were stored at 4 ˚C. The size of EANPs was determined using dynamic light scattering (DLS) using a Malvern Zetasizer upon dilution in phosphate buffered saline (PBS, pH 7.4). Transmission electron microscopy (TEM) was used to confirm the size and morphology of EANPs.

3.2.5 Conjugation of Fluorescent Dye to EANPs

AF750 was conjugated to surface PLL chains on EANPs. For this process, 4 mL of EANPs were reacted with 0.4 mg of AF750 for 12 hours in the dark at room temperature. The NHS ester of AF750 reacts with primary amines on PLL forming stable amide bonds.

The close proximity and high concentration of PLL-bound AF750 on the surface of EANPs resulted in fluorescence quenching. EANPs were purified by centrifugation and washed with DI H_2O three times to remove unbound AF750. The highly-colored AF750-labeled EANPs were characterized by absorption and fluorescence spectroscopy, and their size by DLS.

3.2.6 Enzymatic Activation of EANP Fluorescence

Enzymatic activation of EANP fluorescence study was performed with a Biotek H4 multimode plate reader (λ_{Ex} =740 nm, λ_{Em} =775 nm) to demonstrate the reproducibility of fluorescence enhancement. Studies were conducted in 96-well plates. Four repetitions were done for each sample. Controls consisted of EANPs that were incubated with PBS buffer only, or EANPs exposed to trypsin together with the protease inhibitor TLCK. Fluorescence readings were normalized with respect to the control consisting of EANPs exposed to PBS only. Data are presented as the average of four replicates that were analyzed per sample. Student's t-tests were performed to establish statistically significant differences between samples based on a confidence level of 95% ($P<0.05$).

3.2.7 Cell Culture

MDA-MB-231 human mammary adenocarcinoma cells were obtained from the American Type Tissue Collection (ATCC). MDA-MB-231 cells are known to produce high levels of cathepsins.[129] Cells were cultured in Dulbecco's Modified Eagle's Medium (DMEM) with 10% bovine serum in an incubator at 37 ˚C and under a CO_2 atmosphere.

3.2.8 Determination of EANP Cytocompatibility

MDA-MB-231 cells were plated at 5,000 cells/well in 96-well plates with 100 μL of complete cell culture media. Peripheral wells were filled with sterile, buffered saline solution to maintain appropriate humidity. After 24 hours of incubation, the growth medium was replaced with suspensions of AF750-labeled EANPs in complete medium in the concentration range of 1 to 1,000 μg/mL. The cells were then incubated at 37 ˚C and 5% CO_2 for 72 hours. Wells with cells not exposed to EANPs functioned as the positive cytocompatibility controls, while wells with cells treated with 100 μL of methanol for 15 minutes served as the negative cytocompatibility controls.

The viability of the cells was determined using the MTT assay. The media was replaced with 100 μL of 0.5 mg/mL MTT reagent (thiazolyl blue tetrazolium bromide, Sigma–Aldrich) in growth medium. The cells were incubated for an additional 3.5 hours. The media was then carefully removed and the resulting formazan crystals were dissolved in 100 mL of dimethyl sulfoxide. The peak absorbance of formazan was read at 590 nm with a Biotek H4 multi-mode plate reader. The average absorbance values were corrected by subtracting the average baseline absorbance at 700 nm. Averages and standard deviations were calculated from the measurements of six wells for each condition. Viability was calculated as a percentage of the positive cytocompatibility control. Student's t-tests were performed to establish statistically significant differences between samples based on a confidence level of 95% ($P<0.05$).

3.2.9 Microscopic Study of EANP Interaction with Cells

Studies were conducted with only MDA-MB-231 cells to assess the degree to which observed fluorescence was associated with enzymatic development, and that near infrared fluorescence could in fact be observed. For these studies, MDA-MB-231 cells were plated on 8-well Lab-Tek chambered coverslips at a density of 50,000 cells per well in 0.3 mL of media. The cells were grown under normal culture conditions 24 hours prior to microscopy studies. To begin the study, the media was replaced with AF750-labeled EANPs at a concentration of 500 μg/mL in the presence of varying concentrations (7.8–250 μM) of the protease inhibitor TLCK. Cells exposed to EANPs in the absence of the inhibitor were used as positive controls, while cells incubated with media only (no EANPs and no TLCK) were used as negative controls. The cells were incubated under normal growth conditions for 48 hours, after which they were washed three times with Dulbeccos' phosphate buffered saline and immediately imaged with a AMG EVOS1 FL LED-based microscope utilizing a Cy-7 filter cube (Ex: 710/40, Em: 775/46, optimal for AF750 per manufacturer).

3.3. Results

3.3.1 Synthesis of PLGA-PLL

Qualitatively, conjugation was noted by the quasi-micellar behavior of the copolymer upon precipitation in water. The composition of PLGA-PLL copolymer was analyzed by FTIR and ^{1}H-NMR (*as described in the published article)*[14]. NMR and FTIR were confirmed the presence of PLGA and PLL in the copolymer and discussed in the paper.[14]

3.3.2 Synthesis of PLA-PEG-COOH and PLA-PEG-OMe

FTIR was used to confirm the structure of the PLA-PEG-COOH and PLA-PEG-OMe copolymers, *as show in the published article*.[14] Proton NMR (Fig. 3-4) also confirmed the polymer composition and was used to estimate the molecular weight of the polymer by comparing the area under the peak of the PEG protons at 3.6 ppm that of the polymerized poly(lactide) peaks at 1.6 and 5.2 ppm as previously reported.[128] A molecular weight of 21,200 Da was calculated in this manner.

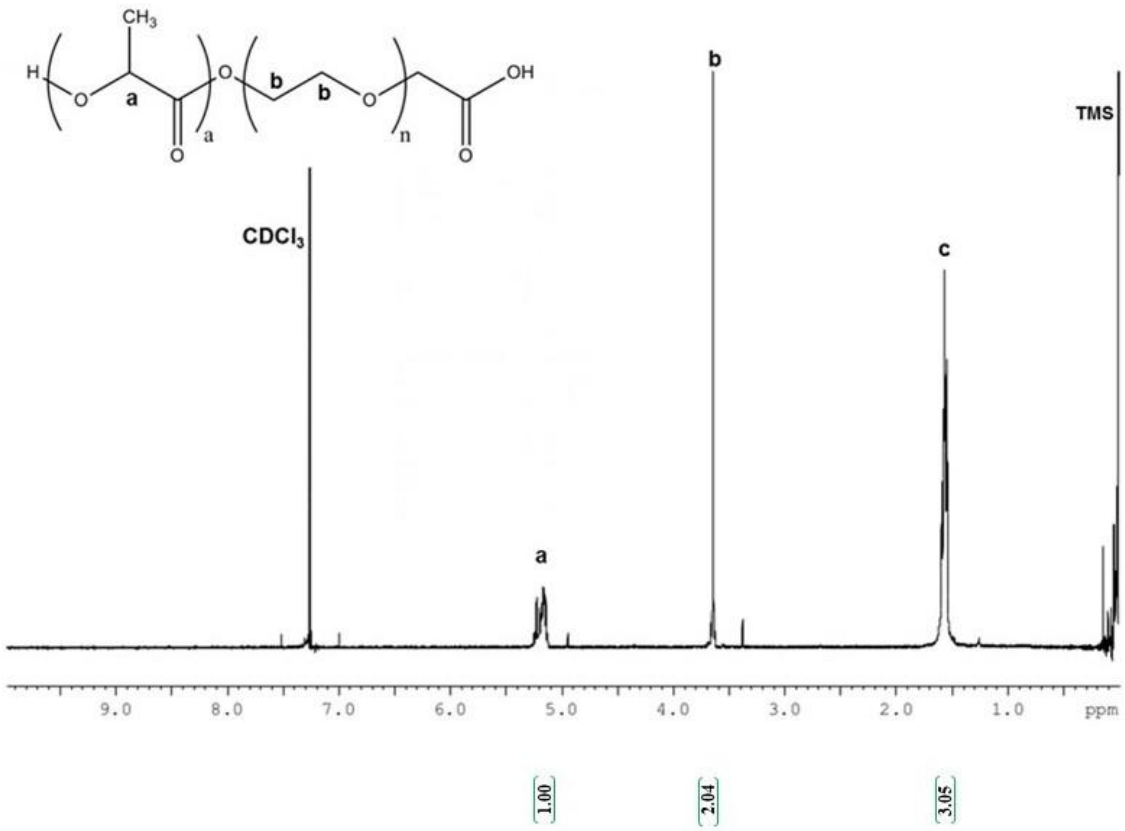

Figure 3-4. [1]H-NMR of PLA-PEG-COOH. NMR spectra of the copolymer presents the peaks associated with the original polymer blocks.

3.3.3 Preparation of EANPs

EANPs were successfully prepared via nanoprecipitation. Figure 3-5 summarizes

the characteristics of these nanoprobes. Figure 3-5A shows SEM images of the EANPs after attachment of AF750. *SEM images were obtained by Dr. Tania Betancourt.* Spherical EANPs of about 50–120 nm in diameter are observed. Figure 3-5B shows the dynamic light scattering (DLS) size distribution of representative batches of EANPs before and after AF750 conjugation. The hydrodynamic diameter of the particles after purification via centrifugation was in the range of 70–200 nm, with an average of about 100 nm. Sizing studies were performed by dynamic light scattering for more than nine batches before fluorophore conjugation or after conjugation of AF750. The fact that consistent sizing was obtained between batches demonstrates the reproducibility of the procedure. An overall size increase was also noticed upon fluorophore conjugation via DLS, possibly as a result of increased surface hydrophobicity leading to increased aggregation potential. Polydispersity indexes ranged from 0.05–0.11 before centrifugation to 0.11–0.17 after AF750 conjugation and purification. Figure 3-5C shows transmission electron microscopy images of the EANPs stained with uranyl acetate, which corroborate the size and shape of the EANPs.

The conjugation of AF750 to the PLL chains on the surface of the EANPs was confirmed visually. Figure 3-5D shows images of AF750-conjugated EANPs as a pellet at the last step of purification via centrifugation and as a suspension in PBS. Note the intense color of the pellet and the lack of AF750 in the supernatant on the left image, demonstrating effective covalent conjugation to the surface of the EANPs.

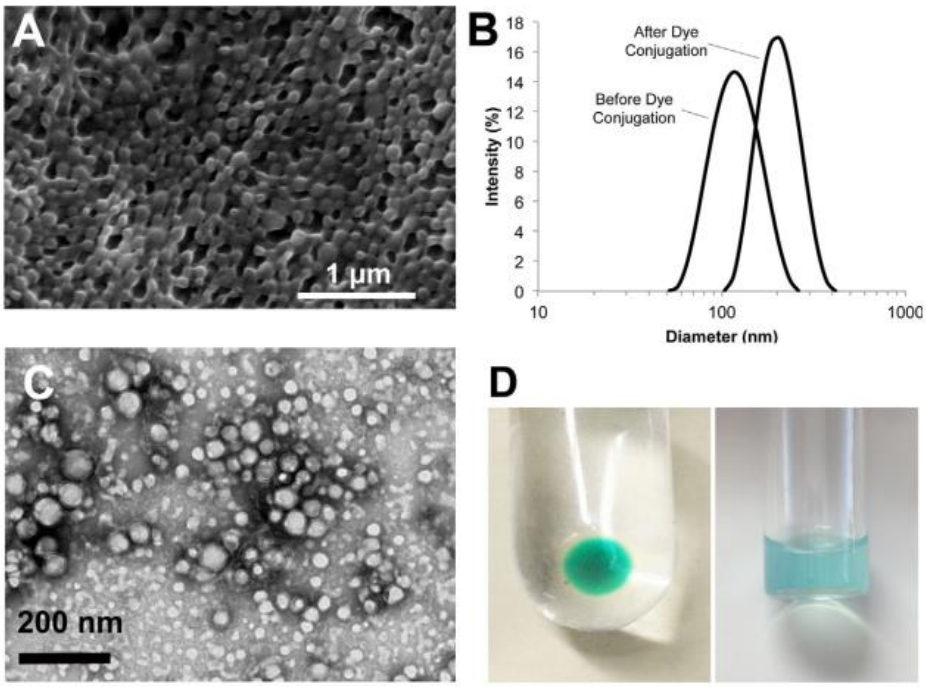

Figure 3-5. EANP Characterization. **(A)** Scanning electron microscopy images of EANPs after AF750 attachment. **(B)** Intensity-weighted size distribution of EANPs before and after AF750 conjugation. **(C)** Transmission electron microscopy image of EANPs. **(D)** Image of centrifuged AF750-labeled EANPs on last wash step and of EANP suspension.

3.3.4 Enzymatic Activation of EANP Fluorescence

Trypsin from porcine pancreas was used as a model protease for activation of the fluorescence of the AF750-labeled EANPs *in vitro*. Figure 3-6 shows a plot of the normalized fluorescence dynamics at 775 nm of EANPs exposed to trypsin, trypsin and TLCK, or buffer obtained in a 96-well microplate format. *As shown, over a 15-fold increase in fluorescence was observed within 120 minutes in the presence of 2.5 mg/mL trypsin. On the other hand, no fluorescence increase was observed in the absence of the protease and very little increase in the presence of trypsin and the trypsin inhibitor TLCK.* Thus, the data demonstrate that a marked increase in fluorescence signal can be achieved upon enzymatic activation of the nanoprobes.

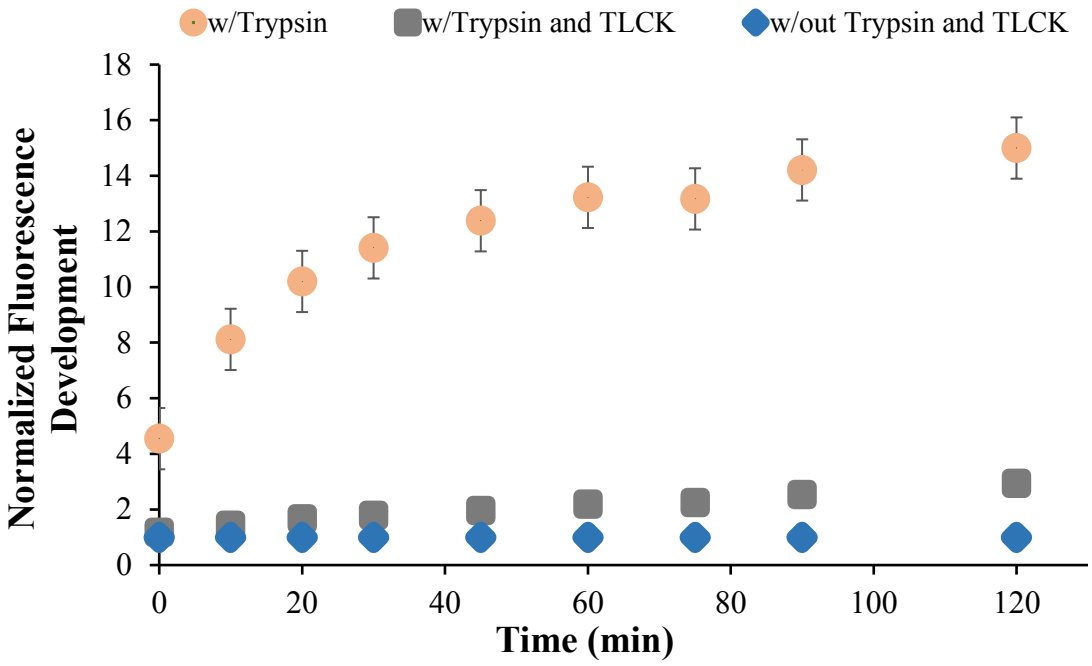

Figure 3-6. *In vitro* enzymatic activation of EANP fluorescence. Plot of average fluorescence at 775 nm versus time for EANPs exposed to trypsin, trypsin and TLCK, or buffer. Error bars represent standard deviation (n = 4). The error bars are too small to be seen on the graph for "w/Trypsin and TLCK" and "w/out Trypsin and TLCK" data.

3.3.5 Determination of EANP Cytocompatibility

The cytocompatibility of the EANPs was assessed with MDA-MB-231 cancer cells. Figure 3-7 shows the viability of cells exposed to AF750-labeled EANPs for 72 hours. Cells exposed to EANPs showed high viability (87–100 % of control), even at high concentrations. Neither a general dose-dependent viability trend nor a statistically significant difference was observed in these studies ($p > 0.15$ for all samples). As expected, the negative viability control alone had statistically lower viability ($p << 0.05$). In addition to quantitative viability determination via the MTT assay, cells were monitored via microscopy during the studies and no visual differences in cell morphology or growth were observed between EANP-treated NPs compared to cells in the positive viability control set. These studies overall suggest that the EANPs are biocompatible.

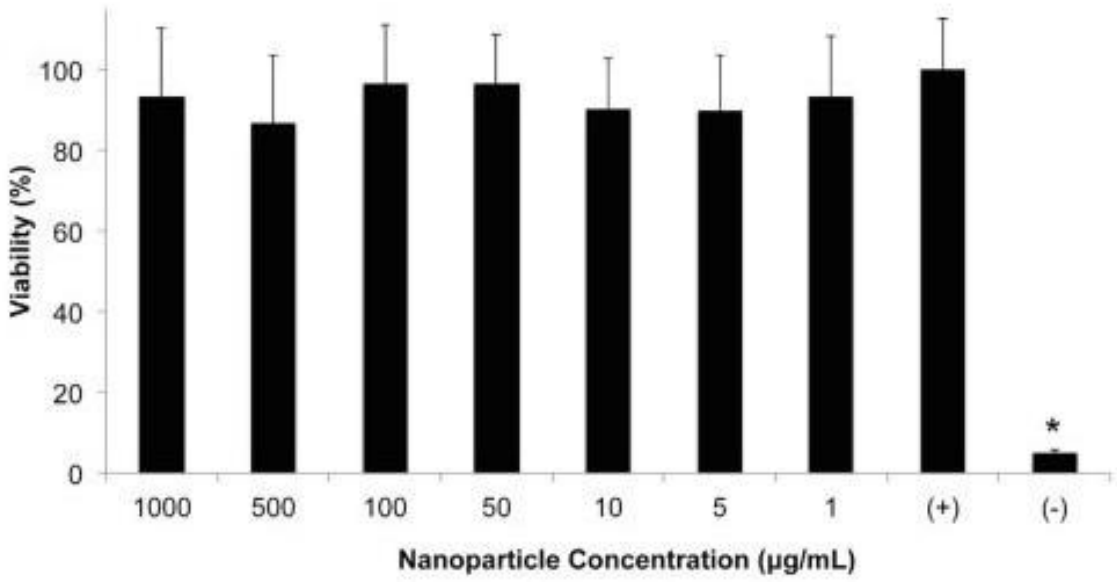

Figure 3-7. Interaction of EANPs with cultured cells. Viability of MDA-MB-231 cells after exposure to EANP 72 hours determined with MTT assay. Cells cultured in complete media without EANPs represent the positive control (+). Cells killed with methanol prior to MTT assay represent negative control (-). Bars represent standard deviation. Statistically significant difference compared to positive control ($p < 0.05$) is identified with an asterisk (*). Representative fluorescence, reflectance and overlay images of cells exposed to EANP suspensions for 36 hours.

3.3.6 Microscopic Study of EANP Interaction with Cells

Interaction of EANPs with MDA-MB-231 breast cancer cells was monitored to study the effect of enzymatic activity on fluorescence development. Figure 3-8 shows the transmission and NIR fluorescence images of the cells exposed to a constant concentration of EANPs but varying concentrations of the protease inhibitor TLCK. Increased TLCK concentrations prevented the activation of EANPs, leading to undetectable fluorescence in the cells compared to background. TLCK dose-dependency was observed in all samples with TLCK concentrations between 7.8 to 250 µM. These studies thus demonstrate the potential ability of the EANPs to interact with and be internalized into cells resulting in enzymatically-aided contrast enhancement.

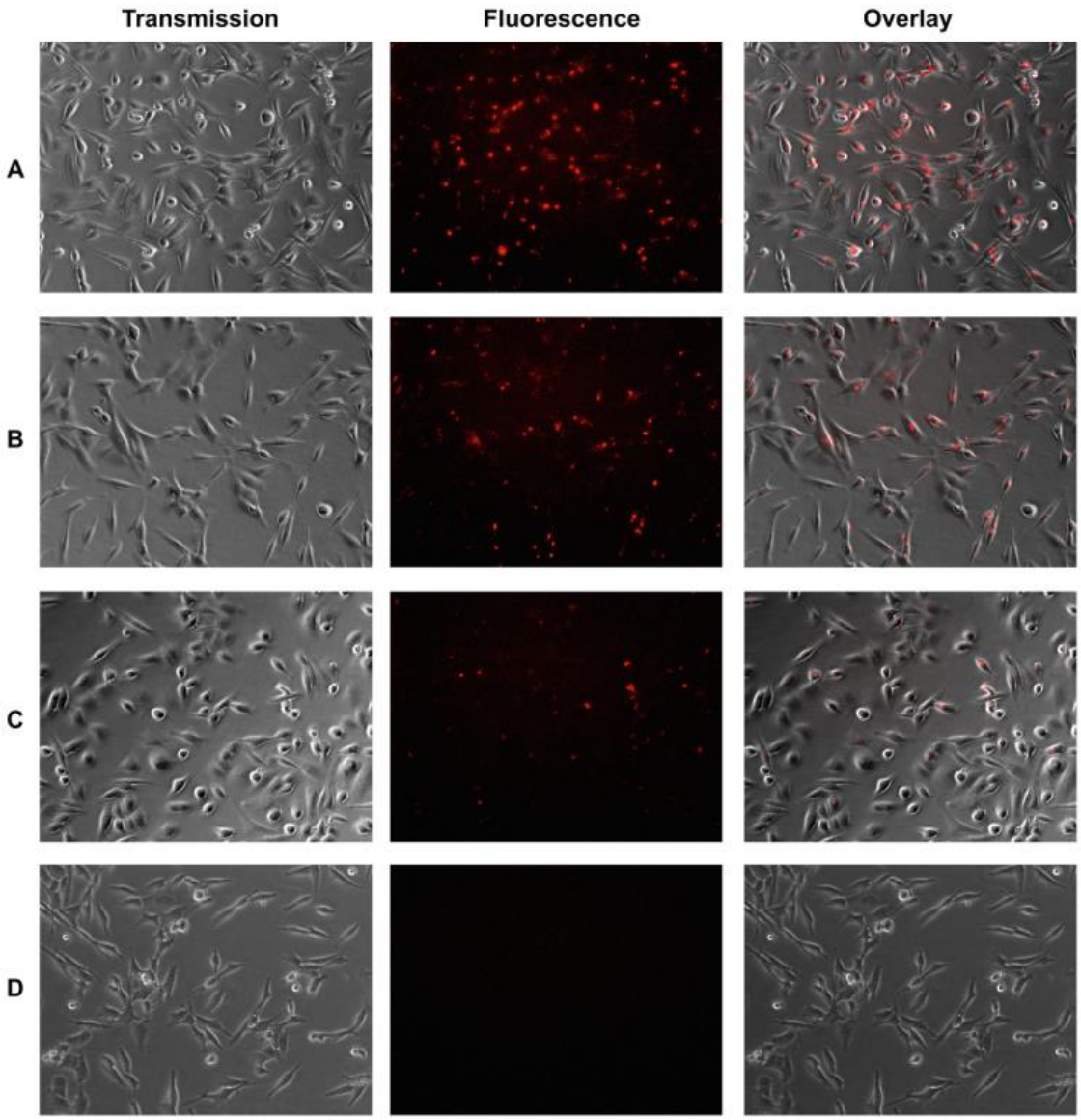

Figure 3-8. Enzymatic activation of fluorescence in cells. Transmission, NIR fluorescence, and overlay images of MDA-MB-231 cells exposed to AF750-labeled EANPs in the presence of varying concentrations of TLCK protease inhibitor: (A) 0.5 mg/mL EANPs and 0 μM TLCK, (B) 0.5 mg/mL EANPs and 31.25 μM TLCK, (C) 0.5 mg/mL EANPs and 250 μM TLCK, (D) 0 mg/mL EANPs and 0 μM TLCK.

In addition to this study, our collaborators at The University of California, Irvine conducted a similar nanoprobe-cell interaction study. They used FITC-labeled EANPs to monitor nanoprobe-cell interaction using MDA-MB-231 breast cancer cells and noncancerous fibroblast (HDF) cells. Cells were exposed to FITC-labeled EANPs for 36

hours. While noncancerous cells showed very low level of fluorescence, an increase in fluorescence was observed on the surface and within the cytoplasm of MDA-MB-231 cancer cells.[14]

The results of these nanoprobe-cell interaction studies suggest that cancer cells showed a high-level fluorescence development due to their overexpression of proteases.[14] *However, the use of different type of cell lines could also result in different fluorescence intensities.* Different cell lines might have differing rates of endocytosis, which could influence the extent of intracellular uptake of the nanoprobes, leading to differences in fluorescence intensities that are not completely caused by the enzymatic activation of the nanoprobes. The dependence of endocytic rates on fluorescent agent or nanoparticle identity, time of exposure, and cell line has been previously reported for benign and malignant cell lines of different metastatic potential.[130–132]

Our collaborators also conducted a study using tissue phantoms to investigate the effect of EANPs concentration and depth on imaging ability. Although EANPs were excited with a blue shifted laser and fluorescence emission was collected at wavelengths above 800 nm which are longer than the peak wavelength of AF750, between 2.5 to over 13-fold increased fluorescence levels at up to a depth of 4 mm into the tissue phantom were detected with enzymatically activated EANPs.[14]

3.4 Discussion

In this work, polymeric nanoprobes were developed as highly specific fluorescence-based contrast agents for cancer. Compared to other imaging technologies such as magnetic resonance imaging (MRI), computed tomography (CT), single photon

emission computed tomography (SPECT), and positron emission tomography (PET), fluorescence-based imaging can offer high resolution, the ability to resolve spectral features of tissue or contrast agents, relative simplicity, and low cost, and avoids the use of ionizing radiation. Fluorescent probes that provide disease specificity and increased signal-to-noise ratio through disease-mediated activation have been previously reported. Among these are multi-step bioorthogonal probes such as those that rely on the rapid and specific cycloaddition reaction between strained trans-cyclooctene or cyclooctyne-modified homing ligands and tetrazine or azide-functionalized fluorescent molecules.[133–136] These orthogonal probes, while effective at providing high signal-to-noise ratio, would require sequential delivery of the two components to the location of interest and are thus best suited for *in vitro* cell imaging.

Enzymatically-activated NIR fluorescent probes based on macromolecules that can interact with proteases overexpressed by tumors have also been developed,[90–96] as discussed in the introduction. In addition to cancer applications, the use of protease-activated probes has been demonstrated in pancreatitis,[97] a disease in which endoprotease activation is considered as one of the onset events; pulmonary inflammation;[98] atherosclerosis in which secreted proteolytic enzymes play a role in plaque disruption and associated complications;[99–104] and stent-induced inflammation.[102] Protease-activated probes based on PEGylated poly-L-lysine have also been used as contrast agents for imaging infarcted myocardial tissue utilizing time-resolved fluorescence imaging.[105] A family of macromolecular enzymatically activated probes, including Prosense® and MMPSense®, is now commercially available (PerkinElmer, Inc.).

More recently, peptidic probes including both fluorescent molecules and quenchers

have been used for *in vivo* imaging of tumor fibroblast activation protein a (FAPa) peptidase in mice[137] and matrix metalloproteinases in osteoarthritis and cancer.[138,139] Enzymatically activated cell penetrating peptides consisting of hairpin structures linked together by a cleavable linker have been also recently used as thrombin-activated fluorescent contrast agents for atherosclerotic plaque[140] and as intracellular drug delivery systems in protease-overexpressing tumors.[141] Peptide dendrimers or branched structures containing cathepsin S peptide substrates as linkers for NIR fluorochromes have also been reported.[142] Similarly, enzymatically cleavable polypeptides have been used for the development of enzymatically controlled drug delivery system in the past.[143,144]

In addition to macromolecular contrast agents, research has begun on the development of nanoparticle-based activatable fluorescent nanoprobes. Crosslinked iron oxide nanoparticles have been used as carriers for NIR fluorescent dyes for combined magnetic resonance and optical imaging.[106–108] Gold,[109] silica,[110] and chitosan[111] nanoparticles have been more recently used as carriers for enzymatically activated fluorescent probes.

Compared to other nanoparticle-based protease probes,[109–111] the EANPs herein described offer a number of benefits. Compared to gold and silica based systems,[109,110] EANPs combine proven biocompatible and biodegradable polymers that easily assemble into core-shell nanostructures and that have been utilized as biomaterials in the drug delivery field for decades. Compared to polymeric protease activated nanoparticles,[111] EANPs were also designed to include surface modifications to enhance blood circulation and for incorporation of targeting agents, cancer-specific cleavable linkers for enzymatic development of NIR fluorescence, high loading of NIR fluorescent molecules, and a stable

yet degradable core that could act as a drug reservoir in future studies. This combination of properties is expected to offer significant improvements in selectivity and sensitivity that would encourage their use in clinical settings as contrast agents for non-invasive detection, monitoring of cancer, or fluorescence-guided tumor treatment. In addition to their applications in cancer imaging, EANPs could be utilized in the study of physiological enzyme kinetics, and in the detection and monitoring of enzyme-related diseases such as inflammation and vascular disease.

Nanoprecipitation of amphiphilic copolymer blends enabled facile assembly of multi-component nanoprobes. FTIR analysis corroborated incorporation of all copolymers within the nanoprobe structure. Polymer blends were utilized for facile inclusion of the two hydrophilic polymers PLL and PEG on the surface of the nanoprobes. Specifically, each of the two copolymers consisted of a single hydrophilic (PLL or PEG) and a single hydrophobic region (PLGA or PLA). The architecture of these copolymers enabled self-assembly of the nanoprobes into a core-shell structure in which the hydrophilic components were presented on the surface and interacted with the surrounding aqueous environment. The use of copolymer blends enables easy modification of the ratio of PLL and PEG presented on the surface of the nanoprobes simply by changing the mass ratios of the PLGA-PLL to PLA-PEG used for nanoprobe preparation, without the need for further synthesis of branched copolymers containing both PLL and PEG. The hydrophobic portions of the copolymers form the core of the nanoprobe. PLGA and PLA, both hydrophobic biodegradable polyesters, were utilized in this work to provide EANPs with drug loading capabilities that will be investigated in future work. These hydrophobic polymer blocks could be replaced with only PLGA (including PLGA polymers of different

lactide-to-glycolide ratio), only PLA, or even other hydrophobic polymers as needed to tune the biodegradation and drug loading capacity of the nanoprobes.

The ability to fluorescently label the nanoprobes after nanoassembly confirmed surface localization of PLL chains, as well as relatively hydrophilic and flexible environment of the nanoprobe shell. Dynamic light scattering and electron microscopy confirmed the nano-scaled size and spherical morphology of EANPs (Figure 3-5).

Unlike other contrast agents, EANPs are designed to provide both structural and functional information about the target tissue since their enzymatic dependence can convey clues about disease status and prognosis. Proteolytic enzymes play numerous roles in animal physiology and pathophysiology. Many diseases, including cancer, arteriosclerosis, inflammation, and vascular disease are associated with abnormal enzymatic activity.[145] Elevated expression of cathepsin B and D has been observed in ovarian, lung, colorectal, and breast cancer tissue, and has been correlated with poor patient prognosis.[146–149] Proteases have been investigated as triggers for drug delivery[144] and imaging of pathological events in combination with NIR fluorescent probes. Results of studies of *in vitro* enzymatic fluorescence activation with the model protease trypsin and in cultured cancer cells demonstrated the capabilities of our EANPs as enzymatically triggered contrast agents. PLL acted as an enzymatically cleavable carrier for NIR fluorescent molecules. Rationally functionalized polypeptide sequences that are known substrates to specific cathepsins and matrix metalloproteinases will be utilized instead of PLL in the future to provide more disease-specific activation. For example, polypeptide substrates containing the PLGVR amino acid sequence show selectivity for matrix metalloproteinases while the GFLG tetra peptide can be cleaved by cysteine proteases including Cathepsins

B, H, L and C[109,144,149,150].

Imaging studies in tissue phantoms showed the promising capabilities of EANPs as optical contrast agents for *in vivo* applications. As opposed to fluorescent molecules that absorb and emit light in the visible range, NIR imaging enables interrogation of deeper tissue due to minimal spectral overlap with physiological chromophores. In this work, *our collaborators demonstrated our ability to detect fluorescence from EANPs at concentrations as low as 28 μg/mL up to a depth of 4 mm within phantoms of optical properties similar to those of tissue*[14]. Enzymatically activated EANPs showed significantly increased fluorescence compared to non-activated EANPs in these tissue phantom experiments, suggesting that these nanoprobes could potentially enable tumor-specific imaging and image-guided therapeutic interventions.

Future studies will investigate the potential of these contrast agents for *in vivo* imaging in animal models of cancer, as well as their evaluation as theranostic agents that could be used for concurrent tumor imaging and drug delivery. The key benefits provided by EANPs for *in vivo* imaging compared to other contrast agents will be their targeting potential and high signal-to-background ratio. Compared to other enzymatically activated optical contrast agents, the size of EANPs will enable passive tumor targeting due to the enhanced permeability and retention effect. In addition, EANPs can be actively directed to a target by conjugation of agents such as antibodies, aptamers, or peptides to terminal carboxylic acid groups of the PEG chains which rest on the surface of the nanoprobes. Finally, the low fluorescence level of the nanoprobes prior to enzymatic activation ensures optimal conditions for optical imaging due to low background fluorescence.

Nanotechnology offers the possibility of creating complex multi-functional

structures that can provide solutions for numerous biomedical problems. EANPs are an example of such structures, offering a combination of properties that are key for a successful NIR optical contrast agent. Their macromolecular structure, in addition, can be envisioned as a depot for targeted drug delivery, thus enabling opportunities for the development of theranostic systems.

IV. DOXORUBICIN-LOADED AF750-LABELED POLYMER BASED NANOPROBES (NPS) FOR IMAGING AND THERAPY OF BREAST CANCER

4.1 Introduction

Theranostic nanoparticles carry imaging agents and drugs simultaneously. Various types of theranostic nanoparticles based on organic and inorganic materials have been developed over the last decade for imaging and treating cancer.[151] Due to biocompatibility and diversity of polymer based theranostic nanoparticles, they have become one of the most strongly studied platforms for image-guided therapy.

The U.S. Food and Drug Administration (FDA) has approved many polymers such as poly(lactic-*co*-glycolic acid) (PLGA), poly(lactic acid) (PLA), poly(ethylene glycol) (PEG), and poly(caprolactone) (PCL) for pharmaceutical and medical applications.[152] Polymer-based theranostic nanoparticles can be categorized as polymer conjugates, nanocapsules, polymersomes, dendrimers, hydrogels, micelles, and nanoparticles (NPs).[153]

Polymer conjugates offer several advantages such as longer plasma half-life, lower immunogenicity, higher aqueous solubility and stability, and improved tumor targeted drug delivery over traditional small molecular and macromolecular drugs.[153] These conjugates are made of a covalently bonded water-soluble polymer and a bioactive molecule.[154] There are many commercially available polymer–protein conjugates in the market. Oncaspar® poly(ethyleneglycol) (PEG)-L-asparaginase conjugate is used for treating acute lymphoblastic leukaemia. Neulasta™ PEGylated recombinant methionyl human granulocyte colony stimulating factor (G-CSF) is used for protecting cancer patients against the risk of infection following chemotherapy.[155] Different types of polymers are

under investigation for the development of theranostic polymer conjugates, such as *N*-(2-hydroxypropyl)methacrylamide (HPMA) copolymer, poly-L-lysine, and poly(L-glutamic acid).[156] HPMA copolymer contains multiple reactive groups, so it can be functionalized with imaging and targeting agents, and therapeutics at the same time as a theranostic platform. Zarabi *et al.* synthesized a HPMA-cRGD (cyclic Arg-Gly-Asp) theranostic conjugate for targeting tumor angiogenesis. This conjugate was covalently bound to an imaging agent Gd(III) that enabled *in vivo* imaging of these active targeting systems by magnetic resonance.[157]

Polymeric nanocapsules have a core-shell structure. Their inner liquid core is surrounded by a polymer membrane.[158] Polymeric nanocapsules can encapsulate both hydrophobic and hydrophilic components with acceptable encapsulation efficiencies. Liu *et al.* synthesized cationic amphiphilic block copolymer mPEG-PLGA-*b*-PLL. They made nanocapsules using this copolymer, anticancer drug adriamycin and siRNA via a double emulsion method. NIR fluorescent dye Cy5 was also encapsulated to monitor Huh-7 hepatic carcinoma tumor targeting with the nanocapsules.[159]

Polymersomes are made through the self-assembly of amphiphilic diblock or triblock copolymers. Their structure is very alike that of liposomes. Polymersomes are hollow spheres that contain an aqueous solution in the core surrounded by a bi-layer membrane. The bi-layer membrane is alike that of a cell membrane in that the hydrophobic polymer sections assemble in the middle of the bilayer and are separated and protected from the bulk outer aqueous medium and inner aqueous core by the hydrophilic blocks.[160] Depending on the hydrophilic to hydrophobic block ratio of amphiphilic copolymers, these polymers can form micelle structures, while others can form polymersomes. If the ratio of

hydrophilic part to total polymer mass is about ≤35%, the polymer will typically self-assemble into polymersomes. If this ratio is above 45%, micelles typically form; however, the three-dimensional structure of the block copolymer mostly depends on block length and preparation methods.[161] Doxorubicin for treatment and maghemite nanoparticles for MRI imaging were loaded into poly(trimethylene carbonate)-*b*-poly(L-glutamic acid) block copolymers by nanoprecipitation method forming theranostic polymersomes.[162]

Dendrimers are defined as three-dimensional, tree-like branched nano-sized polymeric architectures. Poly-amidoamines (PAMAM), polypeptides, and polyesters have been used for synthesizing of dendrimers for therapeutic and diagnostic applications.[163] High therapeutic and imaging agent loading can be achieved due to the dendrimer's branching architecture. [163,164] Xu *et al.* prepared a dendritic core-shell architecture for tumor imaging and drug delivery.[165] They used a hyperbranched polyglycerol core and biocompatible PEG shells to make dendrimers. They loaded doxorubicin for treatment, and an near infrared (NIR) fluorescence imaging dye, indotricarbocyanine, for optical imaging.[165]

Hydrogels are covalently or physically cross-linked polymer chains that can absorb over 99% water due to their hydrophilic groups in the polymer chains. They have lots of unique features such as high hydrophilicity, tunable structure, very high loading capacity, stimuli controlled drug delivery capabilities, and low nonspecific protein binding.[166] Park *et al.* developed hydrophobically modified glycol chitosan hydrogel nanoparticles for the combination of anticancer agents doxorubicin and fluorescein isothiocyanate (FITC) fluorescent imaging agents.[167]

Polymeric micelles are self-assembled core-shell structured supramolecular nanoparticles based on amphiphilic block copolymers. The hydrophobic core is used as a reservoir for carrying imaging and/or therapeutic agents. The hydrophilic shell protects the micelle from rapid clearance and can carry imaging and/or targeting agents. Micelles can be formed by a variety of biocompatible amphiphilic copolymers. The core materials can be polyesters, polyamides, and polyethers such as PLGA, poly(lactic acid) (PLA), poly(caprolactone) (PCL), poly(L-aspartate), poly(propylene oxide), etc.[168] PEG is the most commonly used hydrophilic polymer that minimizes NP clearance by the reticuloendothelial system, prevents NPs from aggregation, and prolongs NPs half-life circulation in the body.[122] Poorly water soluble or non-water soluble drugs can be loaded with high entrapment efficiency on the hydrophobic core of polymeric micelles. Their size is relatively small compared to some other nanoparticles and they have optimal properties for tumor accumulation through passive targeting.[168] PLA-PEG polymeric micelles (Genexol®-PM) have been approved for use in breast cancer therapy in Europe.[169] Tsai *et al.* developed a multifunctional micelle structure using amphiphilic block copolymers. NIR dye Cy5.5 for imaging and folate for targeting were conjugated to the end of PEG-*b*-PLA. Doxorubicin was encapsulated within the core of the micelles for treatment of cervix adenocarcinoma.[170]

Doxorubicin (DOX) is one of the most commonly used chemotherapeutic drug with an Adriamycin as is trade name. It has been using for treatment of several different types of cancer such as leukemia, lung, breast, stomach, ovarian, soft tissue sarcoma, etc.[171] DOX intercalates into base pairs of DNA, and localizes in the minor groove of the double helix.

The progression of the enzyme topoisomerase II which winds DNA for transcription is inhibited by DOX intercalation.[172,173]

To reduce the systemic toxicity of DOX caused by its conventional administration, DOX was encapsulated within PEGylated liposomes to make it more targetable for tumors.[174,175] PEGylated liposomal doxorubicin improves pharmacokinetic and biodistribution profile of DOX, resulting in a decrease in DOX-related toxic effects, especially cardiotoxicity. However, these liposomes cause a dermatologic toxic reaction which is known as hand-foot syndrome[176,177] It has been hypnotized that PEGylated liposomal doxorubicin may extravasate from the deeper microcapillaries in the hands and feet and accumulate promoted by the hydrophilic coating of the liposomes. The penetration of DOX into deeper skin layers, where its radicals will be formed and react with epidermal cells may cause this syndrome.[176] Because of this reason, the novel drug delivery systems based on polymeric micelles for encapsulation of DOX has been developed.[178–181]

DOX has inherent fluorescence feature due to its central anthracycline chromophore group. DOX distribution in various tissues or cells can be viewed under fluorescence imaging system in visible range.[171] However, absorption and emission interferences between DOX and biological chromophores such as hemoglobin, oxyhemoglobin, melanin don't allow to DOX as an efficient imaging agent for diagnosis and monitoring tumor, especially *in vivo*. This is the reason other imaging agents such as NIR imaging agents need to be used for monitoring tumor.

Due to advantages of polymeric micelle type of nanoparticles as a carrier, NIR fluorescent optical imaging with less interferences with biological chromophores, and effectiveness of DOX for treatment breast cancer, a theranostic system can be developed

for imaging and treatment of any invasive breast cancer type. In this work, theranostic NPs were prepared to use for NIR imaging and DOX delivery to MDA-MB-231 breast cancer cells. The cell line, MDA-MB-231, is highly invasive ductal carcinoma cells. This cell line is known as triple-negative because both hormone receptors (estrogen and progesterone) and human epidermal growth factor receptor 2 (HER2) are negative, that is their expression on the cells is minimal. Triple-negative cancer cells don't respond to hormonal and HER2 receptor-targeted therapies because these hormones don't support their growth. This cell line represents a more aggressive, higher grade, and more likely recurrent tumor type than other types of breast cancers.[182,183]

Our theranostic NPs are designed in such a way that NIR fluorescence contrast is activated by proteolytic enzymes that are overexpressed in tumor tissues. High level of proteases is involved in the progression, and tumor growth both at primary and metastatic sites. Tumor margins secrete high amounts of proteases to degrade the basement membrane and extracellular matrix (ECM) and open more space up for tumor growth.[95,184–186] Peptide-based NIR fluorescence imaging probes have been broadly studied as targeting optical probes for image-guided drug delivery, and for monitoring of drug pharmacokinetics, distribution, and tumor accumulation in real time.[187] These probes can interact with proteases overexpressed by tumors such as cathepsins, matrix metalloproteases (MMPs) and trypsin.[90,188–191] Overexpressed trypsin associates with different types of diseases such as colorectal, pancreatic, breast cancer and atherosclerosis.[192] Highly invasive metastatic breast carcinoma cell lines secrete overexpressed trypsin enzyme, leading to autocrine activation of cell surface protease-activated receptor-2 (PAR-2).[193] PAR-2 is

overexpressed in a variety of breast cancer cells such as MDA-MB-231 and causes cell growth, migration, and invasion.[194–196]

We prepared enzymatically-activated NIR fluorescent probes (EANPs) by nanoprecipitation of blends of poly(lactic acid)-*b*-poly(ethylene glycol) and poly(lactic-*co*-glycolic acid)-*b*-poly-L-lysine in our previous work,[14] as described in Chapter III. The protease (trypsin)[197] cleavable polypeptide poly-L-lysine (PLL) was covalently decorated with the near infrared (NIR) fluorescent molecule. These molecules became fluorescent when PLL chains were cleaved enzymatically by proteases.[14]

In this chapter, enzymatically activated and chemotherapeutic drug loaded theranostic nanoparticles were synthesized using common biocompatible and biodegradable amphiphilic copolymers. The synthesis and characterization of copolymers, conjugation of NIR dye on polypeptide, drug loading and release, and characterization of nanoparticles, as well as the *in vitro* evaluation of the function of the nanoparticles as imaging and therapeutic agent will be discussed.

4.2 Materials and Methods

4.2.1 Materials

An acid terminated poly(lactic-co-glycolic acid) (PLGA) copolymer with carboxylic acid terminal group (PLGA-COOH) was bought from Corbion Purac (Netherlands). The molecular weight of PLGA-COOH was 17 kDa with a 50:50 D, L lactide: glycolide molar ratio and with an inherent viscosity midpoint of 0.2 dl/g. Heterofuntional poly(ethylene glycol) (OH-PEG-COOH) with 5 kDa molecular weight was obtained from Laysan Bio (Arab, AL). Heterofunctional poly(ethylene glycol) methyl

ether (OH-PEG-OMe, Mn 5 kDa), poly-L-lysine hydrobromide (PLL, MW 3.8 kDa), poly-D-lysine hydrobromide (PDL, MW 3.8 kDa), *N*-*α*-tosyl-*L*-Lysine chloromethyl ketone hydrochloride (TLCK), *N,N'*-dicyclohexylcarbodiimide (DCC), trypsin solution from porcine pancreas (10x, 25 g/L solution in 0.9% sodium chloride), and bovine serum albumin (BSA) were acquired from Sigma-Aldrich (St. Louis, MO). *N*-hydroxysuccinimide (NHS) was purchased from ThermoScientific (Waltham, MA).

3,6-dimethyl-1,3-dioxane-2,5-dione (D,L-lactide), *N*-(dimethylaminopropyl)-*N'*-ethylcarbodiimide HCl (EDC), tin(II) 2-ethylhexanoate (stannous octoate, $Sn(Oct)_2$), doxorubicin hydrochloride (DOX HCl), triethylamine (TEA), and thiazolyl blue tetrazolium bromide (MTT) were obtained from Alfa Aesar (Ward Hill, MA). Alexa Fluor 750 succinimidyl ester (AF750) was obtained from Molecular Probes (Life Technologies, Carslbad, CA). CellTiter-Glo® Luminescent cell viability assay was obtained from Promega (Madison, WI). Toluene, methanol, acetone, dimethyl sulfoxide (DMSO), dimethyly formamide (DMF), and diethyl ether solvents were ACS grade. Ultrapure deionized water was obtained from a Millipore Direct Q system.

4.2.2 Instrumentation

The structure of copolymers was characterized using proton nuclear magnetic resonance spectroscopy (^{1}H-NMR) with a Bruker Avance 400 NMR. Fourier transform infrared spectra (FTIR) were aquired a Bruker Tensor 27 FTIR spectrometer with attenuated total reflectance (ATR) attachment. UV-Vis-NIR-Luminescence measurements were obtained using a BioTek Synergy™ 4 Hybrid Microplate Reader. SEM images were obtained using an FEI Helios Nano Lab 400 scanning electron microscope. SEM samples

were coated with 2 nm of iridium using an EMS Quorum EMS150T ES turbo-pumped sputter coater. TEM images were obtained using a JEOL JEM 1200 EXII microscope with a Gatan Orius CCD digital camera. Dynamic light scattering measurements were obtained using a Malvern Zetasizer Nano ZS. A VWR® symphony™ Ultrasonic Cleaner was used for resuspending of NP pellets. Beckman Coulter Avanti J-26 XPI centrifuge was used to purify polymers and NPs.

4.2.3. Cell Culture

MDA-MB-231 human mammary adenocarcinoma cells were obtained from the American Type Tissue Collection (ATCC). Cells were grown in Dulbecco's Modified Eagle's Medium (DMEM) supplemented with 10% fetal bovine serum (FBS), 1% HEPES, and 1% Pen/Strep in a 37 °C humidified incubator with a 5% CO_2 and 95% air atmosphere.

4.2.4 Synthesis of PLGA-PLL or PLGA-PDL

The detailed explanation of PLGA-PLL synthesis was given in section 3.2.2. PLGA (0.5 g), DCC (0.062 g) and NHS (0.035 g) were dissolved in 4 mL of dimethyl formamide and reacted for four hours to activate PLGA under argon purging while stirring. PLGA: NHS: DCC molar ratio was 1:10:10.

Activated PLGA (PLGA-NHS) was reacted with 0.121 grams of PLL in the presence of 8.43 μL TEA. PLGA: PLL: TEA molar ratio was 1:1:2. Figure 4-1 shows the reaction scheme of PLGA-PLL conjugation. An identical method was utilized for the preparation of PDL, which is used as a non protease-labile control in this work.

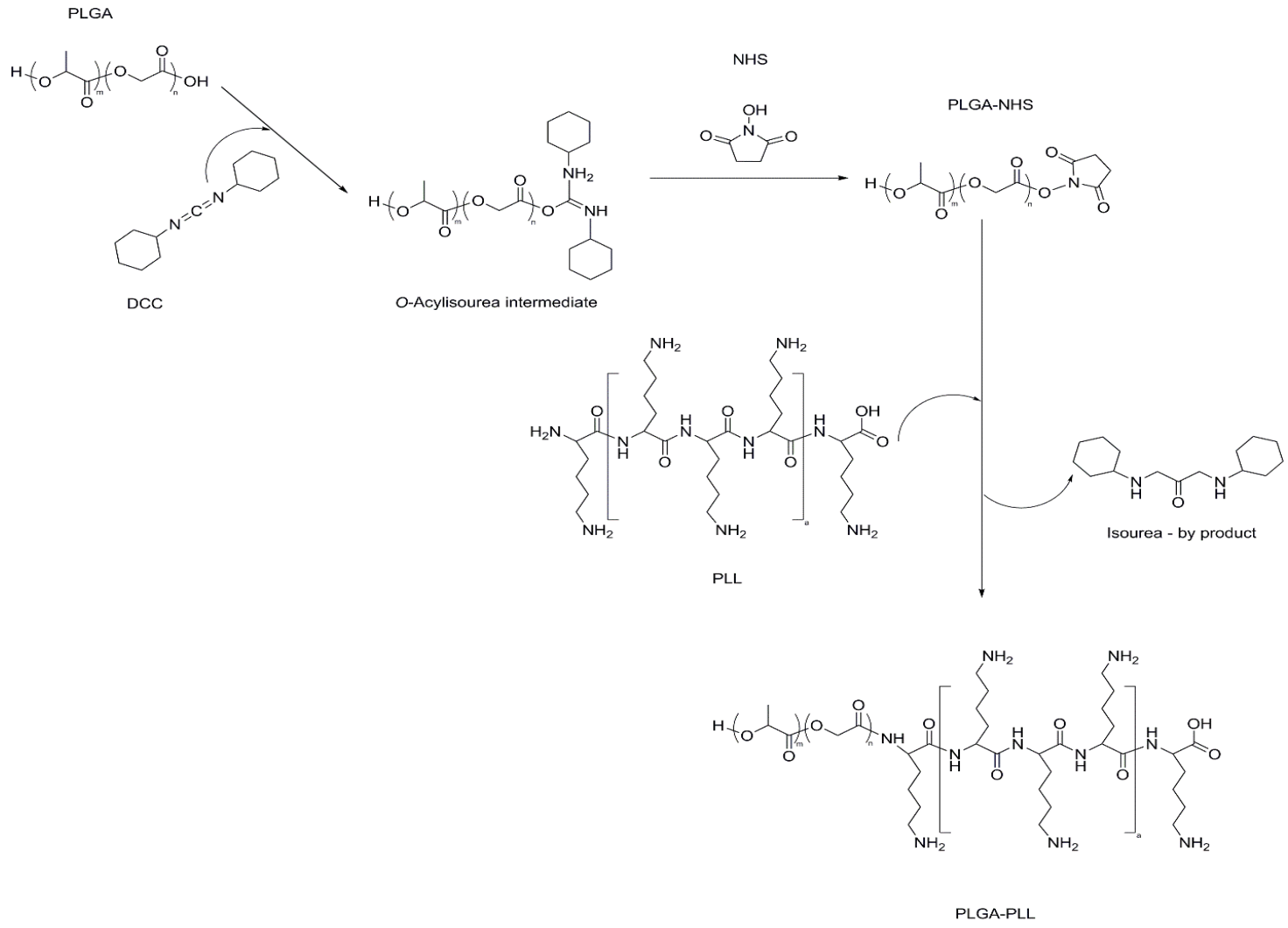

Figure 4-1. Synthesis of PLGA-PLL copolymer.

4.2.5 Synthesis of PLA-PEG-COOH and PLA-PEG-OMe

The PLA-PEG copolymers were synthesized via ring opening polymerization of lactide. D,L-lactide and carboxylated or methoxylated PEG reacted in the presence of stannous octoate. Then, copolymers were precipitated and dissolved for purification. The synthesis scheme is shown in Figure 4-2.

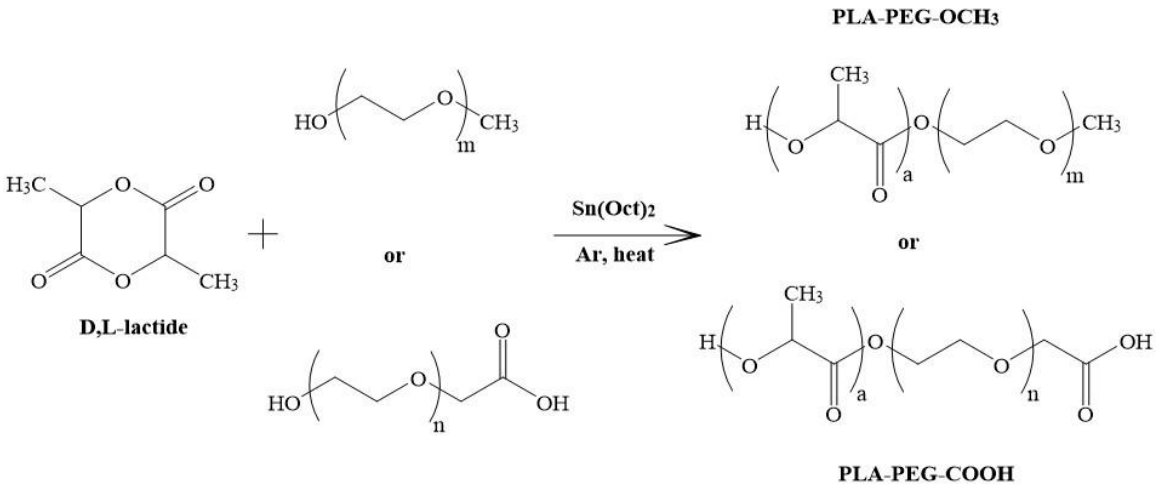

Figure 4-2. Synthesis of PLA-PEGs copolymers.

4.2.6 Conjugation of Fluorescent Dye to PLGA-PLL or PLGA-PDL Copolymer

PLGA-PLL copolymer (6.25 mg) was dissolved in 125 µL of DMF. A mass of 0.3 mg of AF750 NIR fluorescent dye in 300 µL DMF was added into the copolymer solution in the presence of 13.25 µL TEA for 12 hours in the dark at room temperature. The theoretical feed molar ratio of AF750/PLL is 2.5. AF750 NHS ester reacts with primary amines on PLL forming stable amide bonds. PLGA-PLL-AF750 polymer conjugate was purified by three cycles of precipitation in ice-cold methanol and dissolution in acetone to remove unbound AF750, and then dried under vacuum. An identical method was used for

the fluorescence labeling of PLGA-PDL which acted as a non-activatable fluorescence control in our studies.

4.2.7 Preparation of NPs

For preparation of the drug-loaded NPs, DOX HCl was converted to its hydrophobic free base form. DOX HCl was dispersed in 12.5% v/v methanol in acetone, and deprotonated using TEA (1:5 molar ratio of DOX to TEA) at 3.5 mg/mL. After overnight reaction, the clear solution of DOX free base (DOX) was evaporated and left-over solvents were freeze dried. Figure 4-3 shows images of the initial DOX HCl dispersion in methanol/acetone mixture and then of the solution that results after reaction in the presence of TEA.

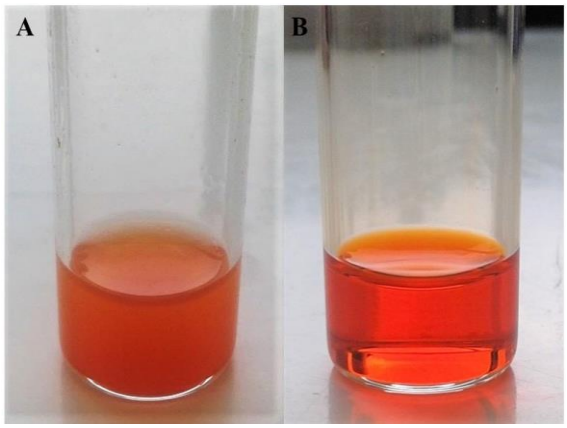

Figure 4-3. The conversion of DOX HCl to DOX free base. (A) Before adding TEA (B) After overnight reaction with TEA.

NPs were prepared by nanoprecipitation of blends of PLGA-PLL-AF750 or PLGA-PDL-AF750, PLA-PEG-COOH, PLA-PEG-OMe, and DOX free base. DOX was dissolved in dimethyl sulfoxide (DMSO) at 3.5 mg/mL. Each of the three copolymers were dissolved in acetone separately at 50 mg/mL. The polymer blend (187.5 µL including 125 µL of PLGA-PLL-AF750, 31.25 µL of PLA-PEG-COOH, and 31.25 µL of PLA-PEG-

OMe) and DOX free base solution (141 µL) were combined in acetone (500 µL) and methanol (86 µL). The final polymer concentration was 10.25 mg/mL in the organic phase. The mixed solution (mass ratio of PLGA-PLL-AF750: PLA-PEG-COOH: PLA-PEG-OMe = 4:1:1) was then added dropwise to 3.75 mL of a stirring aqueous solution of 10 mg/mL bovine serum albumin (BSA) to enable NP formation via nanoprecipitation. DOX-loaded NPs without AF750 were also prepared as described but utilizing PLGA-PLL or PLGA-PDL instead of the fluorescently labeled copolymers.

Blank NPs (no DOX, no AF750) were prepared by nanoprecipitation of blends of PLGA-PLL (125 µL), PLA-PEG-COOH (31.25 µL), PLA-PEG-OMe (31.25 µL), DMSO (141 µL), acetone (500 µL) and methanol (86 µL) in 3.75 mL of solution of 10 mg/mL BSA aqueous solution.

NPs were washed five times with 10 mg/mL bovine serum albumin in DI water by centrifugation at 74,200 x g for an hour at 4 °C. The NP pellet was resuspended with 1X phosphate buffered saline (PBS) after the last centrifugation for further studies. Figure 4-4 shows the different types of NP suspensions.

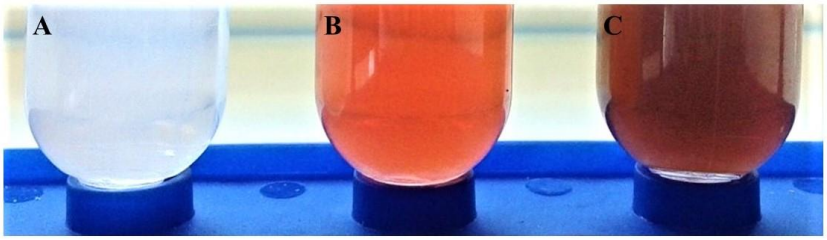

Figure 4-4. NP suspensions in PBS (A) Blank NPs (B) DOX NPs (C) AF750-DOX NPs.

The size of NPs was determined using dynamic light scattering (DLS) and zeta-potential of the NPs was determined using laser Doppler micro-electrophoresis. This

technique is used to measure the movement of charged particles in an electric field that applies Doppler effect. The particle mobility is determined from the known applied electric field and measured particle velocity. Zeta potential is then calculated from mobility using the Smoluchowski model.[198] For zeta-potential measurements, a few drops of aqueous NP suspension were added into 1 mL of 1 mM potassium chloride (KCl). A dip cell electrode was then used to determine the zeta-potential of NPs.

The size and morphology of NPs were imaged by transmission electron microscopy (TEM) and scanning electron microscopy (SEM). NP suspensions were dried on carbon-coated 200-mesh copper grids, and stained with 2% aqueous uranyl acetate for TEM imaging. For SEM imaging, a drop of NP suspension was dried on a silicon wafer. The NPs were then coated with iridium (2 nm thickness) before SEM imaging.

4.2.8 Loading Percentage and Entrapment Efficiency of DOX

The percentage of drug loading and entrapment efficiency of DOX-free base in NPs were determined using a Biotek H4 multimode plate reader (λ_{Ex} = 500 nm, λ_{Em} = 600 nm). A known mass of freeze-dried NPs was dissolved in a known volume of DMSO. For determining drug loading percentage, the concentration and mass of DOX in NPs were determined based on a standard curve of DOX in DMSO by fluorescence spectroscopy. The supernatants collected during purification process were analyzed based on a standard curve of DOX HCl in water to find entrapment efficiency. The percentage of drug loading and entrapment efficiency were determined by utilizing equation 1 and 2.

$$\text{Drug Loading \%} = \frac{mass\ of\ DOX\ in\ NPs}{mass\ of\ NPs\ recovered} \text{ x } 100 \qquad (1)$$

$$\text{Entrapment Efficiency \%} = \frac{mass\ of\ DOX\ in\ NPs}{mass\ of\ total\ DOX\ fed\ initially} \text{ x } 100 \quad (2)$$

4.2.9 Enzymatic Activation of NP Fluorescence

DOX-loaded AF750 labeled NPs were diluted in PBS to 1/10th the concentration of the NP stock (0.2 mg/mL, value based on the known mass of NPs after freeze drying). A Biotek H4 multimode plate reader was used to determine the fluorescent enhancement of the NPs (λ_{Ex} = 740 nm, λ_{Em} = 780 nm). Four repetitions were done for each sample. NPs were incubated with 1X PBS buffer (10 mM), and exposed to 10X trypsin (25 g/L) together with the protease inhibitor TLCK (initial concentration, 30 mg/mL) were used as controls. The mixture of 50 µL of 0.2 mg/mL NP suspension and 40 µL of 1X PBS was read as the starting sample fluorescence. Then, 30 µL of 10X trypsin (time zero) was added onto the starting sample and fluorescence development was recorded at specific intervals up to four hours. The molar ratio of Trypsin: TLCK in the mix was 1 for control studies including this protease inhibitor. Fluorescence readings were normalized with respect to the control consisting of NPs exposed to PBS only.

The same study was carried out with NPs contained PLGA-PDL copolymer to show lack of fluorescent development based on trypsin's lack of reactivity on PDL. Paired, two-tailed t-test were used to determine statistical differences between individual conditions and the control (NPs exposed to PBS).

4.2.10 *In Vitro* Drug Release Study

Drug (DOX) release from NPs was studied using a dialysis method. D-Tube Dialyzer Mini (MWCO 12-14 kDa) (EMD Millipore) tubes were filled with 180 µL of 2

mg/mL NP suspension (actual mass of DOX in NPs was 0.28 mg, based on loading and determination of the known mass of NPs after freeze drying). Dialyzer tubes were immersed in 5 mL of 1X PBS buffer solution (release medium, pH = 7.4) at 37 °C and continuously stirred at 200 rpm using a OptiMag Plus hot plate stirrer with a round dry block for 20 mL scintillation vials that was graciously borrowed from Dr. Jennifer Irvin's laboratory. DOX hydrochloride solution in DI water at the same concentration of DOX-free base in NPs was used as control and release medium were collected for 24 hours, when complete dialysis of DOX HCl was visually observed to be complete and as determined in preliminary experiments. Four independent replicates were used for each sample. 120 μL aliquots of the release medium were collected for analysis at different time intervals and replaced with fresh 120 μL of 1X PBS buffer at 37 °C. DOX-free base NP release runs were continued for 30 days. Samples were stored at -25 °C until the end of the study. At the end of the study, DOX-NPs in dialyzer tubes were freeze dried and dissolved in DMSO. The fluorescence of DOX in the collected samples and NPs in dialyzer tubes was read with a Biotek H4 multi-mode plate reader at λ_{Ex} = 500 nm, λ_{Em} = 600 nm. The mass released at each time point was determined using a standard calibration curve.

4.2.11 Determination of NP Cytocompatibility

MDA-MB-231 cells were cultivated in complete DMEM medium at 37 °C and 5% CO_2. After that, the cells were harvested with 0.25% Trypsin-EDTA solution (Sigma). Then, cells were seeded in black clear-bottom 96-well plates at a density of 7,500 cells/well with 100 μL of complete cell culture medium. After 36 hours of incubation, the growth medium was replaced with suspensions of blank (DOX-free, AF750 free) NPs in the

concentration range of 2000 μg/mL to 0.02 μg/mL by 1/10th dilution and cells were incubated for 72 hours. Cells cultured in complete media without NPs represent the positive control (+) and cell-free wells with serum-free medium were used as negative control (-).[199] After the period of exposure, the media was replaced with 100 μL of CellTiter-Glo™ luminescence mixture. This mixture was prepared by dissolving the lyophilized CellTiter-Glo™ substrate (1 vial) in CellTiter-Glo™ Buffer (100 mL), as specified by the manufacturer. The mixture was diluted by 1:5 with 1X TRIS buffer (250 mM TRIS, 27 mM KCl, 1.37 M NaCl, 10% Glycerol, 1% Triton X-100) before use in the cells. The 96-well plate was mixed for 2 minutes on a shaker, and after a 10-minute incubation at 37 °C, the emitted luminescence was detected using a Biotek H4 multi-mode plate reader. The luminescence (λ_{Em} = 540/35 nm) of six repeat wells for each concentration were read.

To determine the cytocompatibility of blank NPs (DOX-free, AF750 free), we also used MTT assay. MDA-MB-231 cells were seeded in transparent 96-well plates at a density of 7500 cells/well with 100 μL of complete cell culture medium. The growth medium was replaced with blank NP suspensions in the concentration range of 1000 μg/mL to 7.8 μg/mL by half dilution and cells were incubated for 72 hours after 24 hours of incubation. Cells cultured in complete media without NPs represent the positive control (+) and cells treated with methanol for 15 minutes before adding MTT reagent were used as negative control (-). After the period of exposure, the media was replaced with 100 μL of MTT reagent. After 3.5 hours incubation, the media was carefully removed and the formazan crystals were dissolved in 100 μL of DMSO. The formazan's absorbance peak was read at 590 nm with a Biotek H4 multi-mode plate reader.

Paired, two-tailed t-test were used to determine statistical differences between individual conditions and the control (cells incubated in full media).

4.2.12 Determination of NP Therapeutic Efficacy

The therapeutic efficacy of DOX-NPs was determined with the CellTiter-Glo™ luminescence assay. MDA-MB-231 cells were plated at 7,500 cells/well in black clear-bottom 96-well plates with 100 μL of complete cell culture medium. After 36 hours of incubation, the growth medium was replaced with suspensions of DOX-NPs in the drug concentration range of 100 μM to 0.001 μM by 1:10th dilution and cells were incubated for 72 hours. DOX free base and DOX HCl solutions in the concentration range of 100 μM to 0.001 μM were also used as controls for therapeutic efficacy study. For dilution of DOX free base, 1% DMSO in media was used to maintain DMSO content constant at different concentrations since this form of the drug is not directly soluble in aqueous solutions. Cells cultured without NPs/drug in complete media and cells without NPs/drug in complete media containing 1% DMSO were the positive (+) controls for the DOX HCl and DOX free solution studies, respectively. Cell-free wells with serum free medium were used as negative control (-). The viability was determined with luminescence assay.

To monitor therapeutic efficacy of DOX NPs in a narrow concentration range, cells were also incubated with 100, 85, 70, 55, 40, 25, and 10 μM of DOX NPs for 72 hours and the luminescence assay was performed.

4.2.13 NP-Cell Interactions

MDA-MB-231 cells were plated on 8-well LabTek™ chambered coverslips at a density of 50,000 cells per well in 0.3 mL of media. The cells grew under normal culture conditions 24 h prior to beginning the studies. The cell media was replaced with the NP suspensions at 0.2 μg/mL concentration. After incubation for specific time periods (24 h, 48 h, 72 h and 96 h), the cells were washed three times with Dulbecco's Phosphate-Buffered Saline (DPBS) and fixed using 3.7% formaldehyde in PBS. The interaction of the NPs with the cells was monitored over time with an AMG EVOS FL LED-based fluorescence microscope utilizing a Cy-7 filter cube (Ex: 710/40 nm, Em: 775/46) with embedded monochromatic camera. The delivery of DOX-free base to the cells was also monitored with the fluorescence microscope utilizing an RFP filter cube (λ_{Ex} = 531/40, λ_{Em} = 593/40). NPs (AF750-labelled DOX-loaded) containing PLGA-PDL copolymer were used as control for monitoring fluorescent development on imaging studies.

4.3 Results

4.3.1 Synthesis of PLGA-PLL, PLGA-PDL, PLA-PEG-COOH and PLA-PEG-OMe

The PLGA-PLL and PLGA-PDL copolymers were synthesized by carbodiimide-mediated coupling of acid-terminated PLGA and PLL. PLGA-PLL copolymer was characterized using ^{1}H-NMR spectroscopy. Figure 4-5 shows the ^{1}H-NMR spectra of PLGA-PLL in deuterated dimethylsulfoxide (DMSO-d6). NMR spectra confirmed the presence of PLGA and PLL in the copolymer. Proton peaks for PLL were assigned as previously reported:[14] β, γ, and δ protons at 1.2 ppm (6H), ε protons at 2.8 ppm (2H), and α proton at 4.0–4.5 ppm (1H). PLGA proton peaks correspond to lactide methane quartets

and methyl doublets at 5.2 ppm (1H) and 1.6 ppm (3H), respectively, and glycolide methane protons 4.8 ppm (2H).

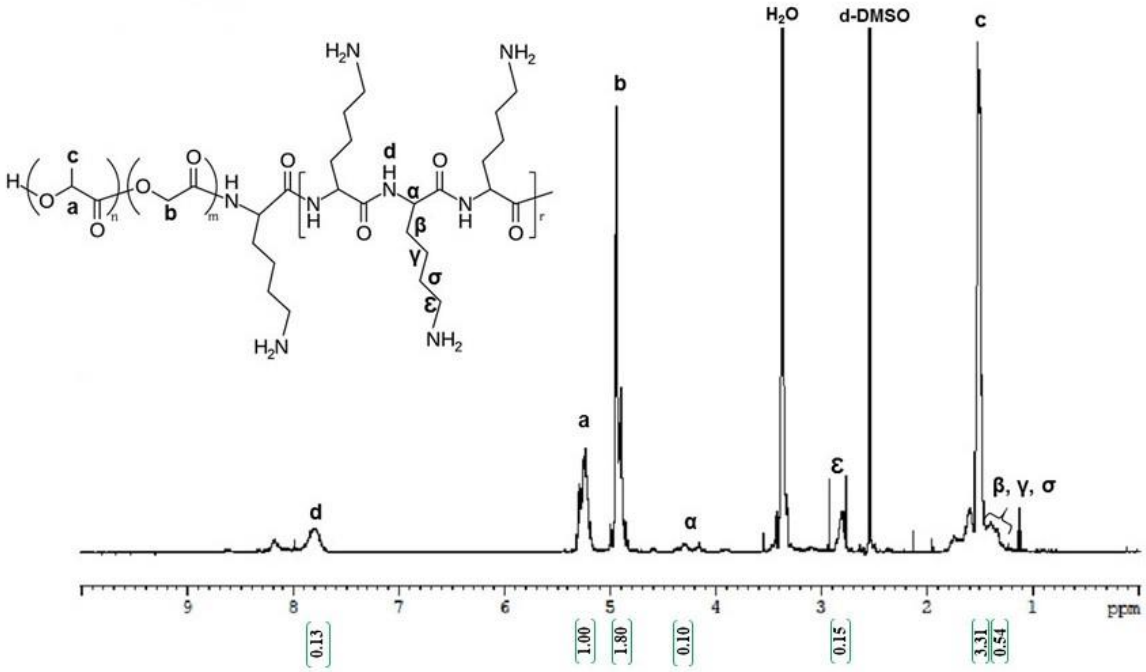

Figure 4-5. ^{1}H-NMR spectrum of PLGA-PLL.

The composition of PLGA-PLL copolymer was also confirmed by Fourier transform infrared spectroscopy (FTIR). Figure 4-6 shows the FTIR spectra of PLGA, PLL, and PLGA-PLL copolymer. The spectrum of PLGA (red line) shows the and alkyl C-H stretch at 2950 – 2850 cm^{-1}, characteristic ester C=O stretch absorption peak at 1750 -1735 cm^{-1}, and C—O—C stretch peak at 1250 - 1050 cm^{-1}, respectively.

The spectrum of PLL (blue line) shows a broad medium band for primary amines N-H stretch peak at 3500 - 3350 cm^{-1}, characteristic strong amide C=O stretch peak (amide I band) at 1690 - 1630 cm^{-1}, and broad and strong N-H bend (amide II band) peak at 1510 - 1580 cm^{-1}, respectively.

The spectrum of PLGA-PLL is indicated with green color. PLL amide I and amide II bands, alkenyl stretch peak at 3100 – 3010 cm^{-1} and PLGA ester C=O stretch absorption peak, C—O—C stretch peak, and alkenyl stretch peak confirm the presence of both blocks in the copolymer.

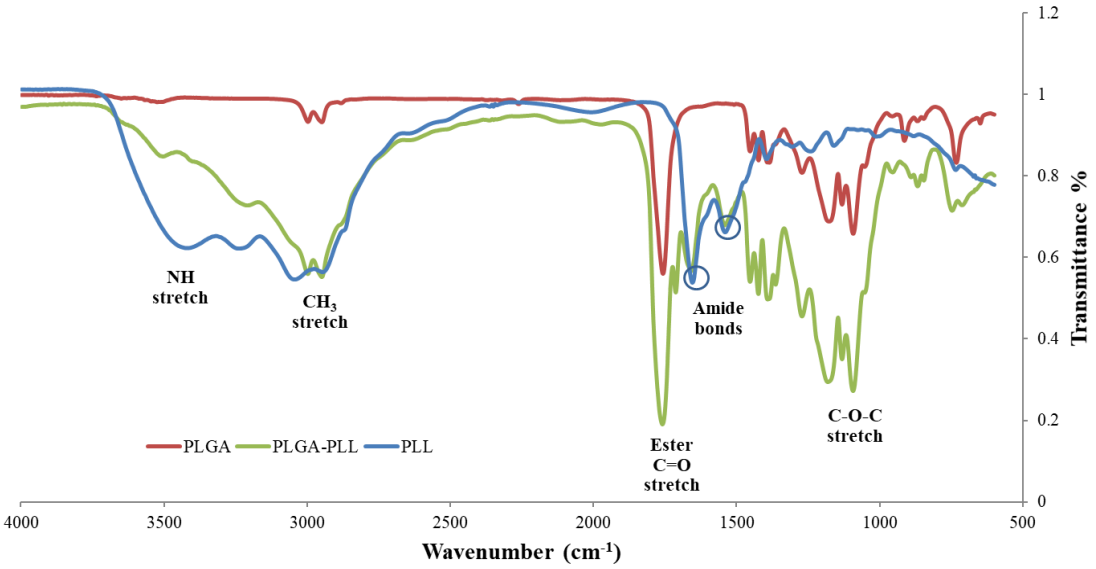

Figure 4-6. FTIR spectra of PLGA, PLL and PLGA-PLL.

The PLA-PEGs copolymers were synthesized via the ring opening polymerization of lactide initiated by terminal hydroxyl groups of heterofunctional PEGs. Poly(lactide) protons at 1.6 (3 H) and 5.2 (1 H) ppm, and PEG protons at 3.6 ppm (1.8 H) were confirmed PLA-PEG-OMe copolymer composition, as shown for PLA-PEG-OMe in Figure 4-7. The molecular weight of PLA-PEGs was calculated by comparing the area of PEG protons with that of poly(lactide). The molecular weight of polymers was determined to be 21,200 Da for PLA-PEG-COOH and 23,180 Da for PLA-PEG-OMe. The same batch of PLA-PEG-COOH on Chapter III was used for this chapter's studies. The proton NMR spectrum was shown on Figure 3-5.

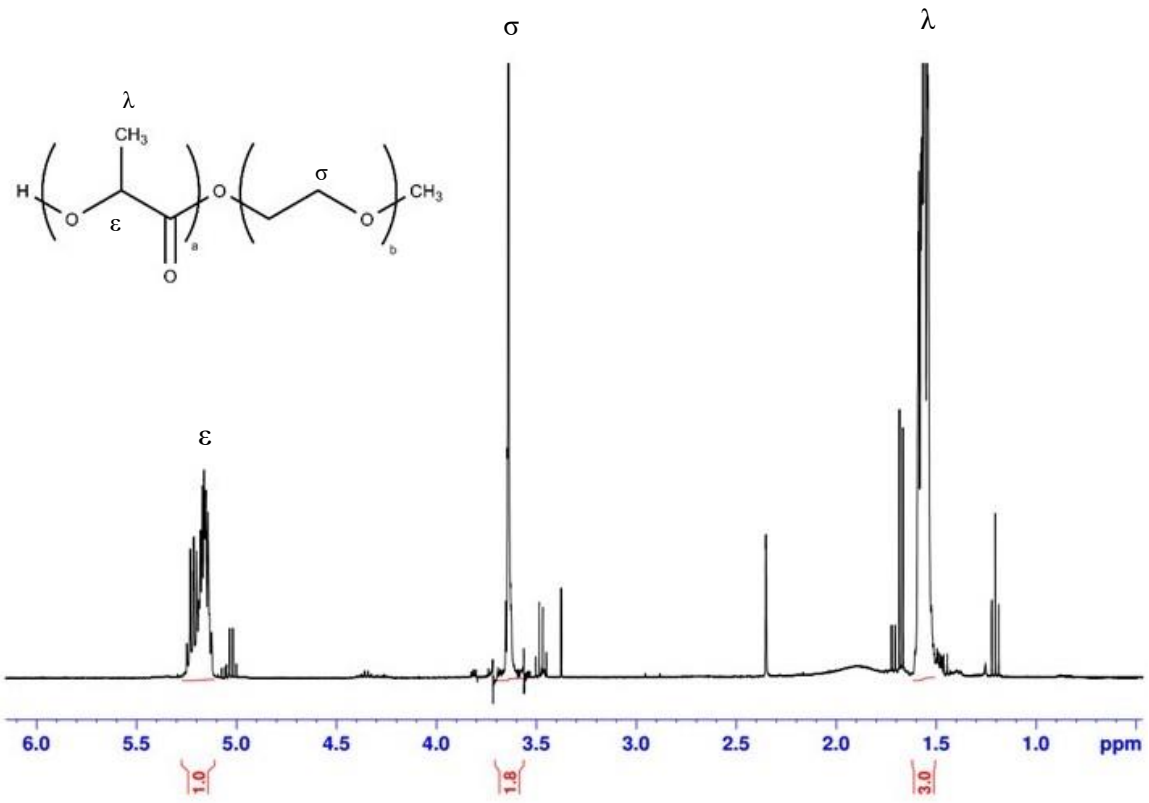

Figure 4-7. ^{1}H-NMR spectrum of PLA-PEG-OMe.

The structure of PLA-PEG-COOH and PLA-PEG-OMe copolymers was also confirmed by FTIR (Figure 4-8). The copolymers present peaks for C-H bonds of alkyl groups at 2800-2950 cm^{-1}, ether C—O—C stretch at ~1100 cm^{-1}, carboxylic acid OH stretch peak at 3500 cm^{-1}, and C = O of COOH in PEG at 1635 cm^{-1} associated with the PEG block of PLA-PEG-COOH. The characteristic sharp C=O stretch peak at ~1755 cm^{-1} of the PLA polyester block and alkyl absorption peaks at 2950-3000 cm^{-1} were confirmed. The peak at ~2400 cm^{-1} indicates CO_2 which comes from atmosphere while running samples. The FTIR spectrum indicates the formation of PLA-PEG block copolymer.

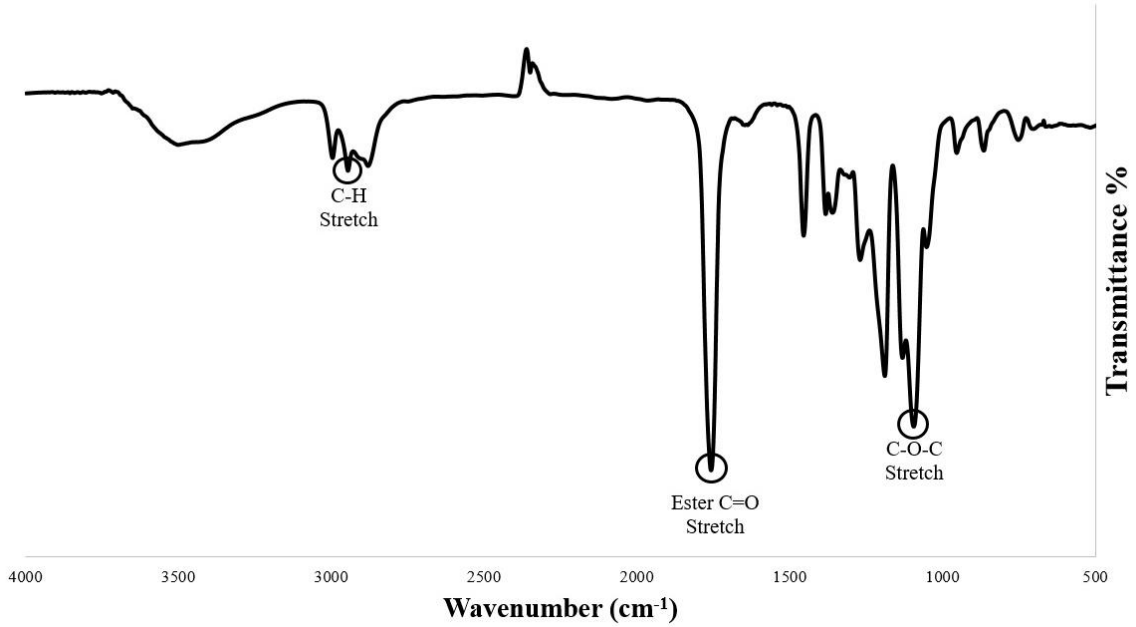

Figure 4-8. FTIR spectra of PLA-PEG-COOH.

4.3.2 Conjugation of Fluorescent Dye to PLGA-PLL or PLGA-PDL

The PLL and PDL moieties of PLGA-PLL and PLGA-PDL were covalently decorated with the AF750 NIR fluorescent molecules. Figure 4-9 shows that AF750-labeled PLGA-PLL copolymer and non-labeled PLGA-PLL copolymer after purification. The dark blue color of AF750-PLL-PLGA copolymer was indication of successful conjugation reaction between AF750-NHS ester and PLL primary amine groups.

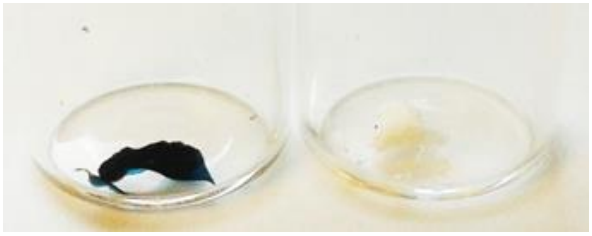

Figure 4-9. PLGA-PLL-AF750 copolymer vs PLGA-PLL copolymer.

4.3.3 Preparation of NPs

NPs were prepared via nanoprecipitation of a blend of amphiphilic copolymers in an aqueous solution. Figure 4-10A shows the absorbance spectrum of NP suspension in water. While DOX free base absorbs and fluoresces at 500 nm and 600 nm, AF750 absorbs and fluoresces at 740 nm and 780 nm, respectively. The spectral separation between DOX and AF750 is sufficient to ensure that there is no optical interference during spectroscopic quantification of these dyes or fluorescence microscopy. To confirm size and morphology of AF750-DOX NPs, TEM and SEM were used (Figure 4-10B-E). The average size of the spherical NPs was found to be approximately 66 nm.

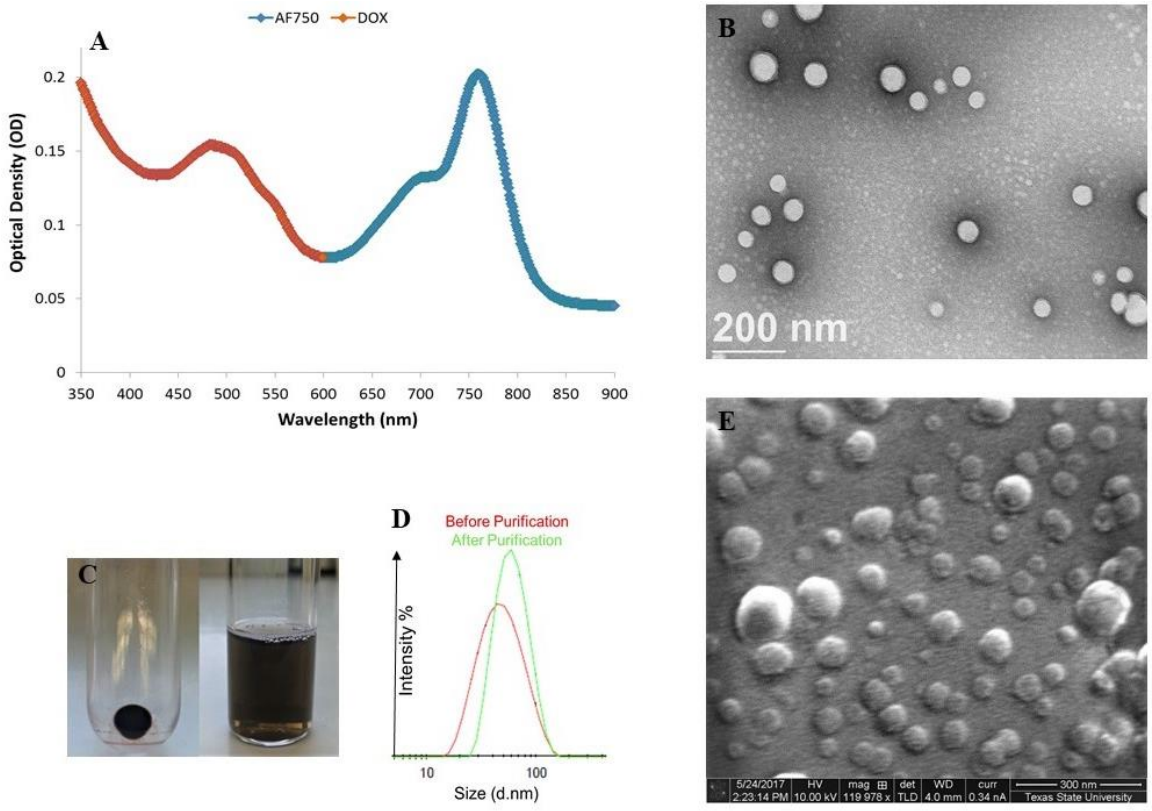

Figure 4-10. NP Characterization. (A) Absorbance spectrum of NPs in water. (B) Transmission electron microscopy image. (C) NP pellet and suspension in PBS. (D) Intensity-weighted size distribution of NPs before and after purification. (E) Scanning electron microscopy image.

Figure 4-10C shows NPs pelleted after centrifugation (left) and NPs suspension in PBS (right). NPs can be stored as pellets at 4 ˚C for moderate time periods (~few days) for further studies with minimal release of DOX or degradation of polymers. The size of the NPs in 1X PBS was also determined by dynamic light scattering (DLS). Figure 4-10D shows the intensity-weighted size distribution of the particles before and after purification. The change in size distribution observed in Figure 4-10D is likely due to the fact that after further purifications of NPs via centrifugation, smaller NPs stayed in supernatant as we previously demonstrated with PLA-PEG nanoparticle formulations.[57] The polydispersity index ranged from 0.2–0.25 before purification and 0.14–0.16 after purification most likely because of the loss smaller size of NPs during centrifugation confirmed by DLS.

The charge on a particle at the shear plane is known as zeta potential. This value of surface charge is beneficial for understanding and predicting interactions between particles in suspension. The surface charge of the AF750-DOX NPs was found to be -6.9 mV± 0.7 mV. The zeta potential of NPs depends on the end groups of charged polymers such as PLL (positively charged), PEG-COOH (negatively charged), the ratio of polymers in NPs, the type of drug encapsulated and the type of surfactant (BSA, negatively charged) utilized during their preparation and purification. As can be seen on Table 4-1, there are no significant zeta potential differences between blank, AF750 labeled and DOX loaded NPs.

Table 4-1. Size / Polydispersity Index (PDI) and zeta potential of NPs.

Type of NPs	Z-average (d.nm) / PDI	Zeta Potential (mV)
Blank NPs	52.8 ± 0.3 / 0.150	-9.2 ± 0.4
DOX NPs	56.9 ± 0.3 / 0.135	-13.1 ± 2.3
AF750-DOX NPs (PLL)	63.5 ± 0.5 / 0.157	-6.9 ± 0.7
AF750-DOX NPs (PDL)	68.5 ± 0.4 / 0.189	-8.1 ± 2.6

The size of the spherical NPs is expected to allow them to easily extravasate into the leaky vasculature of tumor vessels upon intravenous administration resulting in passive accumulation into tumors. The effective optimal diameter of nanoparticles range between 100 and 200 nm is referred to favor prolonged circulation times and passive targeting of carriers thanks to the enhanced permeation and retention (EPR) effect.[41,200]

4.3.4 Loading Percentage and Entrapment Efficiency of DOX

The amount of entrapped drug in the NP formulations were determined based on the fluorescence intensity of DOX in dissolved nanoparticle solutions using fluorescence spectroscopy. The target loading of DOX based on feed ratios was 5 % (mg DOX/mg NP x 100). We achieved a 3% ± 0.4 (w/w) drug loading. The entrapment efficiency was determined as 49% ± 1.98 by analyzing supernatants from nanoparticle purification via centrifugation using fluorescence spectroscopy. The analysis was carried out in triplicate for each batch of drug-loaded NPs.

The loading studies were carried on with DOX HCl (water soluble form) as well. Unfortunately, we achieved less than 1% drug loading percentage. Since DOX HCl is highly soluble in water, the hydrophobic core of NPs could not entrap it efficiently. A small percentage of entrapped DOX HCl released very rapidly into NP suspension. For this reason, DOX HCl was converted into its insoluble free base form. We achieved high drug loading with hydrophobic DOX free base on hydrophobic core of NPs.

The loading percentage and entrapment efficiency were determined by fluorescence spectrophotometry. The absorption and emission peaks of DOX in the NPs were shifted. It should be pointed that after conversion of DOX HCl to its free base form, the visible absorption spectrum of encapsulated DOX shows slight differences from that of the DOX HCl because the deprotonation site is far from the chromophore. The presence of a distinct blue-shift of the absorption peak is a clear sign of DOX-DOX interactions due to π- π stacking.[201]

4.3.5 Enzymatic Activation of NP Fluorescence

PLL can be degraded by many intracellular proteases, such as cathepsins B and L, and trypsin.[191,202–204] AF750 molecules which are close enough, are able to transfer their energy to each other and self-quenched. This quenched signal can be recovered after proteolytic degradation of the PLL backbone. The optimal loading ratio (AF750/PLL = 2.5) that provided the appropriate quenching / dequenching effect and protease accessibility was determined from a series of polymer-dye conjugates with differing amounts of fluorescent molecules. To find the optimal loading ratio, fluorescein isothiocyanate (FITC) fluorescent dye was conjugated on PLL polymer in different molar

ratios. FITC was utilized for this preliminary experiment instead of AF750 as a result of cost considerations. FITC-labeled NPs were prepared and purified by centrifugation. Enzymatic activation studies were carried out with trypsin. Table 4-2 shows the molar ratio between FITC and PLL chains and FITC per lysine. The fluorescent development of NPs with FITC/PLL 5.14 ratio significantly increased with further centrifugation.

Table 4-2. The fluorescent development of FITC-labeled NPs with different FITC/PLL ratio and further purification.

FITC/PLL	FITC/LYS	Fluorescent Development in 3 hours	Fluorescent Development in 3 hours (with extra purification)
0.51	1/60.8	4.38-fold	N/A
1.03	1/30.4	6.51-fold	N/A
1.56	1/20.01	3.74-fold	2.44-fold
3.08	1/10.1	4.29-fold	2.89-fold
5.14	1/6.08	10.02-fold	30.01-fold
10.27	1/3.04	2.77-fold	5.42-fold
20.55	1/1.52	2.11-fold	3.07-fold

Energy can be transferred without absorption or emission of photons between two donor and acceptor chromophores. Förster resonance energy transfer (FRET) is a dynamic energy transfer (and quenching in this case) mechanism in which energy transfers while the donor is in the excited state. FRET depends strongly on the donor–acceptor distance.[205] The efficiency of FRET is inversely proportional to the sixth power of the distance between

donor and acceptor. FRET can typically occur over distances of up to 1-10 nm. Smaller distance between chromophores causes the higher FRET efficiency.[206] The structural size of the fluorophore AF750 is bigger than that of FITC. It is possible that this size difference might cause higher FRET efficiency and quenching because of lower distance between AF750 chromophores. Similarly, the extinction coefficient of AF750 is almost four times higher than that of FITC (290,000 vs. 75,000 $M^{-1}cm^{-1}$). Thus, AF750 is expected to act as a better acceptor than FITC. Thus, considering molecular weight, structure, excitation/emission wavelengths, molar absorption, quantum yield as well as the cost of AF750, an AF750/PLL ratio of 2.5 was selected for enzymatic activation study. Figure 4-11 proves the use of smaller ratio of AF750/PLL than that of FITC/PLL showed higher fluorescent development.

Trypsin was used as a model protease for activation of the fluorescence of NPs. As shown in Figure 4-11, the fluorescence intensity of NP suspensions immediately increased 2.6-fold and reached 32.7-fold within 240 min of exposure to trypsin *in vitro*, while only a slight increase (2.9-fold) in fluorescence was observed in the same period in the presence of the protease and its inhibitor *Nα*-tosyl-L-lysine chloromethyl ketone (TLCK). As expected, there is no increase in the absence of trypsin. The off-on switch fluorescent enhancement demonstrates the capabilities of our NPs as enzymatically triggered contrast agents by tumor-overexpressed enzymes.

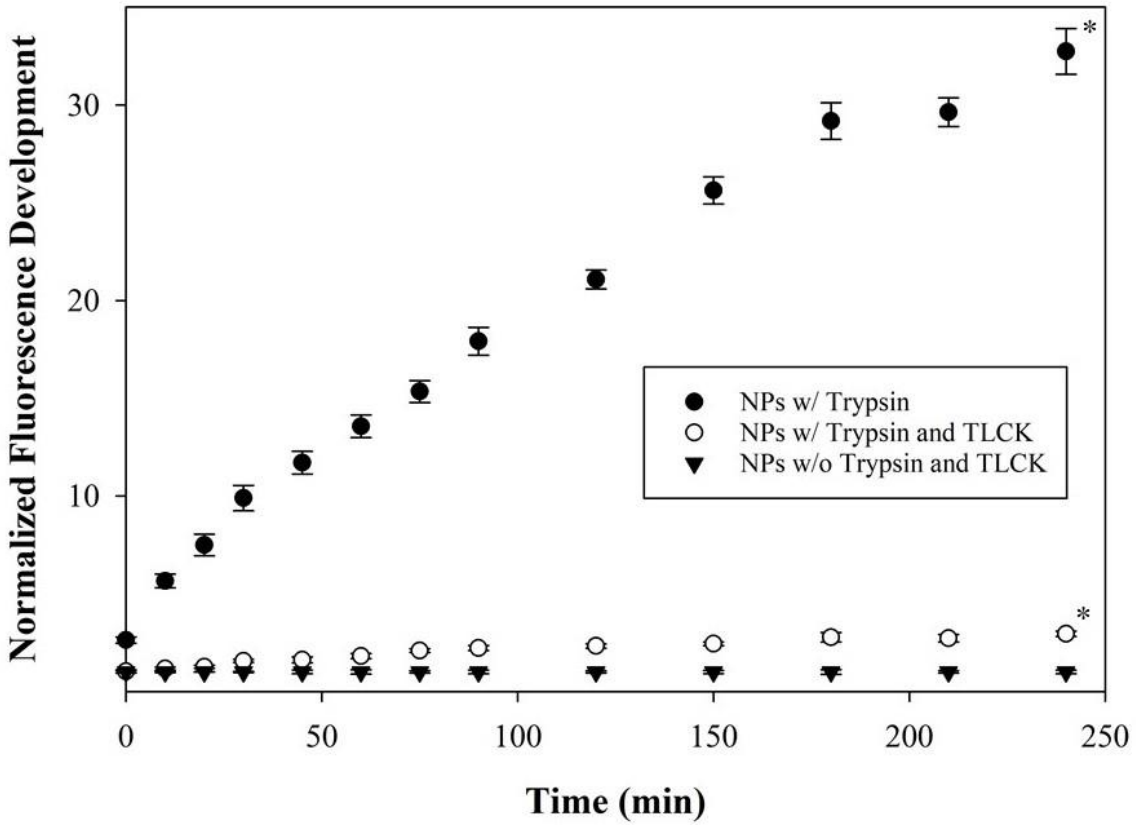

Figure 4-11. *In vitro* enzymatic activation of NP fluorescence prepared with PLGA-PLL. Plot of average fluorescence at 780 nm versus time for NPs exposed to trypsin, trypsin and TLCK, or buffer. The final concentration of trypsin was 6.25 mg/mL, and of TLCK was 10 mg/mL. Error bars represent standard deviation between replicates (n = 4). Statistically significant difference compared to positive control ($p < 0.05$) is identified with an asterisk (*) at 240 min.

For comparison, AF750-labeled non-cleavable poly-D-lysine (PDL) NPs at the same ratio were treated with trypsin in the same way. As expected, the fluorescence signal was not increased (Figure 4-12) significantly (2.2-fold vs. < 30-fold), suggesting that proteolysis is required to release the quenched fluorescence signal.

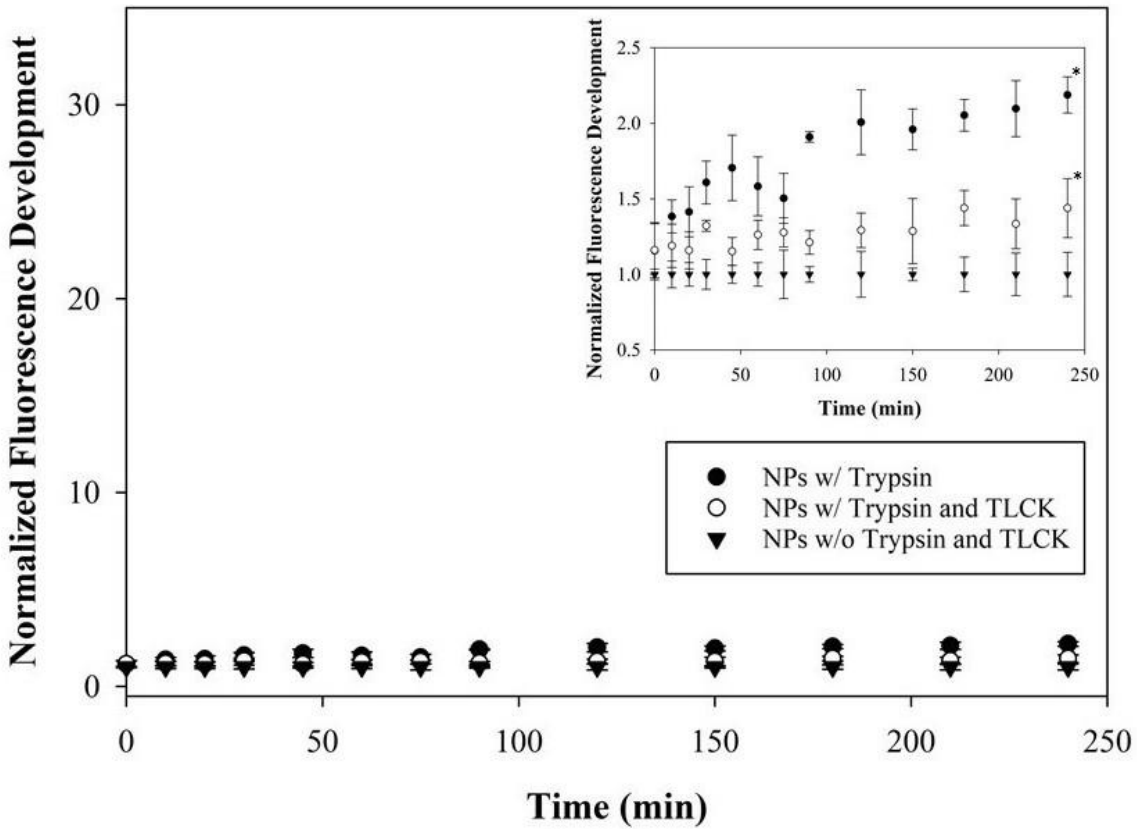

Figure 4-12. *In vitro* enzymatic activation of NP fluorescence prepared with PLGA-PDL. Plot of average fluorescence at 780 nm versus time for NPs exposed to trypsin, trypsin and TLCK, or buffer. The final concentration of trypsin was 6.25 mg/mL, and of TLCK was 10 mg/mL. The y-axis was scaled up to 35-fold to compare with Figure 4-11. Error bars represent standard deviation between replicates (n = 4). The inset graph shows same data of the graph with y-axis scaled down to 2.4 to show details. Statistically significant difference compared to positive control ($p < 0.05$) is identified with an asterisk (*) at 240 min.

4.3.6 *In Vitro* Drug Release Study

DOX HCl is water soluble form of the drug. It was used as control study for understanding the rate of diffusion of DOX solutions through the dialysis membrane into the dialysate. The *in vitro* release of DOX from DOX-NPs and DOX HCl at pH 7.4 in 24 hours is shown in Figure 4-13. Fast diffusion of DOX HCl across the dialysis membrane was observed, as expected, releasing 99.3% ± 0.16 of drug in the first 18 hours. The

cumulative percentage of doxorubicin free base released from NPs at pH 7.4 was 20.63% ± 5.03 within 24 hours.

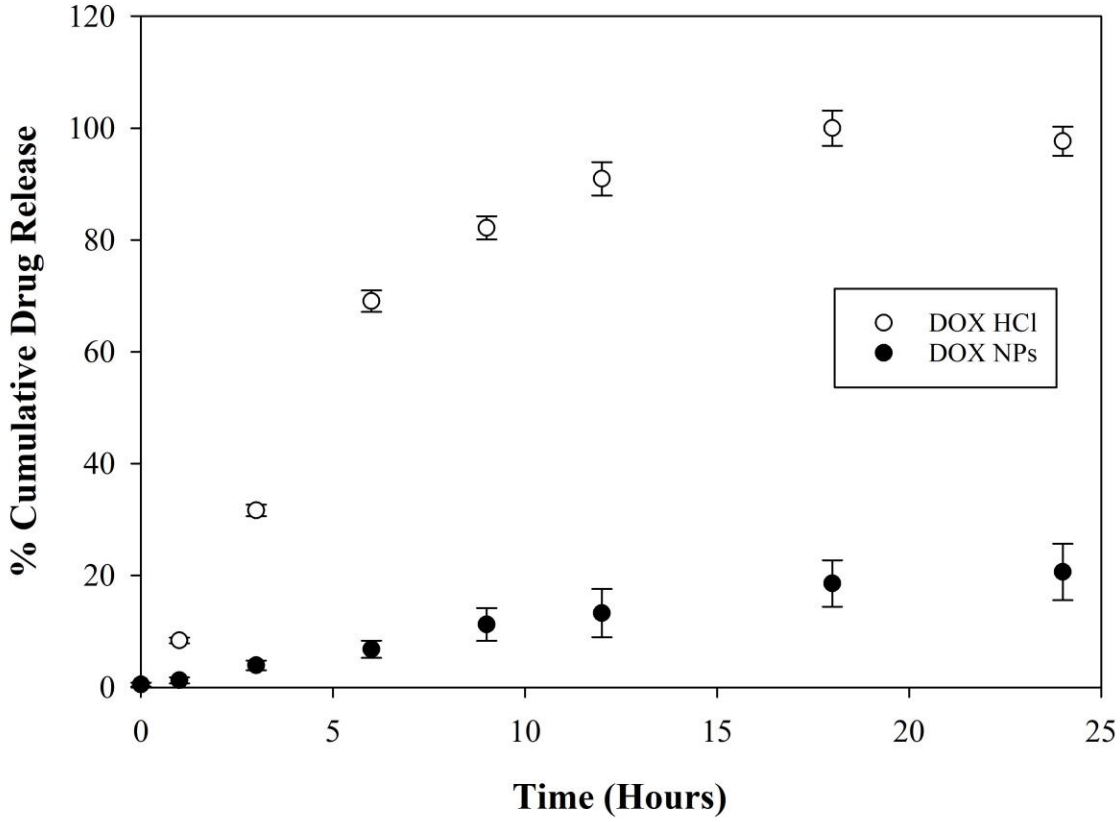

Figure 4-13. Doxorubicin release profiles in PBS, pH 7.4 in 24 hours at 37 ˚C for DOX NPs and DOX HCl (control). Error bars represent standard deviation between replicates (n = 4).

The drug release study was continued for DOX NPs for 30 days. The cumulative percentage of doxorubicin released from NPs at pH 7.4 was 61% ± 13 within 30 days (Figure 4-14).

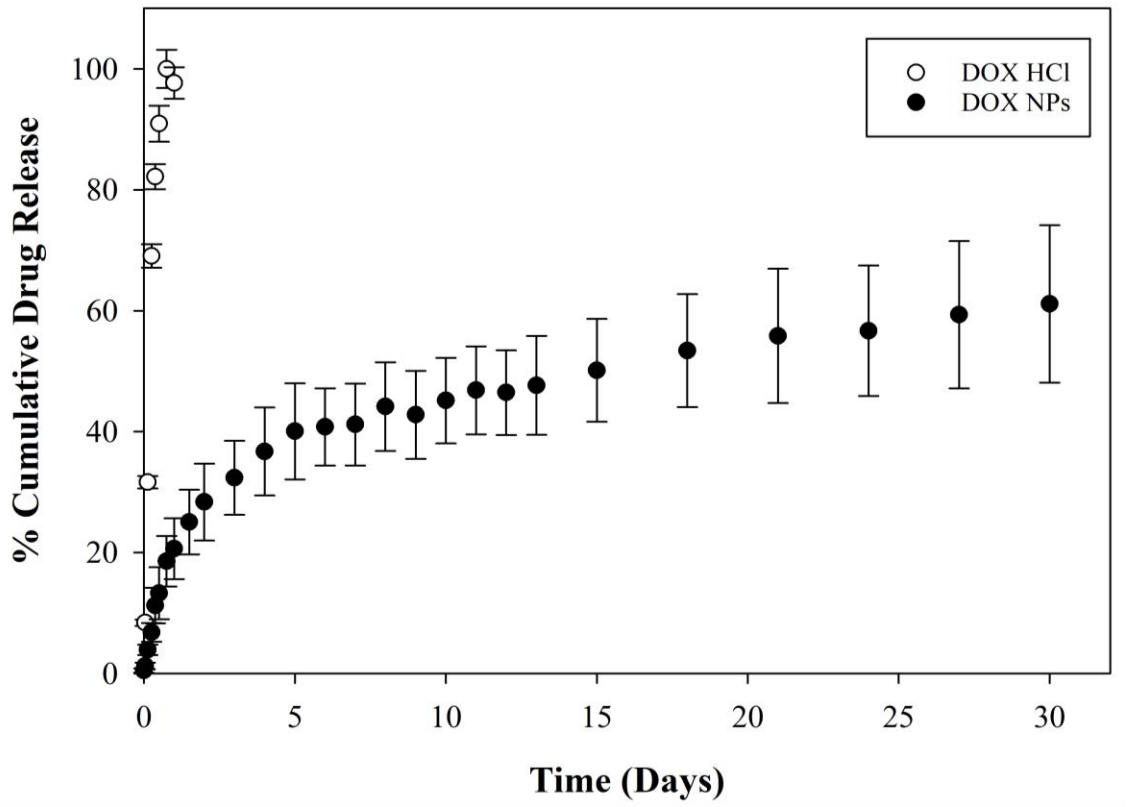

Figure 4-14. Doxorubicin release profiles in PBS, pH 7.4 in 30 days at 37 ˚C for DOX NPs and DOX HCl (control). Error bars represent standard deviation between replicates (n = 4).

To analyze the *in vitro* drug release data, the power-law expression was used to describe the release kinetics. The controlled release behavior of spherical, non-swelling polymeric delivery systems can be analyzed with equation 3. This equation was used to analyze the first 60 % of the drug release out of the total released,

$$\frac{M_t}{M_\infty} = kt^n \qquad (3)$$

where M_t/M_∞ is the fractional of drug release, k is a constant, t is the release time, and n is the diffusional exponent that provides information about the mechanism associated with the drug release from the particles. For spherical particles, $n < 0.43$ represents quasi-Fickian diffusion, $n = 0.43$ represents purely Fickian diffusion, $0.43 < n < 0.85$ represents

anomalous (non-Fickian) transport, n = 0.85 represents Case-II transport, and n = 1 represents zero order release.[207–209] The diffusion constant "n" for our drug release process was determined as 0.5, as shown in Figure 4-15.

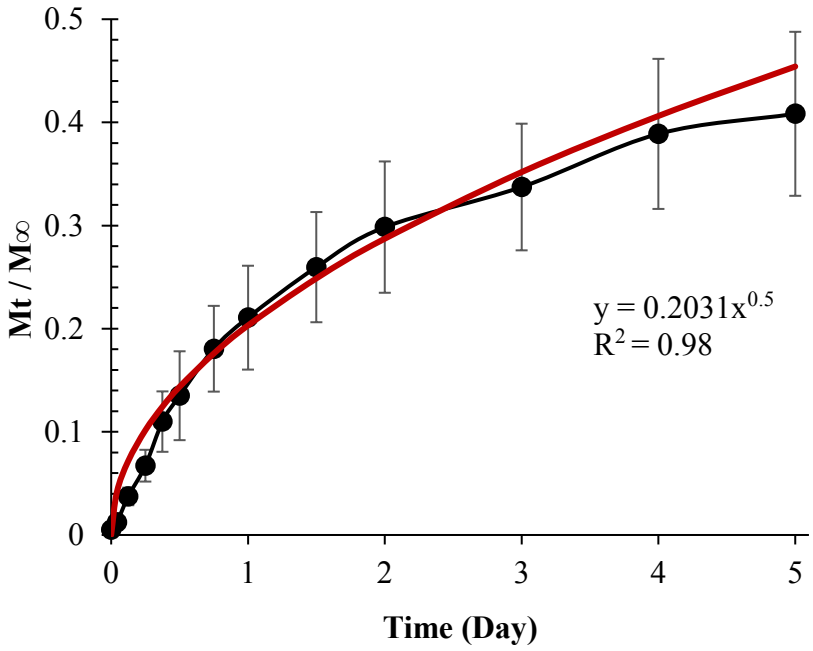

Figure 4-15. Fitting of doxorubicin-free base release data to power law equation for $M_t/M_\infty < 0.5$ (first five days of the release). Here each data point (black) represents the average fractional release for four independent replicates while the error bars represent the standard deviation between samples. The power trend line (red) and associated equation provide the value of n = 0.5, indicating Fickian drug transport ($R^2 = 0.98$).

The diffusional constant value indicates that doxorubicin-free base was released from the particles through anomalous transport, i.e. a process likely influenced by drug dissolution, drug diffusion, and polymer relaxation. About 40% of the drug was released within 5 days, and total cumulative release within 30 days was found to be nearly 62%. Low aqueous solubility of doxorubicin-free base may be a reason for the slow release from the polymer matrices after burst release.

To investigate the release mechanism for the latter part of the release study (past 5 days), the data were again fitted to a power-law equation, as shown in Figure 4-16. The exponent was found to be 0.2617. Therefore, the release dynamic of DOX obeyed quasi-Fickian diffusion after 5 days. Delaying drug release after five days might be caused by crystallization of DOX FB within the polymer matrix.

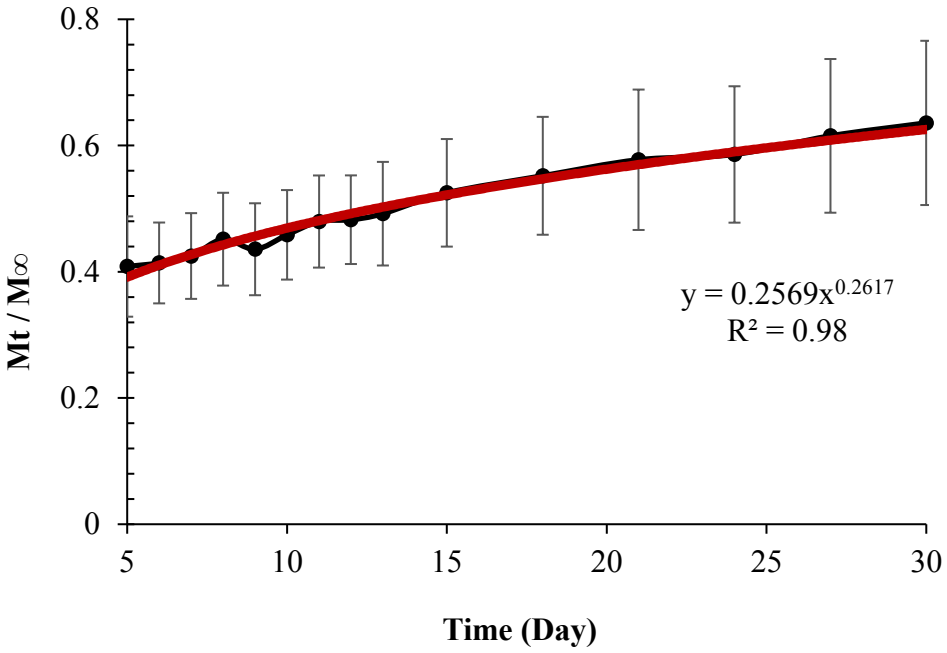

Figure 4-16. Fractional of drug release vs. time for DOX NPs after five days (black) and power law fit (red).

Missirlis *et al.* prepared DOX free base-loaded NPs composed of PEG and poloxamer 407 by inverse emulsion photopolymerization. They converted DOX HCl to its free base form and used it for encapsulation. The burst release was recorded at 37 ˚C, pH 7.4 and accounted for approximately 10% of encapsulated DOX. At 37 ˚C, they found that "k" was 5.14 ±0.07 and "n" was 0.47 ±0.03 which indicates the Fickian diffusion. The DOX free base release from NPs at 37 ˚C was found approximately 50% in 168 hours (a week).[210]

Kataoka et al. prepared DOX free base-loaded micelles composed of poly(ethylene glycol)–poly(β-benzyl-L-aspartate) block copolymer by an oil/water emulsion method. At pH 7.4, biphasic release profiles of DOX was seen. The release profile was characterized by a rapid release in the initial stage (phase I, first 10 hours). Then, slow and sustained release occurred which seems to continue for a prolonged period of time (phase II, up to 80 hours). The cumulative DOX free base release at pH 7.4 was recorded as about 25% in three days.[211]

The drug release kinetic studies of Missirlis and Kataoka's support the data that was obtained in this study. The DOX free base released 25% in three days,[211] 50% in a week,[210] and 62% in a month in this study. The hydrophobic form of DOX releases from nanoparticles slow overtime.

4.3.7 Determination of NP Cytocompatibility

The cytocompatibility of the blank NPs (no DOX, no AF750) was determined with MDA-MB-231 cancer cells. Figure 4-17 shows the viability of cells exposed to blank NPs for 72 hours as determined by the MTT assay. Cells exposed to NPs showed high viability, even at high concentrations. In addition to quantitative viability determination via the MTT assay, cells were monitored via microscopy during the studies and no visual differences in cell morphology or growth were observed between NP-treated cells compared to cells in the positive viability control set. These studies overall suggest that the blank NPs are biocompatible.

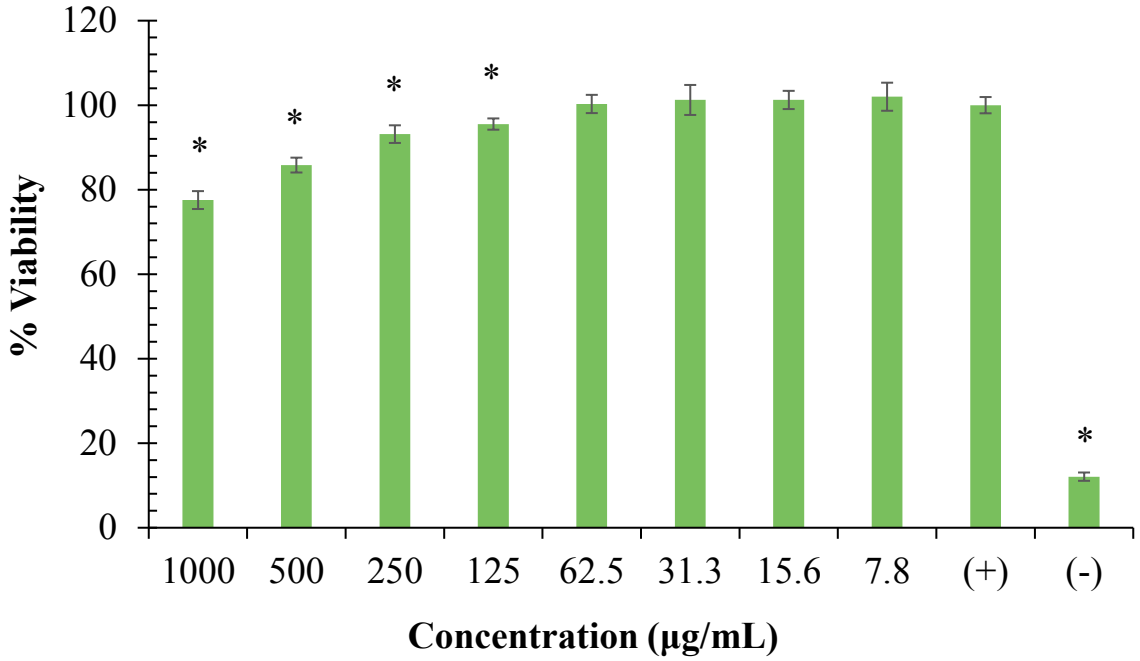

Figure 4-17. Viability of MDA-MB-231 cells after exposure to Blank NP for 72 hours as determined with MTT assay. Cells cultured in complete media without NPs represent the positive control (+). Cells killed with methanol prior to MTT assay represent negative control (-). Bars represent standard deviation between replicates (n=6). Statistically significant difference compared to positive control ($p < 0.05$) is identified with an asterisk (*).

The cytocompatibility of the blank NPs was also investigated with the CellTiter-Glo® luminescence assay. Figure 4-18 shows the viability of cells exposed to blank NPs for 72 hours. For this study, the wider range of concentrations of NPs were used to match that used in later therapeutic effect studies. The viability was almost same as the highest concentration (1 mg/mL) of NPs utilizing the MTT assay with at the highest concentration (2 mg/mL) of NPs analyzed with the luminescence assay. Blank NPs at very high concentrations (1 or 2 mg/mL) are not toxic to the cells. The luminescence and MTT assays showed very similar results especially at low concentrations.

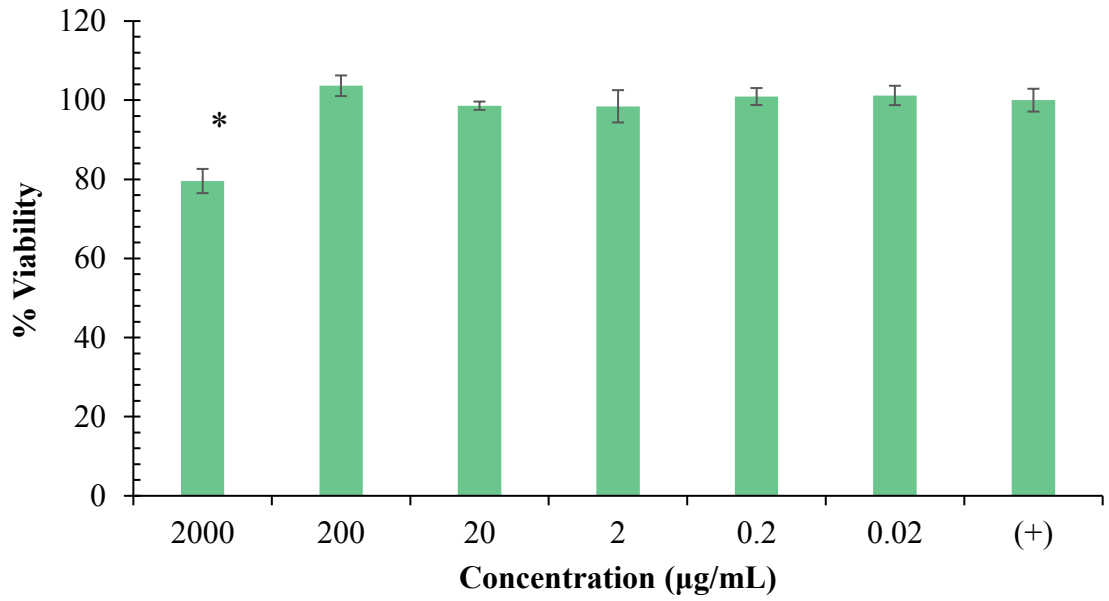

Figure 4-18. Viability of MDA-MB-231 cells after exposure to Blank NP 72 hours determined with CellTiter-Glo® luminescence assay. Cells cultured in complete media without NPs represent the positive control (+). Wells with media without serum represent negative control (-). Bars represent standard deviation between replicates (n=6). Statistically significant difference compared to positive control ($p < 0.05$) was identified with an asterisk (*).

4.3.8 Determination of NP Therapeutic Efficacy

The *in vitro* therapeutic efficacy of DOX-loaded NPs (no AF750) was evaluated with the CellTiter-Glo® luminescence assay in MDA-MB-231 breast cancer cells. Figure 4-19 shows the viability of cells exposed to DOX free base, DOX HCl and DOX NPs at the same drug concentrations. Lower cell viability represents a higher anti-tumor therapeutic effect. The viability of cells treated with DOX free base solution (not nanoparticles) at 100 µM concentration appears higher than that of cells exposed to lower DOX free base concentrations, and that of cells treated with DOX HCl and DOX NPs. However, this is an artifact of the study that is caused by the fact that at high concentrations DOX free base solution precipitates and strains the well plate (Figure 4-20), causing optical

interference, light scattering, and background emission which leads to erroneous readings. This is in fact the reason why the luminescent assay was utilized as the effect was much more pronounced with the colorimetric MTT assay. Overall, however, cells treated with DOX NPs showed higher viability than cells exposed to DOX HCl or DOX free base solutions. This was confirmed through visual observation of the samples. The reason for this is most likely the fact that doxorubicin released slowly in to cells from NPs, thereby exposing the cells to much lower effective concentrations than the controls within the 72-hour exposure time.

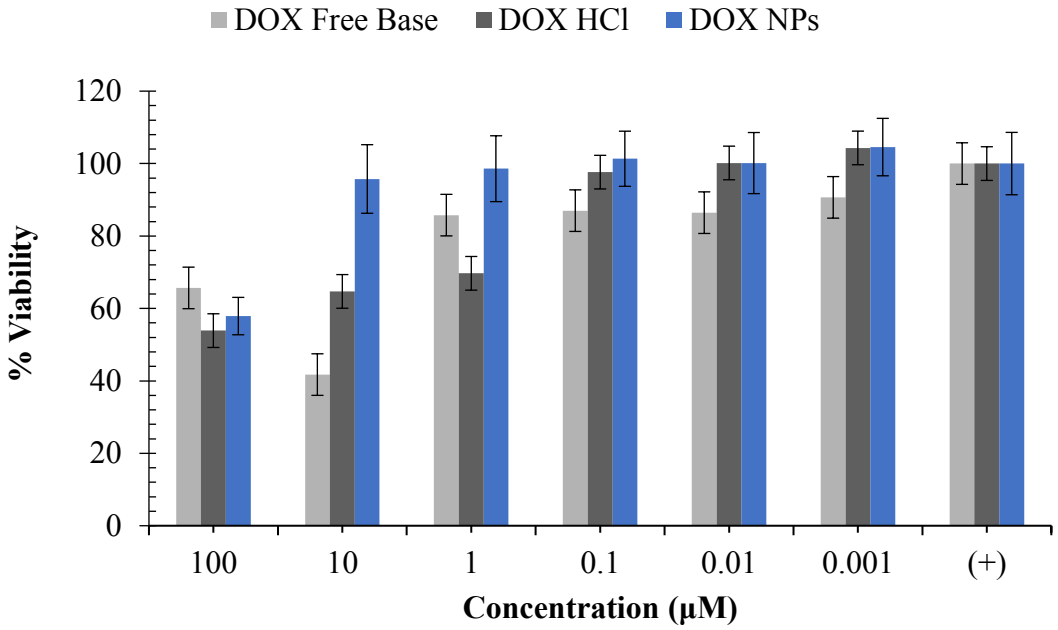

mg/mL, 2000	200	20	2	0.2	0.02	(+)

Figure 4-19. Viability of MDA-MB-231 cells after exposure to DOX Free Base (FB), DOX HCl, and DOX NPs for 72 hours as determined with CellTiter-Glo® luminescence assay. Cells cultured in complete media without NPs represent the positive control (+) for DOX HCl and DOX NPs study. Cells cultured in complete media without NPs with 1% DMSO represent the positive control (+) for DOX FB study. Bars represent standard deviation. Box on bottom of figure shows the actual equivalent concentrations of NPs matching the DOX FB concentrations.

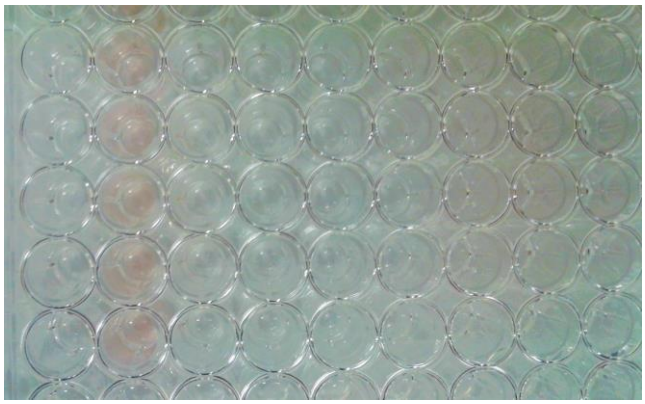

Figure 4-20. Appearance of 96-well plate after cells incubated with DOX free base for 72 hours and washed with DPBS.

Since most of the therapeutic effect was seen with drug concentrations between 10 – 100 µM with DOX NPs, additional studies were conducted with drug concentrations in this range. Figure 4-21 shows the viability of cells exposed to DOX NPs for 72 hours. Lower cell viability represents a higher anti-tumor therapeutic effect. As shown, most of the effect of DOX NPs is observed with doxorubicin in the concentration range of 10 – 40 µM. Above this concentration, no further cell death is observed.

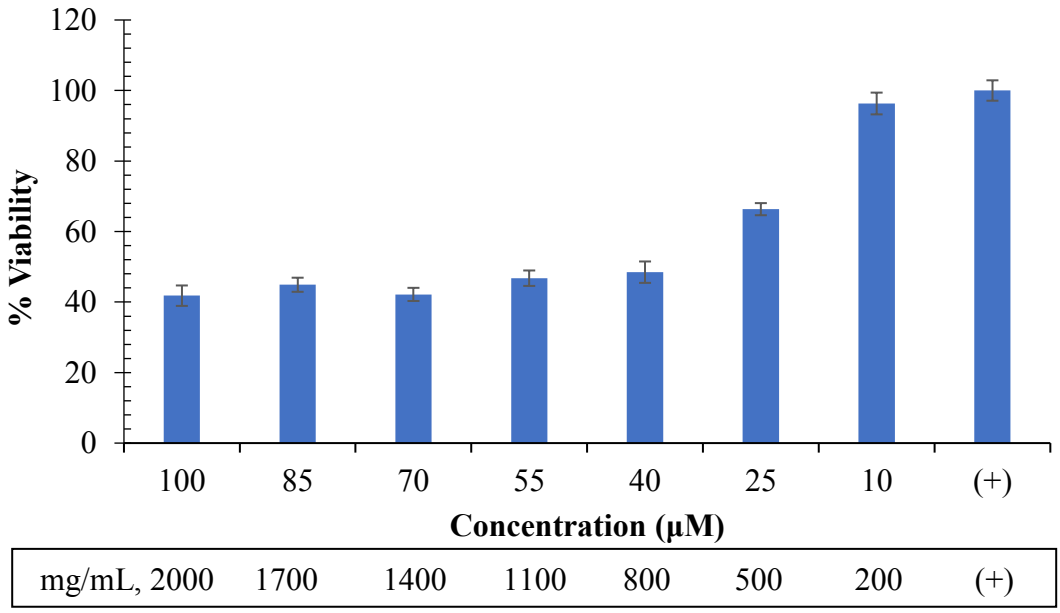

Figure 4-21. Viability of MDA-MB-231 cells after exposure to DOX NPs for 72 hours as determined with CellTiter-Glo® luminescence assay. Cells cultured in complete media without NPs represent the positive control (+). Bars represent standard deviation. Box on bottom of figure shows the equivalent concentrations of NP with DOX FB.

Moffatt *et al.* conducted therapeutic efficacy studies with DOX HCl concentration in range 0.005-50 μg/mL using the MDA-MB-231 cell line. They synthesized DOX-PLGA-PEG-RGD nanoparticles for integrin targeted drug delivery. The most of therapeutic effect of nanoparticles was observed with doxorubicin in the concentration range of 0.1-10 μg/mL (0.18-18 μM).[212]

Betancourt *et al.* prepared DOX HCl-loaded PLGA nanoparticles and evaluated their interaction with MDA-MB-231 breast cancer cells. They used 1.0, 10.0, 50.0 or 100.0 μg/ml of DOX for a 5.0% drug loading in the NPs to evaluate therapeutic efficacy of NPs. DOX-loaded NPs showed the therapeutic effect at concentrations equivalent to or higher than 1 μg/ml of DOX (1.8 μM).[128]

Siddharth et al. prepared chitosan-dextran sulfate coated DOX(HCl)-loaded PLGA-PVA nanoparticles. They treated MDA-MB-231 breast cancer cells with the NPs at various concentrations. NPs showed the most therapeutic effect at concentrations equivalent to and higher than 50 nM (0.05-0.5 μM) of DOX.[213]

Breast cancer cells, especially MDA-MB-231 and MCF-7, develop DOX resistance and cause low therapeutic efficacy of DOX. The use of DOX free base (insoluble in water) in NPs results in lower therapeutic effect that that of DOX HCl loaded NPs due to the slow release rate from the nanoparticles. Although DOX free base-loaded NPs were used in this study, the most therapeutic effect results at concentrations are very similar with the study carried by Betancourt[128] *et al*.

4.3.9 Microscopic Study of NP Interaction with Cells

Fluorescence microscopy was used to investigate the ability of the NPs to mediate NIR fluorescence and DOX delivery to MDA-MB-231 cells. As shown in Figure 4-22, an increase in AF750 fluorescence intensity was observed throughout the four-day study, suggesting that the fluorescence was in fact being activated by the cells. The highest fluorescence intensity of AF750 was observed on the third day. On the other hand, the fluorescence intensity of DOX did not change significantly over time. These results suggest that the nanoparticles were already internalized in the cells by day 1, and that the NIR fluorescence of AF750 was "developed" by cell proteases. A decreased cell density was observed over time due to therapeutic efficacy of DOX, which caused dying cells to detach from the plate.

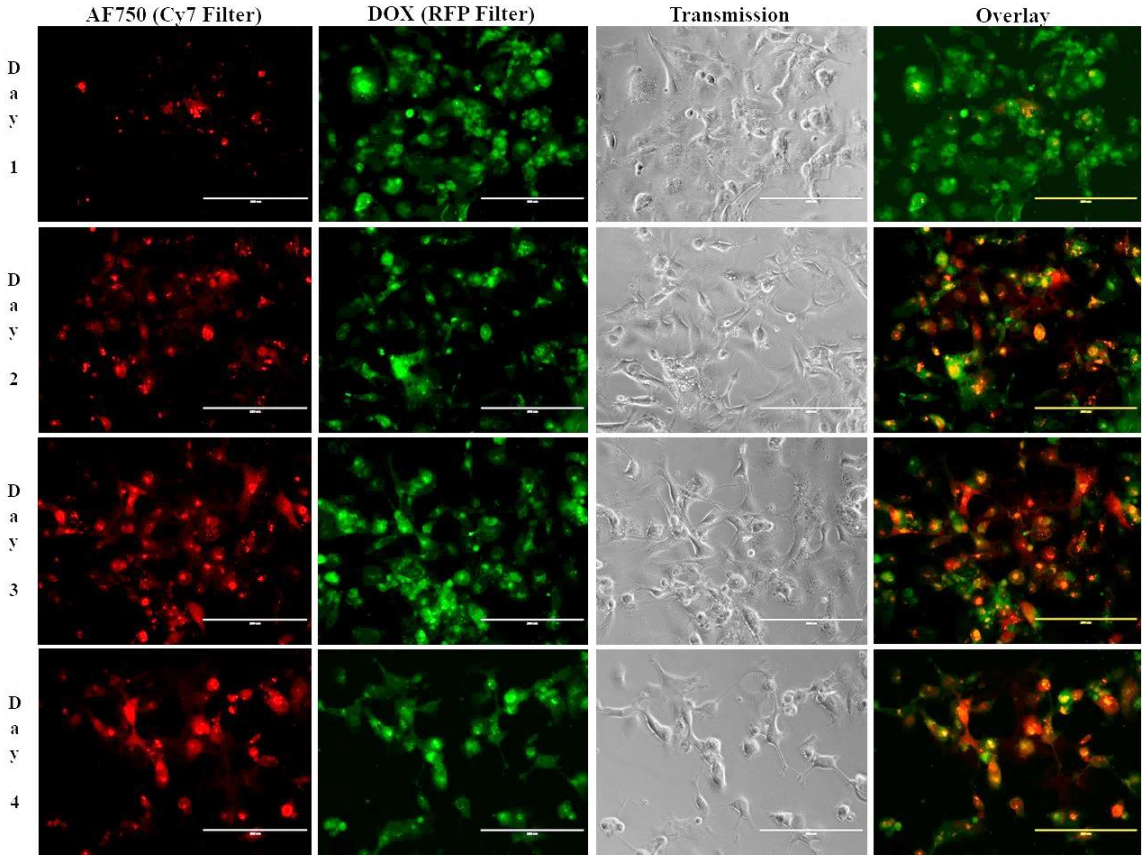

Figure 4-22. Enzymatic activation of fluorescence and DOX release in cells over 96 hours. Individual channel and overlay images of MDA-MB-231 cells exposed to AF750-labeled DOX-loaded NPs with PLGA-PLL copolymer at 0.2 μg/mL (10 μM DOX). Red color indicates AF750 and green color indicates DOX FB. Scale bar represents 200 μm.

To confirm that NIR fluorescence development was in fact caused by cell activation of AF750 fluorescence and not simply a result of differences in AF750 and DOX diffusion into the cells, studies were then conducted with NPs prepared with non-cleavable PLGA-PDL. As shown in Figure 4-23, NPs containing inert PDL polypeptide showed very low and constant AF750 fluorescence during the four-day study. These data agree with the enzymatic activation study of PDL-NPs, in which we observed very low fluorescence development (about 2-fold). This low fluorescence of AF750 might come from PLL impurity in the purchased PDL polymer product, although we have not further studied this possibility. As in the study with PLGA-PLL nanoparticles, steady fluorescence intensity of DOX was observed over time and the cell density decreased during the study.

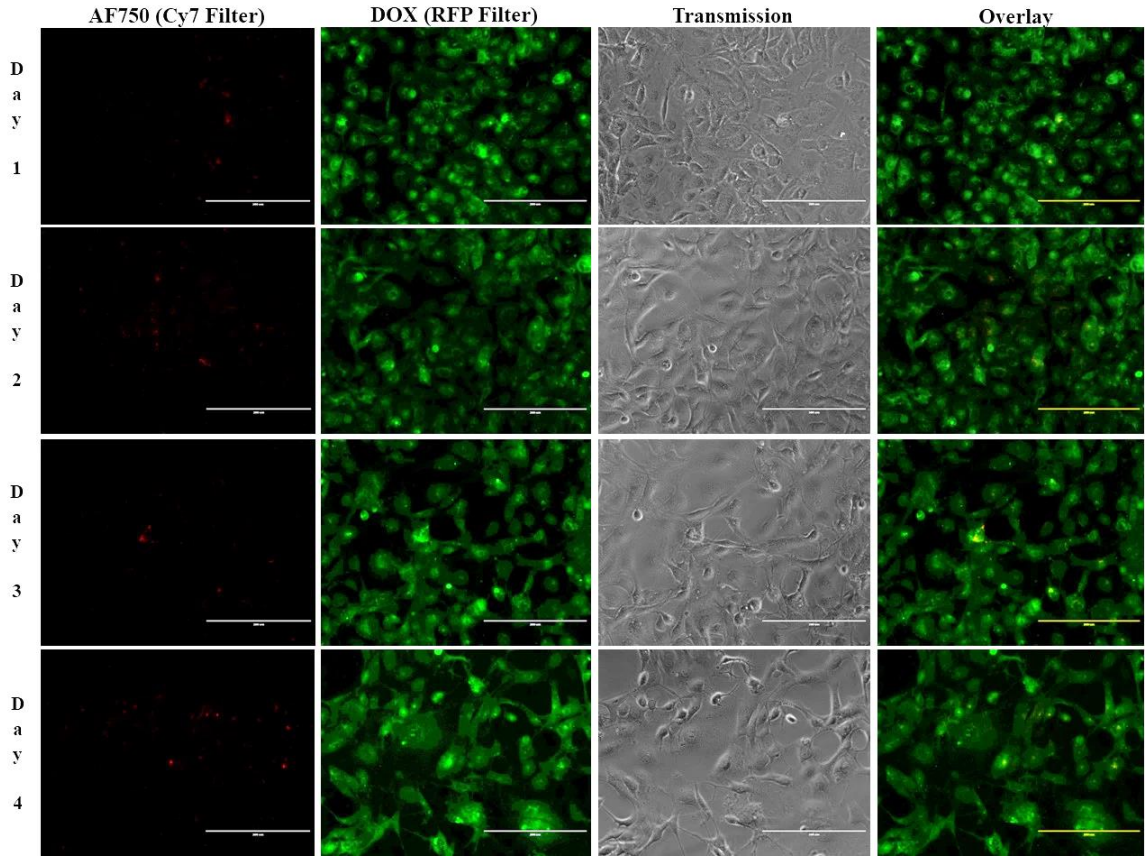

Figure 4-23. Enzymatic activation of fluorescence and DOX release in cells over 96 hours. Individual channel and overlay images of MDA-MB-231 cells exposed to AF750-labeled DOX-loaded NPs with PLGA-PDL copolymer at 0.2 μg/mL (10 μM DOX). Red color indicates AF750 and green color indicates DOX FB. Scale bar represents 200 μm.

4.4 Discussion

Amphiphilic block copolymers PLGA-PLL and PLA-PEGs were synthesized and characterized. The conjugation of AF750 on PLL (or PDL) chains was successful. AF750-labeled DOX-loaded NPs were successfully prepared in very acceptable size, shape, and low polydispersity. Approximately 3% DOX was encapsulated in the core of the NPs. The cumulative drug release in 30 days at pH 7.4 at 37 ˚C was about 62% with biphasic release profiles. The first five days of drug release was controlled by anomalous transport, and later by quasi-Fickian diffusion for up to 30 days.

Every amino acid (except glycine) has two isomeric forms, L- and D-. These two different enantiomers form around the central carbon atom. Only L-amino acids are produced in cells and incorporated into proteins.[214] D-isomers of amino acids are of biologically inert nature. For example, poly-D-lysine (PDL) served to eliminate macrophage receptor recognition of NPs. [215] As a control study of enzymatic activation of NPs, AF750 was also conjugated to the non-enzymatically cleavable PDL at the same ratio (AF750/PDL = 2.5) and prepared NPs. While the enzymatic activation fluorescence of NPs that contained enzymatically cleavable PLL increased up to about 33-fold in 4 hours, that of with PDL increased only ~ 3-fold with exposure to trypsin *in vitro.*

The AF750 was conjugated to PLL after NP preparation in Chapter III. The AF750 labelling method on PLL was modified in this Chapter. As described in 4.2.6 section, AF750 was conjugated with PLGA-PLL copolymer, purified by centrifugation to remove unlabeled AF750 molecules from the copolymer, then mixed into with the other polymers/solvents to prepare the organic phase of NPs. Nanoprecipitation occurred in bovine serum albumin (BSA) solution. BSA was used as surfactant and stabilizer for NPs preparation. BSA is a serum protein that consists of 60 lysine that can react with AF750-NHS for the coupling of peptides.[216] The modified NP labeling method prevents AF750 from binding to BSA, thereby it provides better control for enzymatic activation study.

Luminescent cell viability assay is a method to determine the number of viable cells in culture based on quantitation of the ATP present, which signals the presence of metabolically active cells by the enzyme catalyzed (luciferase) bioluminescence reaction.[217] Luminescent cell viability assay was used in addition to MTT assay for determining of NP cytocompatibility. The luminescence assay was especially utilized for

determination of therapeutic efficacy. The absorbance of MTT reagent (λ_{Abs} = 590 nm) and DOX (λ_{Abs} = 600 nm) in NPs interfere with each other due to their similar wavelengths. Luminescence assay minimizes this interference because this assay is based on luminescence and not absorbance. The cytocompatibility of blank NPs and therapeutic efficacy of DOX-loaded NPs were determined by luminescence assay. High viability was observed in cells exposed to blank NPs, even at very high concentrations. These data confirm that blank NPs (in the absence of DOX and AF750) are biocompatible. DOX-loaded NPs, on the other hand, showed dose-dependent decreases in cell viability, as expected, especially in the range of 10 – 40 μM. At higher DOX concentration with the DOX NPs, no further cell death was observed which could be associated with drug resistance, or might be an artifact of the luminescence assay utilized. For example, cells treated with methanol, which we typically utilize as a "dead" control in MTT assays, presented luminescence levels higher than those of the DOX NP-treated cells in several independent studies. This might be caused by the design of this assay, which is based on the quantitation of ATP of live cells by the enzyme (luciferase) catalyzed bioluminescence reaction of luciferin to oxyluciferin.[217] Ultimately, the potential of these nanoparticles to enhance the therapeutic effect of the drug should be evaluated *in vivo,* here nanoencapsulation is expected to provide improved tumor accumulation and long-term release would be beneficial.

The NP and cell interaction study showed an increase in NIR AF750 fluorescence intensity overtime that was associated with enzymatic activation of the PLL-AF750 conjugates, as confirmed with non-cleavable PDL controls. A significant change was not observed on DOX fluorescence intensity because of its slow release kinetics.

Multifunctional theranostic NPs allowed image of cancer cells by near infrared imaging, and at the same time delivery of anticancer drug that in turn were released from the NPs to exhibit anticancer activity. We anticipate that theranostic NPs may be utilized in a distinct way to develop combined diagnosis and therapy for cancer treatment.

V. CONCLUSIONS AND FUTURE OUTLOOK

Early detection of breast cancer and determination of the most suitable treatment for the patient are the most important strategies to prevent deaths from breast cancer. Early detected breast cancer, when it has not spread past the primary tumor location, is easier to treat successfully. Novel nano-sized drug delivery and imaging systems improve the pharmacological behavior of chemotherapeutic drugs thereby reducing side effects, enable the visualization of the target, and provide the ability to evaluate and adjust treatment protocols over time. Theranostic systems are the most recently developed nanomedicines and have high future potential in being the primary tool for personalized medicine. These nanomedicines provide sites for high capacities of therapeutic agent loading and for targeting agents, as well as loading or attaching imaging agents.

In this work, biodegradable polymeric nanoparticles (NPs) were developed and evaluated for imaging and treatment of breast cancer. These nanoparticles have a core-shell architecture. The core of the nanoparticles is made of biodegradable and biocompatible polyesters, poly(lactic-*co*-glycolic acid) and poly(lactic acid). The hydrophobic core is a suitable compartment for carrying the chemotherapeutic drug doxorubicin for drug delivery. The hydrophilic shell contains poly(ethylene glycol) and protease cleavable polypeptide poly-L-lysine. Poly-L-lysine is decorated with near infrared fluorescent dye molecules (Alexa Fluor 750, AF750) for optical imaging of breast cancer cells. Amphiphilic copolymers were synthesized by ring opening polymerization and carbodiimide conjugation reactions. The blend of polymer solutions was combined with doxorubicin and NPs were successfully prepared by the nanoprecipitation method. The size of the spherical NPs was in the range of 60 nm.

The encapsulation of doxorubicin on the core of NPs was efficient and reproducible via nanoprecipitation. During *in vitro* imaging studies, a decreased number of cells were observed over time due to doxorubicin release. The slow release kinetic of hydrophobic doxorubicin free base may give an advantage for *in vivo* studies. If NPs are targeted to specific types of cells, they will have enough time to reach the targeted site and release drug into cells with minimal nonspecific release in the circulation.

The imaging agent AF750 was labeled on protease cleavable poly-L-lysine. Non-active AF750 fluorophores were activated when NPs were introduced to cancer cells. High amount of proteases including trypsin and cathepsins on MDA-MB-231 breast cancer cells cleaved the poly-L-lysine to its fragments with AF750 molecules. The self-quenched AF750 molecules thereby separated and were able to emit absorbed light energy as fluorescence radiation. Increased fluorescence intensity was observed over time in *in vitro* studies. The inactive form of poly(lysine) (D- enantiomer) was used as a control for enzymatic development fluorescence studies. NPs contained AF750-labeled poly-D-lysine did not show fluorescent development compared with AF750-PLL nanoparticles. These results show that the optical imaging of cancer cells using NPs occurs due to protease mediated activation.

Trypsin activates and is also co-expressed with matrix metalloproteases (MMPs) such as MMP-9 that plays an important role in cell proliferation, invasion and metastasis.[196] Serine protease inhibitors such as trypsin and tryptase inhibitors have been used as therapeutics for the treatment of diseases.[194] The targeting of serine proteases has been studied to prevent tumor metastasis over the last ten years.[194] Elevated levels of MMP-9 (gelatinase B) is related to tumor progression and metastasis in several solid tumor types

including breast cancer.[218–221] In this work, PLL was used as a model enzymatically cleavable polypeptide. After optimizing the method with PLL, custom polypeptides, such as Pro-Leu-Gly~Leu-Ala-Arg-Lys $(PLGLARK)_n$ or Pro-Leu-Gly~Val-Arg-Gly-Lys $(PLGVRGK)_n$, which are substrates for breast cancer overexpressed MMP-9 can be used to provide further tumor specificity for future imaging studies.[222]

The viability of cells exposed to NPs were determined by luminescence and MTT assays. Blank NPs that lacked DOX showed high viability at very high NP concentrations. Thereby, NPs are highly suitable for using as an imaging agents and drug delivery systems. DOX loaded NPs showed cytotoxicity in the range of 10 - 40 μM DOX concentration. These studies suggested that the NPs caused reduction of cell viability due to the presence of doxorubicin. When the drug (DOX free base, and DOX HCl forms) was administered directly to the cells without a carrier, the viability of cells decreased as expected. These results were encouraging because *in vivo* there would be enough time for DOX-loaded NPs to reach the tumor and release drug without releasing during blood circulation.

HER2 is a receptor that plays an important role in the proliferation and invasion of aggressive types of breast cancer. The overexpression of HER2 is found in approximately 25-30% of breast cancers.[223] HER2-positive breast cancers tend to be more aggressive, more malignant, and lead to higher recurrence than other types of breast cancer.[224] While HER2-negative patients had a five-year survival rate of 93.7%, HER2-positive patients had a 77.1% five-year survival rate.[5] More than half of the HER2-positive patients are estrogen receptor/progesterone receptor (ER/PR)-negative.[225] Therefore, endocrine therapies are not suitable for HER2-positive breast cancers.[225,226] As a result, the development of targeted therapies for HER2-positive breast cancer is really needed. Trastuzumab (Herceptin), a

humanized HER2 monoclonal antibody, has been approved as targeted treatment of HER2-positive metastatic breast cancer. However, Herceptin resistance is developed rapidly with this treatment in nearly all patients.[225,227,228] Thus, it is necessary to develop novel targeting therapeutic strategies for treatment of HER2-positive breast cancer.

The design of NPs herein presented was built on this targeted therapy strategy. One of the copolymers that was synthesized, PLA-PEG-COOH, would be used a site for anti-HER2 targeting agent attachment to enable treatment of HER2-positive breast cancer. This anti-HER2 targeting agent could be an aptamer, antibody, peptide, or affibody. Aptamers are small single-stranded DNA or RNA oligonucleotides that demonstrate excellent specificity and high affinity toward their target proteins.[229] Furthermore, aptamers have several advantages including low molecular weight, low toxicity, high stability, easy and reproducible synthesis, lack of immunogenicity, and rapid tissue penetration.[230] The easy functionalization of aptamers makes it possible to design various aptamer conjugates to develop more efficient molecular probes for sensing, imaging, and targeted therapy. Macugen, the first RNA aptamer drug, was approved by FDA for the treatment of all types of neovascular age-related macular degeneration in 2004.[231] There are some published studies on anti-HER2 DNA and RNA aptamers as a tumor targeting ligand for delivering chemotherapeutic drugs in the literature.[225,232–234] Understanding the interaction of NPs with the cell membrane is crucial to investigate to use of NPs for efficient intracellular therapeutic drug delivery. The specificity of cell binding and cellular uptake of targeting agent-modified NPs by HER2-positive SKBR3 and HER2-negative MDA-MB-231 cells could be therefore studied in future work.

Before *in vivo* studies of NPs are conducted, the stability of the NPs should be investigated in water, and phosphate-buffered saline (PBS) solution, and blood at a range of temperatures (25 ºC room temperature, and 37 ºC physiological temperatures). According to the results of these studies, the optimal NP formulation under physiological conditions can be determined.

The development of the proposed theranostic nanocarriers will provide an alternative tool in the fight against cancer. The all data that obtained in this study is the basis for future projects in which the function of these NPs could be investigated *in vivo*. Theranostic probes that can be used as personalized diagnostic and therapeutic agents such as the one herein proposed will be valuable in the hands of oncologists. Optical imaging allows minimally invasive surgical approaches such as image-guided tumor resection with endoscopic procedures. Tumors that are small and dispersed can be treated by theranostic agents given at regular intervals. Simultaneous imaging and therapy feature of theranostics is a helpful strategy to monitor and treat the cancer using all-in-one nanoparticle.

APPENDIX SECTION

APPENDIX A

JOHN WILEY AND SONS LICENSE TERMS AND CONDITIONS

Jun 19, 2017

This Agreement between Texas State University -- Tugba Ozel Yildiz ("You") and John Wiley and Sons ("John Wiley and Sons") consists of your license details and the terms and conditions provided by John Wiley and Sons and Copyright Clearance Center.

License Number	4132600870393
License date	Jun 19, 2017
Licensed Content Publisher	John Wiley and Sons
Licensed Content Publication	Lasers in Surgery and Medicine
Licensed Content Title	Enzymatically activated near infrared nanoprobes based on amphiphilic block copolymers for optical detection of cancer
Licensed Content Author	Tuğba Özel,Sean White,Elaine Nguyen,Austin Moy,Nicholas Brenes,Bernard Choi,Tania Betancourt
Licensed Content Date	Jul 17, 2015
Licensed Content Pages	16
Type of use	Dissertation/Thesis
Requestor type	Author of this Wiley article
Format	Print and electronic
Portion	Full article
Will you be translating?	No
Title of your thesis / dissertation	BIODEGRADABLE ENZYMATICALLY ACTIVATED NANOPROBES FOR DUAL IMAGING AND THERAPY OF BREAST CANCER
Expected completion date	Aug 2017
Expected size (number of pages)	150
Requestor Location	Texas State University 601 University Dr. Centennial Hall 343 SAN MARCOS, TX 78666 United States Attn: Texas State University
Publisher Tax ID	EU826007151
Billing Type	Invoice
Billing Address	Texas State University 601 University Dr. Centennial Hall 343 SAN MARCOS, TX 78666 United States Attn: Texas State University
Total	0.00 USD

REFERENCES

(1) Jemal, A.; Tiwari, R.; Murray, T.; Ghafoor, A.; Samuels, A.; Ward, E.; Feuer, E.; Thun, M. Cancer Statistics , 2004. *CA Cancer J Clin.* **2004**, *54* (1), 8–29.

(2) WCRF. Data for cancer frequency by country: World Cancer Research Fund International http://www.wcrf.org/int/cancer-facts-figures/data-cancer-frequency-country.

(3) American Cancer Society. Cancer Facts & Figures 2016. *Cancer Facts Fig. 2016* **2016**, 1–9.

(4) Mariotto, A. B.; Robin Yabroff, K.; Shao, Y.; Feuer, E. J.; Brown, M. L. Projections of the Cost of Cancer Care in the United States: 2010-2020. *J. Natl. Cancer Inst.* **2011**, *103* (2), 117–128.

(5) DeSantis, C.; Ma, J.; Bryan, L.; Jemal, A. Breast Cancer Statistics, 2013. *CA. Cancer J. Clin.* **2014**, *64* (1), 52–62.

(6) Giaccone, G.; Pinedo, H. Drug Resistance. *Oncologist* **1996**, *1* (1 & 2), 82–87.

(7) Xu, X.; Xie, K.; Zhang, X.-Q.; Pridgen, E. M.; Park, G. Y.; Cui, D. S.; Shi, J.; Wu, J.; Kantoff, P. W.; Lippard, S. J.; Langer, R.; Walker, G. C.; Farokhzad, O. C. Enhancing Tumor Cell Response to Chemotherapy through Nanoparticle-Mediated Codelivery of siRNA and Cisplatin Prodrug. *Proc. Natl. Acad. Sci. U. S. A.* **2013**, *110* (46), 18638–18643.

(8) Du, Y.; Ren, W.; Li, Y.; Zhang, Q.; Zeng, L.; Chi, C.; Wu, A.; Tian, J. The Enhanced Chemotherapeutic Effects of Doxorubicin Loaded PEG Coated TiO 2 Nanocarriers in an Orthotopic Breast Tumor Bearing Mouse Model. *J. Mater. Chem. B* **2015**, *3* (8), 1518–1528.

(9) Chen, A. M.; Zhang, M.; Wei, D.; Stueber, D.; Taratula, O.; Minko, T.; He, H. Co-Delivery of Doxorubicin and Bcl-2 siRNA by Mesoporous Silica Nanoparticles Enhances the Efficacy of Chemotherapy in Multidrug-Resistant Cancer Cells. *Small* **2009**, *5* (23), 2673–2677.

(10) Wang, H.; Zhao, Y.; Wu, Y.; Hu, Y. lin; Nan, K.; Nie, G.; Chen, H. Enhanced Anti-Tumor Efficacy by Co-Delivery of Doxorubicin and Paclitaxel with Amphiphilic Methoxy PEG-PLGA Copolymer Nanoparticles. *Biomaterials* **2011**, *32* (32), 8281–8290.

(11) Taurin, S.; Greish, K. Enhanced Vascular Permeability in Solid Tumors: A Promise for Anticancer Nanomedicine. In *Tight Junctions in Cancer Metastasis*; Martin, T. A., Jiang, W. G., Eds.; Springer Netherlands: Dordrecht, 2013; pp 81–118.

(12) Weissleder, R.; Pittet, M. J. Imaging in the Era of Molecular Oncology. *Nature* **2008**, *452* (7187), 580–589.

(13) Lammers, T.; Kiessling, F.; Hennink, W. E.; Storm, G. Nanotheranostics and Image-Guided Drug Delivery: Current Concepts and Future Directions. *Mol. Pharm.* **2010**, *7* (6), 1899–1912.

(14) Özel, T.; White, S.; Nguyen, E.; Moy, A.; Brenes, N.; Choi, B.; Betancourt, T. Enzymatically Activated near Infrared Nanoprobes Based on Amphiphilic Block Copolymers for Optical Detection of Cancer. *Lasers Surg. Med.* **2015**, *47* (7), 579–594.

(15) Nagaich, U. Nanomedicine: Revolutionary Trends in Drug Delivery and Diagnostics. *J Adv Pharm Technol Res* **2014**, *5* (1), 1.

(16) Koo, H.; Huh, M. S.; Ryu, J. H.; Lee, D.-E.; Sun, I.-C.; Choi, K.; Kim, K.; Kwon, I. C. Nanoprobes for Biomedical Imaging in Living Systems. *Nano Today* **2011**, *6* (2), 204–220.

(17) Leroux, J.-C.; Allémann, E.; De Jaeghere, F.; Doelker, E.; Gurny, R. Biodegradable Nanoparticles — From Sustained Release Formulations to Improved Site Specific Drug Delivery. *J. Control. Release* **1996**, *39* (2–3), 339–350.

(18) Guo, Y.; Yuan, H.; Claudio, N. M.; Kura, S.; Shakerdge, N.; Mempel, T. R.; Bacskai, B. J.; Josephson, L. PEG-like Nanoprobes: Multimodal, Pharmacokinetically and Optically Tunable Nanomaterials. *PLoS One* **2014**, *9* (4).

(19) Banik, B. L.; Fattahi, P.; Brown, J. L. Polymeric Nanoparticles: The Future of Nanomedicine. *Wiley Interdisciplinary Reviews: Nanomedicine and Nanobiotechnology*. 2016, pp 271–299.

(20) Kumari, A.; Yadav, S. K.; Yadav, S. C. Biodegradable Polymeric Nanoparticles Based Drug Delivery Systems. *Colloids and Surfaces B: Biointerfaces*. 2010, pp 1–18.

(21) Masood, F. Polymeric Nanoparticles for Targeted Drug Delivery System for Cancer Therapy. *Mater. Sci. Eng. C* **2015**, *60*, 569–578.

(22) Danhier, F.; Lecouturier, N.; Vroman, B.; Jérôme, C.; Marchand-Brynaert, J.; Feron, O.; Préat, V. Paclitaxel-Loaded PEGylated PLGA-Based Nanoparticles: In Vitro and in Vivo Evaluation. *J. Control. Release* **2009**, *133* (1), 11–17.

(23) Liang, C.; Yang, Y.; Ling, Y.; Huang, Y.; Li, T.; Li, X. Improved Therapeutic Effect of Folate-Decorated PLGA-PEG Nanoparticles for Endometrial Carcinoma. *Bioorganic Med. Chem.* **2011**, *19* (13), 4057–4066.

(24) Luo, G.; Yu, X.; Jin, C.; Yang, F.; Fu, D.; Long, J.; Xu, J.; Zhan, C.; Lu, W. LyP-1-Conjugated Nanoparticles for Targeting Drug Delivery to Lymphatic Metastatic Tumors. *Int. J. Pharm.* **2010**, *385* (1–2), 150–156.

(25) Dhar, S.; Gu, F. X.; Langer, R.; Farokhzad, O. C.; Lippard, S. J. Targeted Delivery of Cisplatin to Prostate Cancer Cells by Aptamer Functionalized Pt(IV) Prodrug-PLGA-PEG Nanoparticles. *Proc Natl Acad Sci U S A* **2008**, *105* (45), 17356–17361.

(26) Danhier, F.; Pourcelle, V.; Marchand-Brynaert, J.; Jérôme, C.; Feron, O.; Préat, V. Targeting of Tumor Endothelium by RGD-Grafted PLGA-Nanoparticles. *Methods Enzymol.* **2012**, *508*, 157–175.

(27) Chen, H.; Gao, J.; Lu, Y.; Kou, G.; Zhang, H.; Fan, L.; Sun, Z.; Guo, Y.; Zhong, Y. Preparation and Characterization of PE38KDEL-Loaded Anti-HER2 Nanoparticles for Targeted Cancer Therapy. *J. Control. Release* **2008**, *128* (3), 209–216.

(28) Yokoyama, M.; Okano, T. Targetable Drug Carriers: Present Status and a Future Perspective. *Adv. Drug Deliv. Rev.* **1996**, *21* (2), 77–80.

(29) Folkman, J. Fundamental Concepts of the Angiogenic Process. *Curr. Mol. Med.* **2003**, *3* (7), 643–651.

(30) Fang, J.; Nakamura, H.; Maeda, H. The EPR Effect: Unique Features of Tumor Blood Vessels for Drug Delivery, Factors Involved, and Limitations and Augmentation of the Effect. *Advanced Drug Delivery Reviews*. 2011, pp 136–151.

(31) Wong, A. D.; Ye, M.; Ulmschneider, M. B.; Searson, P. C. Quantitative Analysis of the Enhanced Permeation and Retention (EPR) Effect. *PLoS One* **2015**, *10* (5).

(32) Byrne, J. D.; Betancourt, T.; Brannon-Peppas, L. Active Targeting Schemes for Nanoparticle Systems in Cancer Therapeutics. *Adv. Drug. Deliv. Rev.* **2008**, *60* (15), 1615–1626.

(33) Yokoyama, M. Drug Targeting with Nano-Sized Carrier Systems. *J. Artif. Organs* **2005**, *8* (2), 77–84.

(34) Owens 3rd, D. E.; Peppas, N. A. Opsonization, Biodistribution, and Pharmacokinetics of Polymeric Nanoparticles. *Int J Pharm* **2006**, *307* (1), 93–102.

(35) Peracchia, M. T.; Fattal, E.; Desmaële, D.; Besnard, M.; Noël, J. P.; Gomis, J. M.; Appel, M.; D'Angelo, J.; Couvreur, P. Stealth(®) PEGylated Polycyanoacrylate Nanoparticles for Intravenous Administration and Splenic Targeting. *J. Control. Release* **1999**, *60* (1), 121–128.

(36) Elsabahy, M.; Wooley, K. L. Design of Polymeric Nanoparticles for Biomedical Delivery Applications. *Chem. Soc. Rev.* **2012**, *41* (7), 2545.

(37) Moghimi, S. M.; Hunter, A. C.; Murray, J. C. Nanomedicine: Current Status and Future Prospects. *FASEB J.* **2005**, *19* (3), 311–330.

(38) Swami, A.; Shi, J.; Gadde, S.; Votruba, A. R.; Kolishetti, N.; Farokhzad, O. C. Nanoparticles for Targeted and Temporally Controlled Drug Delivery. In *Multifunctional Nanoparticles for Drug Delivery Applications*; 2012; pp 9–29.

(39) Alexis, F.; Pridgen, E.; Molnar, L. K.; Farokhzad, O. C. Factors Affecting the Clearance and Biodistribution of Polymeric Nanoparticles. In *Molecular Pharmaceutics*; 2008; Vol. 5, pp 505–515.

(40) Kong, G.; Braun, R. D.; Dewhirst, M. W. Hyperthermia Enables Tumor-Specific Nanoparticle Delivery: Effect of Particle Size. *Cancer Res.* **2000**, *60* (16), 4440–4445.

(41) Link, C.; Alexis, F.; Pridgen, E.; Molnar, L. K. Reviews Factors Affecting the Clearance and Biodistribution of. *Mol. Pharm.* **2008**, *5* (4), 505–515.

(42) Pillai, G. Nanomedicines for Cancer Therapy : An Update of FDA Approved and Those under Various Stages of Development. *SOJ Pharm Pharm Sci* **2014**, *1* (2), 1–13.

(43) Meany, D. L.; Sokoll, L. J.; Chan, D. W. Early Detection of Cancer: Immunoassays for Plasma Tumor Markers. *Expert Opin. Med. Diagn.* **2009**, *3* (6), 597–605.

(44) O'Farrell, A. C.; Shnyder, S. D.; Marston, G.; Coletta, P. L.; Gill, J. H. Non-Invasive Molecular Imaging for Preclinical Cancer Therapeutic Development. *Br. J. Pharmacol.* **2013**, *169* (4), 719–735.

(45) Hadjipanayis, C. G.; Jiang, H.; Roberts, D. W.; Yang, L. Current and Future Clinical Applications for Optical Imaging of Cancer: From Intraoperative Surgical Guidance to Cancer Screening. *Semin Oncol* **2011**, *38* (1), 109–118.

(46) Sevick-Muraca, E. M. Translation of near-Infrared Fluorescence Imaging Technologies: Emerging Clinical Applications. *Annu Rev Med* **2012**, *63*, 217–231.

(47) Nguyen, Q. T.; Olson, E. S.; Aguilera, T. A.; Jiang, T.; Scadeng, M.; Ellies, L. G.; Tsien, R. Y. Surgery with Molecular Fluorescence Imaging Using Activatable Cell-Penetrating Peptides Decreases Residual Cancer and Improves Survival. *Proc. Natl. Acad. Sci.* **2010**, *107* (9), 4317–4322.

(48) Nguyen, Q. T.; Tsien, R. Y. Fluorescence-Guided Surgery with Live Molecular Navigation — a New Cutting Edge. *Nat. Rev. Cancer* **2013**, *13* (9), 653–662.

(49) Yi, X.; Wang, F.; Qin, W.; Yang, X.; Yuan, J. Near-Infrared Fluorescent Probes in Cancer Imaging and Therapy: An Emerging Field. *Int. J. Nanomedicine* **2014**, 1347.

(50) Chatterjee, D. K.; Fong, L. S.; Zhang, Y. Nanoparticles in Photodynamic Therapy: An Emerging Paradigm. *Advanced Drug Delivery Reviews*. 2008, pp 1627–1637.

(51) Ntziachristos, V.; Bremer, C.; Weissleder, R. Fluorescence Imaging with near-Infrared Light: New Technological Advances That Enable in Vivo Molecular Imaging. *Eur Radiol* **2003**, *13* (1), 195–208.

(52) Snoeks, T. J. A.; Khmelinskii, A.; Lelieveldt, B. P. F.; Kaijzel, E. L.; Löwik, C. W. G. M. Optical Advances in Skeletal Imaging Applied to Bone Metastases. *Bone*. 2011, pp 106–114.

(53) Tanaka, Y. Impact of near-Infrared Radiation in Dermatology. *World J. Dermatology* **2012**, *1* (3), 30.

(54) Luo, S.; Zhang, E.; Su, Y.; Cheng, T.; Shi, C. A Review of NIR Dyes in Cancer Targeting and Imaging. *Biomaterials*. 2011, pp 7127–7138.

(55) Intes, X.; Ripoll, J.; Chen, Y.; Nioka, S.; Yodh, A. G.; Chance, B. *In Vivo* Continuous-Wave Optical Breast Imaging Enhanced with Indocyanine Green. *Med. Phys.* **2003**, *30* (6), 1039–1047.

(56) Gurfinkel, M.; Thompson, A. B.; Ralston, W.; Troy, T. L.; Moore, A. L.; Moore, T. A.; Gust, J. D.; Tatman, D.; Reynolds, J. S.; Muggenburg, B.; Nikula, K.; Pandey, R.; Mayer, R. H.; Hawrysz, D. J.; Sevick-Muraca, E. M. Pharmacokinetics of ICG and HPPH-Car for the Detection of Normal and Tumor Tissue Using Fluorescence, near-Infrared Reflectance Imaging: A Case Study. *Photochem. Photobiol.* **2000**, *72* (1), 94–102.

(57) Hamon, C. L.; Dorsey, C. L.; ??zel, T.; Barnes, E. M.; Hudnall, T. W.; Betancourt, T. Near-Infrared Fluorescent Aza-BODIPY Dye-Loaded Biodegradable Polymeric Nanoparticles for Optical Cancer Imaging. *J. Nanoparticle Res.* **2016**, *18* (7).

(58) Lim, C. K.; Shin, J.; Lee, Y. D.; Kim, J.; Oh, K. S.; Yuk, S. H.; Jeong, S. Y.; Kwon, I. C.; Kim, S. Phthalocyanine-Aggregated Polymeric Nanoparticles as Tumor-Homing near-Infrared Absorbers for Photothermal Therapy of Cancer. *Theranostics* **2012**, *2* (9), 871–879.

(59) Yue, C.; Liu, P.; Zheng, M.; Zhao, P.; Wang, Y.; Ma, Y.; Cai, L. IR-780 Dye Loaded Tumor Targeting Theranostic Nanoparticles for NIR Imaging and Photothermal Therapy. *Biomaterials* **2013**, *34* (28), 6853–6861.

(60) Crielaard, B. J.; Lammers, T.; Schiffelers, R. M.; Storm, G. Drug Targeting Systems for Inflammatory Disease: One for All, All for One. *Journal of Controlled Release*. 2012, pp 225–234.

(61) Patel, S. K.; Janjic, J. M. Macrophage Targeted Theranostics as Personalized Nanomedicine Strategies for Inflammatory Diseases. *Theranostics*. 2015, pp 150–172.

(62) Singh, A. V.; Khare, M.; Gade, W. N.; Zamboni, P. Theranostic Implications of Nanotechnology in Multiple Sclerosis: A Future Perspective. *Autoimmune Diseases*. 2012.

(63) McCarthy, J. R.; Korngold, E.; Weissleder, R.; Jaffer, F. A. A Light-Activated Theranostic Nanoagent for Targeted Macrophage Ablation in Inflammatory Atherosclerosis. *Small* **2010**, *6* (18), 2041–2049.

(64) Bolognesi, M. L.; Gandini, A.; Prati, F.; Uliassi, E. From Companion Diagnostics to Theranostics: A New Avenue for Alzheimer's Disease? *Journal of Medicinal Chemistry*. 2016, pp 7759–7770.

(65) Aulić, S.; Bolognesi, M. L.; Legname, G. Small-Molecule Theranostic Probes: A Promising Future in Neurodegenerative Diseases. *International Journal of Cell Biology*. 2013.

(66) Perkovic, M. N.; Erjavec, G. N.; Strac, D. S.; Uzun, S.; Kozumplik, O.; Pivac, N. Theranostic Biomarkers for Schizophrenia. *International Journal of Molecular Sciences*. 2017.

(67) Wang, P.; Moore, A. Theranostic MRI: The Future for Type 1 Diabetes Management? *Imaging Med.* **2014**, *6* (1), 25–39.

(68) Wang, P.; Moore, A. Theranostic Magnetic Resonance Imaging of Type 1 Diabetes and Pancreatic Islet Transplantation. *Quant. Imaging Med. Surg.* **2012**, *2* (14), 151–162.

(69) Howell, M.; Wang, C.; Mahmoud, A.; Hellermann, G.; Mohapatra, S. S.; Mohapatra, S. Dual-Function Theranostic Nanoparticles for Drug Delivery and Medical Imaging Contrast: Perspectives and Challenges for Use in Lung Diseases. *Drug Delivery and Translational Research*. 2013, pp 352–363.

(70) Wang, D.; Lin, B.; Ai, H. Theranostic Nanoparticles for Cancer and Cardiovascular Applications. *Pharmaceutical Research*. 2014, pp 1390–1406.

(71) McCarthy, J. R. Multifunctional Agents for Concurrent Imaging and Therapy in Cardiovascular Disease. *Advanced Drug Delivery Reviews*. 2010, pp 1023–1030.

(72) Chen, X.; Wong, S. T. C. Cancer Theranostics. In *Cancer Theranostics*; Elsevier, 2014; pp 3–8.

(73) Vahrmeijer, A. L.; Hutteman, M.; van der Vorst, J. R.; van de Velde, C. J. H.; Frangioni, J. V. Image-Guided Cancer Surgery Using near-Infrared Fluorescence. *Nat. Rev. Clin. Oncol.* **2013**, *10* (9), 507–518.

(74) Yu, M. K.; Park, J.; Jon, S. Targeting Strategies for Multifunctional Nanoparticles in Cancer Imaging and Therapy. *Theranostics* **2012**, *2* (1), 3–44.

(75) Yu, M. K.; Jeong, Y. Y.; Park, J.; Park, S.; Kim, J. W.; Min, J. J.; Kim, K.; Jon, S. Drug-Loaded Superparamagnetic Iron Oxide Nanoparticles for Combined Cancer Imaging and Therapy In Vivo. *Angew. Chemie Int. Ed.* **2008**, *47* (29), 5362–5365.

(76) Bagalkot, V.; Zhang, L.; Levy-Nissenbaum, E.; Jon, S.; Kantoff, P. W.; Langery, R.; Farokhzad, O. C. Quantum Dot-Aptamer Conjugates for Synchronous Cancer Imaging, Therapy, and Sensing of Drug Delivery Based on Bi-Fluorescence Resonance Energy Transfer. *Nano Lett.* **2007**, *7* (10), 3065–3070.

(77) Liang, C.; Diao, S.; Wang, C.; Gong, H.; Liu, T.; Hong, G.; Shi, X.; Dai, H.; Liu, Z. Tumor Metastasis Inhibition by Imaging-Guided Photothermal Therapy with Single-Walled Carbon Nanotubes. *Adv. Mater.* **2014**, *26* (32), 5646–5652.

(78) Huang, P.; Lin, J.; Li, W.; Rong, P.; Wang, Z.; Wang, S.; Wang, X.; Sun, X.; Aronova, M.; Niu, G.; Leapman, R. D.; Nie, Z.; Chen, X. Biodegradable Gold Nanovesicles with an Ultrastrong Plasmonic Coupling Effect for Photoacoustic Imaging and Photothermal Therapy. *Angew. Chemie - Int. Ed.* **2013**, *52* (52), 13958–13964.

(79) Roy, I.; Ohulchanskyy, T. Y.; Pudavar, H. E.; Bergey, E. J.; Oseroff, A. R.; Morgan, J.; Dougherty, T. J.; Prasad, P. N. Ceramic-Based Nanoparticles Entrapping Water-Insoluble Photosensitizing Anticancer Drugs: A Novel Drug-Carrier System for Photodynamic Therapy. *J. Am. Chem. Soc.* **2003**, *125* (26), 7860–7865.

(80) Talelli, M.; Rijcken, C. J. F.; van Nostrum, C. F.; Storm, G.; Hennink, W. E. Micelles Based on HPMA Copolymers. *Advanced Drug Delivery Reviews*. 2010, pp 231–239.

(81) Bourrinet, P.; Bengele, H. H.; Bonnemain, B.; Dencausse, A.; Idee, J.-M.; Jacobs, P. M.; Lewis, J. M. Preclinical Safety and Pharmacokinetic Profile of Ferumoxtran-10, an Ultrasmall Superparamagnetic Iron Oxide Magnetic Resonance Contrast Agent. *Invest. Radiol.* **2006**, *41* (3), 313–324.

(82) Michalet, X.; Pinaud, F. F.; Bentolila, L. A.; Tsay, J. M.; Doose, S.; Li, J. J.; Sundaresan, G.; Wu, A. M.; Gambhir, S. S.; Weiss, S. Quantum Dots for Live Cells, in Vivo Imaging, and Diagnostics. *Science* **2005**, *307* (5709), 538–544.

(83) Derfus, A. M.; Chan, W. C. W.; Bhatia, S. N. Probing the Cytotoxicity of Semiconductor Quantum Dots. *Nano Lett.* **2004**, *4* (1), 11–18.

(84) Kam, N. W. S.; Liu, Z.; Dai, H. Functionalization of Carbon Nanotubes via Cleavable Disulfide Bonds for Efficient Intracellular Delivery of siRNA and Potent Gene Silencing. *J. Am. Chem. Soc.* **2005**, *127* (36), 12492–12493.

(85) Moreno-Vega, A. I.; Gómez-Quintero, T.; Nuñez-Anita, R. E.; Acosta-Torres, L. S.; Castaño, V. Polymeric and Ceramic Nanoparticles in Biomedical Applications. *Journal of Nanotechnology*. 2012.

(86) Xiong, Y.; Jiang, W.; Shen, Y.; Li, H.; Sun, C.; Ouahab, A.; Tu, J. A Poly(??, L-Glutamic Acid)-Citric Acid Based Nanoconjugate for Cisplatin Delivery. *Biomaterials* **2012**, *33* (29), 7182–7193.

(87) American Cancer Society. Cancer Facts & Figures 2015. *Cancer Facts Fig. 2015* **2015**, 1–9.

(88) Chi, C.; Du, Y.; Ye, J.; Kou, D.; Qiu, J.; Wang, J.; Tian, J.; Chen, X. Intraoperative Imaging-Guided Cancer Surgery: From Current Fluorescence Molecular Imaging Methods to Future Multi-Modality Imaging Technology. *Theranostics* **2014**, *4* (11), 1072–1084.

(89) Kishimoto, H.; Zhao, M.; Hayashi, K.; Urata, Y.; Tanaka, N.; Fujiwara, T.; Penman, S.; Hoffman, R. M. In Vivo Internal Tumor Illumination by Telomerase-Dependent Adenoviral GFP for Precise Surgical Navigation. *Proc Natl Acad Sci U S A* **2009**, *106* (34), 14514–14517.

(90) Weissleder, R.; Tung, C.-H.; Mahmood, U.; Bogdanov, A. J. In-Vivo Imaging of Tumors with Protease Activated near-Infrared Fluorescent Probes. *Nat. Biotechnol.* **1999**, *17*, 375–378.

(91) Mahmood, U.; Tung, C.; Bogdanov, A.; Weissleder, R. Near-Infrared Optical Imaging of Protease Activity for Tumor Detection. *Radiology* **1999**, *213* (3), 866–870.

(92) Sheth, R. A.; Upadhyay, R.; Stangenberg, L.; Sheth, R.; Weissleder, R.; Mahmood, U. Improved Detection of Ovarian Cancer Metastases by Intraoperative Quantitative Fluorescence Protease Imaging in a Pre-Clinical Model. *Gynecol. Oncol.* **2009**, *112* (3), 616–622.

(93) Habibollahi, P.; Figueiredo, J. L.; Heidari, P.; Dulak, A. M.; Imamura, Y.; Bass, A. J.; Ogino, S.; Chan, A. T.; Mahmood, U. Optical Imaging with a Cathepsin B Activated Probe for the Enhanced Detection of Esophageal Adenocarcinoma by Dual Channel Fluorescent Upper GI Endoscopy. *Theranostics* **2012**, *2* (2), 227–234.

(94) Ding, S.; Eric Blue, R.; Chen, Y.; Scull, B.; Kay Lund, P.; Morgan, D. Molecular Imaging of Gastric Neoplasia with near-Infrared Fluorescent Activatable Probes. *Mol Imaging* **2012**, *11* (6), 507–515.

(95) Mito, J. K.; Ferrer, J. M.; Brigman, B. E.; Lee, C. L.; Dodd, R. D.; Eward, W. C.; Marshall, L. F.; Cuneo, K. C.; Carter, J. E.; Ramasunder, S.; Kim, Y.; Lee, W. D.; Griffith, L. G.; Bawendi, M. G.; Kirsch, D. G. Intraoperative Detection and Removal of Microscopic Residual Sarcoma Using Wide-Field Imaging. *Cancer* **2012**, *118* (21), 5320–5330.

(96) Cuneo, K. C.; Mito, J. K.; Javid, M. P.; Ferrer, J. M.; Kim, Y.; Lee, W. D.; Bawendi, M. G.; Brigman, B. E.; Kirsch, D. G. Imaging Primary Mouse Sarcomas after Radiation Therapy Using Cathepsin-Activatable Fluorescent Imaging Agents. *Int J Radiat Oncol Biol Phys* **2013**, *86* (1), 136–142.

(97) Agarwal, A.; Boettcher, A.; Kneuer, R.; Sari-Sarraf, F.; Donovan, A.; Woelcke, J.; Simic, O.; Brandl, T.; Krucker, T. In Vivo Imaging with Fluorescent Smart Probes to Assess Treatment Strategies for Acute Pancreatitis. *PLoS One* **2013**, *8* (2).

(98) Haller, J.; Hyde, D.; Deliolanis, N.; de Kleine, R.; Niedre, M.; Ntziachristos, V. Visualization of Pulmonary Inflammation Using Noninvasive Fluorescence Molecular Imaging. *J. Appl. Physiol.* **2008**, *104* (3), 795–802.

(99) Chen, J.; Tung, C. H.; Mahmood, U.; Ntziachristos, V.; Gyurko, R.; Fishman, M. C.; Huang, P. L.; Weissleder, R. In Vivo Imaging of Proteolytic Activity in Atherosclerosis. *Circulation* **2002**, *105* (23), 2766–2771.

(100) Deguchi, J. O.; Aikawa, M.; Tung, C. H.; Aikawa, E.; Kim, D. E.; Ntziachristos, V.; Weissleder, R.; Libby, P. Inflammation in Atherosclerosis: Visualizing Matrix Metalloproteinase Action in Macrophages in Vivo. *Circulation* **2006**, *114* (1), 55–62.

(101) Jaffer, F. A.; Vinegoni, C.; John, M. C.; Aikawa, E.; Gold, H. K.; Finn, A. V.; Ntziachristos, V.; Libby, P.; Weissleder, R. Real-Time Catheter Molecular Sensing of Inflammation in Proteolytically Active Atherosclerosis. *Circulation* **2008**, *118* (18), 1802–1809.

(102) Jaffer, F. A.; Calfon, M. A.; Rosenthal, A.; Mallas, G.; Razansky, R. N.; Mauskapf, A.; Weissleder, R.; Libby, P.; Ntziachristos, V. Two-Dimensional Intravascular near-Infrared Fluorescence Molecular Imaging of Inflammation in Atherosclerosis and Stent-Induced Vascular Injury. *J. Am. Coll. Cardiol.* **2011**, *57* (25), 2516–2526.

(103) Calfon, M. A.; Rosenthal, A.; Mallas, G.; Mauskapf, A.; Nudelman, R. N.; Ntziachristos, V.; Jaffer, F. A. In Vivo Near Infrared Fluorescence (NIRF) Intravascular Molecular Imaging of Inflammatory Plaque, a Multimodal Approach to Imaging of Atherosclerosis. *J Vis Exp* **2011**, *54*, e2257.

(104) Razansky, D.; Harlaar, N. J.; Hillebrands, J. L.; Taruttis, A.; Herzog, E.; Zeebregts, C. J.; van Dam, G. M.; Ntziachristos, V. Multispectral Optoacoustic Tomography of Matrix Metalloproteinase Activity in Vulnerable Human Carotid Plaques. *Mol Imaging Biol* **2012**, *14*, 277–285.

(105) Goergen, C. J.; Chen, H. H.; Bogdanov Jr., A.; Sosnovik, D. A.; Kumar, A. T. N. In Vivo Fluorescence Lifetime Detection of an Activatable Probe in Infarcted Myocardium. *J Biomed Opt* **2012**, *17* (5), 56001.

(106) Josephson, L.; Kircher, M. F.; Mahmood, U.; Tang, Y.; Weissleder, R. Near-Infrared Fluorescent Nanoparticles as Combined MR/optical Imaging Probes. *Bioconjug. Chem.* **2002**, *13* (3), 554–560.

(107) Kircher, M. F.; Weissleder, R.; Josephson, L. A Dual Fluorochrome Probe for Imaging Proteases. *Bioconjug. Chem.* **2004**, *15* (2), 242–248.

(108) Salthouse, C. D.; Reynolds, F.; Tam, J. M.; Josephson, L.; Mahmood, U. Quantitative Measurement of Protease Activity with Correction of Probe Delivery and Tissue Absorption Effects. *Sensors Actuators, B Chem.* **2009**, *138* (2), 591–597.

(109) Lee, S.; Cha, E. J.; Park, K.; Lee, S. Y.; Hong, J. K.; Sun, I. C.; Kim, S. Y.; Choi, K.; Kwon, I. C.; Kim, K.; Ahn, C. H. A near-Infrared-Fluorescence-Quenched Gold-Nanoparticle Imaging Probe for in Vivo Drug Screening and Protease Activity Determination. *Angew. Chemie - Int. Ed.* **2008**, *47* (15), 2804–2807.

(110) Achatz, D. E.; Mezo, G.; Kele, P.; Wolfbeis, O. S. Probing the Activity of Matrix Metalloproteinase II with a Sequentially Click-Labeled Silica Nanoparticle FRET Probe. *ChemBioChem* **2009**, *10* (14), 2316–2320.

(111) Lee, S.; Ryu, J. H.; Park, K.; Lee, A.; Lee, S. Y.; Youn, I. C.; Ahn, C. H.; Yoon, S. M.; Myung, S. J.; Moon, D. H.; Chen, X.; Choi, K.; Kwon, I. C.; Kim, K. Polymeric Nanoparticle-Based Activatable near-Infrared Nanosensor for Protease Determination in Vivo. *Nano Lett.* **2009**, *9* (12), 4412–4416.

(112) McDonald, D. M.; Baluk, P. Significance of Blood Vessel Leakiness in Cancer. *Cancer Res* **2002**, *62* (18), 5381–5385.

(113) Yokoyama, M.; Okano, T. Targetable Drug Carriers: Present Status and Future Perspectives. *Adv Drug Deliv Rev* **1996**, *21*, 77–80.

(114) Folkman, J.; Merler, E.; Abernathy, C.; Williams, G. Isolation of a Tumor Factor Responsible for Angiogenesis. *J Exp Med* **1971**, *133* (2), 275–288.

(115) Whitney, J. R.; Sarkar, S.; Zhang, J.; Do, T.; Young, T.; Manson, M. K.; Campbell, T. A.; Puretzky, A. A.; Rouleau, C. M.; More, K. L.; Geohegan, D. B.; Rylander, C. G.; Dorn, H. C.; Rylander, M. N. Single Walled Carbon Nanohorns as Photothermal Cancer Agents. *Lasers Surg Med* **2011**, *43* (1), 43–51.

(116) Whitney, J.; DeWitt, M.; Whited, B. M.; Carswell, W.; Simon, A.; Rylander, C. G.; Rylander, M. N. 3D Viability Imaging of Tumor Phantoms Treated with Single-Walled Carbon Nanohorns and Photothermal Therapy. *Nanotechnology* **2013**, *24* (27), 275102.

(117) Pattani, V. P.; Tunnell, J. W. Nanoparticle-Mediated Photothermal Therapy: A Comparative Study of Heating for Different Particle Types. *Lasers Surg. Med.* **2012**, *44* (8), 675–684.

(118) Lin, A. Y.; Almeida, J. P.; Bear, A.; Liu, N.; Luo, L.; Foster, A. E.; Drezek, R. A. Gold Nanoparticle Delivery of Modified CpG Stimulates Macrophages and Inhibits Tumor Growth for Enhanced Immunotherapy. *PLoS One* **2013**, *8* (5), e63550.

(119) Park, J.; Estrada, A.; Schwartz, J. A.; Diagaradjane, P.; Krishnan, S.; Dunn, A. K.; Tunnell, J. W. Intra-Organ Biodistribution of Gold Nanoparticles Using Intrinsic Two-Photon Induced Photoluminescence. *Lasers Surg Med* **2010**, *42* (7), 630–639.

(120) Puvanakrishnan, P.; Diagaradjane, P.; Kazmi, S. M.; Dunn, A. K.; Krishnan, S.; Tunnell, J. W. Narrow Band Imaging of Squamous Cell Carcinoma Tumors Using Topically Delivered Anti-EGFR Antibody Conjugated Gold Nanorods. *Lasers Surg Med* **2012**, *44* (4), 310–317.

(121) Prencipe, G.; Tabakman, S. M.; Welsher, K.; Liu, Z.; Goodwin, A. P.; Zhang, L.; Henry, J.; Dai, H. PEG Branched Polymer for Functionalization of Nanomaterials with Ultralong Blood Circulation. *J Am Chem Soc* **2009**, *131* (13), 4783–4787.

(122) Torchilin, V. P. Which Polymer Can Make Nanoparticulate Drug Carriers Long-Circulating? *Adv Drug Deliv Rev* **1995**, *16* (2–3), 141–155.

(123) Avgoustakis, K. Pegylated Poly(lactide) and Poly(lactide-Co-Glycolide) Nanoparticles: Preparation, Properties and Possible Applications in Drug Delivery. *Curr Drug Deliv* **2004**, *1* (4), 321–333.

(124) Gref, R.; Luck, M.; Quellec, P.; Marchand, M.; Dellacherie, E.; Harnisch, S.; Blunk, T.; Muller, R. H. "Stealth" Corona-Core Nanoparticles Surface Modified by Polyethylene Glycol (PEG): Influences of the Corona (PEG Chain Length and Surface Density) and of the Core Composition on Phagocytic Uptake and Plasma Protein Adsorption. *Colloids Surf B Biointerfaces* **2000**, *18* (3–4), 301–313.

(125) Mehvar, R. Modulation of the Pharmacokinetics and Pharmacodynamics of Proteins by Polyethylene Glycol Conjugation. *J Pharm Pharm Sci* **2000**, *3* (1), 125–136.

(126) Ishii, T.; Otsuka, H.; Kataoka, K.; Nagasaki, Y. Preparation of Functionally Pegylated Gold Nanoparticles with Narrow Distribution through Autoreduction of Auric Cation by Alpha-Biotinyl-PEG-Block-[poly(2- (N,N-Dimethylamino)ethyl Methacrylate)]. *Langmuir* **2004**, *20* (3), 561–564.

(127) Betancourt, T.; Byrne, J. D.; Sunaryo, N.; Crowder, S. W.; Kadapakkam, M.; Patel, S.; Casciato, S.; Brannon-Peppas, L. PEGylation Strategies for Active Targeting of PLA/PLGA Nanoparticles. *J Biomed Mater Res A* **2009**, *91* (1), 263–276.

(128) Betancourt, T.; Brown, B.; Brannon-Peppas, L. Doxorubicin-Loaded PLGA Nanoparticles by Nanoprecipitation: Preparation, Characterization and in Vitro Evaluation. *Nanomedicine (Lond).* **2007**, *2* (2), 219–232.

(129) Blum, G.; von Degenfeld, G.; Merchant, M. J.; Blau, H. M.; Bogyo, M. Noninvasive Optical Imaging of Cysteine Protease Activity Using Fluorescently Quenched Activity-Based Probes. *Nat Chem Biol* **2007**, *3* (10), 668–677.

(130) Gal, N.; Massalha, S.; Samuelly-Nafta, O.; Weihs, D. Effects of Particle Uptake, Encapsulation, and Localization in Cancer Cells on Intracellular Applications. *Med. Eng. Phys.* **2015**, *37* (5), 478–483.

(131) Zhang, Y.; Yang, M.; Portney, N. G.; Cui, D.; Budak, G.; Ozbay, E.; Ozkan, M.; Ozkan, C. S. Zeta Potential: A Surface Electrical Characteristic to Probe the Interaction of Nanoparticles with Normal and Cancer Human Breast Epithelial Cells. *Biomed. Microdevices* **2008**, *10* (2), 321–328.

(132) Li, C.; Greenwood, T. R.; Glunde, K. Glucosamine-Bound Near-Infrared Fluorescent Probes with Lysosomal Specificity for Breast Tumor Imaging. *Neoplasia* **2008**, *10* (4), 389–398.

(133) Devaraj, N. K.; Hilderbrand, S.; Upadhyay, R.; Mazitschek, R.; Weissleder, R. Bioorthogonal Turn-on Probes for Imaging Small Molecules inside Living Cells. *Angew. Chemie - Int. Ed.* **2010**, *49* (16), 2869–2872.

(134) Devaraj, N. K.; Weissleder, R. Biomedical Applications of Tetrazine Cycloadditions. *Acc. Chem. Res.* **2011**, *44* (9), 816–827.

(135) Karver, M. R.; Weissleder, R.; Hilderbrand, S. A. Bioorthogonal Reaction Pairs Enable Simultaneous, Selective, Multi-Target Imaging. *Angew. Chemie - Int. Ed.* **2012**, *51* (4), 920–922.

(136) Devaraj, N. K.; Thurber, G. M.; Keliher, E. J.; Marinelli, B.; Weissleder, R. Reactive Polymer Enables Efficient in Vivo Bioorthogonal Chemistry. *Proc. Natl. Acad. Sci.* **2012**, *109* (13), 4762–4767.

(137) Li, J.; Chen, K.; Liu, H.; Cheng, K.; Yang, M.; Zhang, J.; Cheng, J. D.; Zhang, Y.; Cheng, Z. Activatable near-Infrared Fluorescent Probe for in Vivo Imaging of Fibroblast Activation Protein-Alpha. *Bioconjug. Chem.* **2012**, *23* (8), 1704–1711.

(138) Ryu, J. H.; Lee, A.; Na, J. H.; Lee, S.; Ahn, H. J.; Park, J. W.; Ahn, C. H.; Kim, B. S.; Kwon, I. C.; Choi, K.; Youn, I.; Kim, K. Optimization of Matrix Metalloproteinase Fluorogenic Probes for Osteoarthritis Imaging. *Amino Acids* **2011**, *41* (5), 1113–1122.

(139) Yhee, J. Y.; Kim, S. A.; Koo, H.; Son, S.; Ryu, J. H.; Youn, I. C.; Choi, K.; Kwon, I. C.; Kim, K. Optical Imaging of Cancer-Related Proteases Using near-Infrared Fluores-Cence Matrix Metalloproteinase-Sensitive and Cathepsin B-Sensitive Probes. *Theranostics* **2012**, *2* (2), 179–189.

(140) Olson, E. S.; Whitney, M. A.; Friedman, B.; Aguilera, T. A.; Crisp, J. L.; Baik, F. M.; Jiang, T.; Baird, S. M.; Tsimikas, S.; Tsien, R. Y.; Nguyen, Q. T. In Vivo Fluorescence Imaging of Atherosclerotic Plaques with Activatable Cell-Penetrating Peptides Targeting Thrombin Activity. *Integr. Biol. (Camb).* **2012**, *4* (6), 595–605.

(141) Shi, N. Q.; Gao, W.; Xiang, B.; Qi, X. R. Enhancing Cellular Uptake of Activable Cell-Penetrating Peptide-Doxorubicin Conjugate by Enzymatic Cleavage. *Int. J. Nanomedicine* **2012**, *7*, 1613–1621.

(142) Galande, A. K.; Hilderbrand, S. A.; Weissleder, R.; Tung, C. H. Enzyme-Targeted Fluorescent Imaging Probes on a Multiple Antigenic Peptide Core. *J. Med. Chem.* **2006**, *49* (15), 4715–4720.

(143) Singh, H. D.; Bushnak, I.; Unsworth, L. D. Engineered Peptides with Enzymatically Cleavable Domains for Controlling the Release of Model Protein Drug From “soft” nanoparticles. *Acta Biomater* **2012**, *8* (2), 636–645.

(144) Glangchai, L. C.; Caldorera-Moore, M.; Shi, L.; Roy, K. Nanoimprint Lithography Based Fabrication of Shape-Specific, Enzymatically-Triggered Smart Nanoparticles. *J Control Release* **2008**, *125* (3), 263–272.

(145) Liaudet-Coopman, E.; Beaujouin, M.; Derocq, D.; Garcia, M.; Glondu-Lassis, M.; Laurent-Matha, V.; Prebois, C.; Rochefort, H.; Vignon, F. Cathepsin D: Newly Discovered Functions of a Long-Standing Aspartic Protease in Cancer and Apoptosis. *Cancer Lett* **2006**, *237* (2), 167–179.

(146) Heidtmann, H. H.; Salge, U.; Abrahamson, M.; Bencina, M.; Kastelic, L.; Kopitar-Jerala, N.; Turk, V.; Lah, T. T. Cathepsin B and Cysteine Proteinase Inhibitors in Human Lung Cancer Cell Lines. *Clin Exp Metastasis* **1997**, *15* (4), 368–381.

(147) Werle, B.; Kraft, C.; Lah, T. T.; Kos, J.; Schanzenbacher, U.; Kayser, K.; Ebert, W.; Spiess, E. Cathepsin B in Infiltrated Lymph Nodes Is of Prognostic Significance for Patients with Nonsmall Cell Lung Carcinoma. *Cancer* **2000**, *89* (11), 2282–2291.

(148) Campo, E.; Munoz, J.; Miquel, R.; Palacin, A.; Cardesa, A.; Sloane, B. F.; Emmert-Buck, M. R. Cathepsin B Expression in Colorectal Carcinomas Correlates with Tumor Progression and Shortened Patient Survival. *Am J Pathol* **1994**, *145* (2), 301–309.

(149) Bremer, C.; Tung, C. H.; Weissleder, R. In Vivo Molecular Target Assessment of Matrix Metalloproteinase Inhibition. *Nat Med* **2001**, *7* (6), 743–748.

(150) Minko, T.; Kopeckova, P.; Kopecek, J. Efficacy of the Chemotherapeutic Action of HPMA Copolymer-Bound Doxorubicin in a Solid Tumor Model of Ovarian Carcinoma. *Int J Cancer* **2000**, *86* (1), 108–117.

(151) Xie, J.; Lee, S.; Chen, X. Nanoparticle-Based Theranostic Agents. *Advanced Drug Delivery Reviews*. 2010, pp 1064–1079.

(152) Nair, L. S.; Laurencin, C. T. Polymers as Biomaterials for Tissue Engineering and Controlled Drug Delivery. *Advances in Biochemical Engineering/Biotechnology*. 2006, pp 47–90.

(153) Zhu, X.; Anquillare, E. L. B.; Farokhzad, O. C.; Shi, J. Polymer- and Protein-Based Nanotechnologies for Cancer Theranostics. In *Cancer Theranostics*; 2014; pp 419–436.

(154) Vicent, M. J.; Duncan, R. Polymer Conjugates: Nanosized Medicines for Treating Cancer. *Trends in Biotechnology*. 2006, pp 39–47.

(155) Duncan, R.; Vicent, M. J.; Greco, F.; Nicholson, R. I. Polymer-Drug Conjugates: Towards a Novel Approach for the Treatment of Endrocine-Related Cancer. In *Endocrine-Related Cancer*; 2005; Vol. 12.

(156) Larson, N.; Ghandehari, H. Polymeric Conjugates for Drug Delivery. *Chemistry of Materials*. 2012, pp 840–853.

(157) Zarabi, B.; Borgman, M. P.; Zhuo, J.; Gullapalli, R.; Ghandehari, H. Noninvasive Monitoring of HPMA Copolymer-RGDfK Conjugates by Magnetic Resonance Imaging. *Pharm. Res.* **2009**, *26* (5), 1121–1129.

(158) Mora-Huertas, C. E.; Fessi, H.; Elaissari, A. Polymer-Based Nanocapsules for Drug Delivery. *International Journal of Pharmaceutics*. 2010, pp 113–142.

(159) Liu, P.; Yu, H.; Sun, Y.; Zhu, M.; Duan, Y. A mPEG-PLGA-B-PLL Copolymer Carrier for Adriamycin and siRNA Delivery. *Biomaterials* **2012**, *33* (17), 4403–4412.

(160) Lee, J. S.; Feijen, J. Polymersomes for Drug Delivery: Design, Formation and Characterization. *Journal of Controlled Release*. 2012, pp 473–483.

(161) Letchford, K.; Burt, H. A Review of the Formation and Classification of Amphiphilic Block Copolymer Nanoparticulate Structures: Micelles, Nanospheres, Nanocapsules and Polymersomes. *European Journal of Pharmaceutics and Biopharmaceutics*. 2007, pp 259–269.

(162) Sanson, C.; Diou, O.; Th??venot, J.; Ibarboure, E.; Soum, A.; Br??let, A.; Miraux, S.; Thiaudi??re, E.; Tan, S.; Brisson, A.; Dupuis, V.; Sandre, O.; Lecommandoux, S. Doxorubicin Loaded Magnetic Polymersomes: Theranostic Nanocarriers for MR Imaging and Magneto-Chemotherapy. *ACS Nano* **2011**, *5* (2), 1122–1140.

(163) Kesharwani, P.; Jain, K.; Jain, N. K. Dendrimer as Nanocarrier for Drug Delivery. *Progress in Polymer Science*. 2014, pp 268–307.

(164) Khandare, J.; Calderón, M.; Dagia, N. M.; Haag, R. Multifunctional Dendritic Polymers in Nanomedicine: Opportunities and Challenges. *Chem. Soc. Rev.* **2012**, *41* (7), 2824–2848.

(165) Xu, S.; Luo, Y.; Graeser, R.; Warnecke, A.; Kratz, F.; Hauff, P.; Licha, K.; Haag, R. Development of pH-Responsive Core-Shell Nanocarriers for Delivery of Therapeutic and Diagnostic Agents. *Bioorganic Med. Chem. Lett.* **2009**, *19* (3), 1030–1034.

(166) Oishi, M.; Nagasaki, Y. Stimuli-Responsive Smart Nanogels for Cancer Diagnostics and Therapy. *Nanomedicine (Lond).* **2010**, *5* (3), 451–468.

(167) Jae, H. P.; Kwon, S.; Lee, M.; Chung, H.; Kim, J. H.; Kim, Y. S.; Park, R. W.; Kim, I. S.; Sang, B. S.; Kwon, I. C.; Seo, Y. J. Self-Assembled Nanoparticles Based on Glycol Chitosan Bearing Hydrophobic Moieties as Carriers for Doxorubicin: In Vivo Biodistribution and Anti-Tumor Activity. *Biomaterials* **2006**, *27* (1), 119–126.

(168) Blanco, E.; Kessinger, C. W.; Sumer, B. D.; Gao, J. Multifunctional Micellar Nanomedicine for Cancer Therapy. *Exp. Biol. Med.* **2009**, *234* (2), 123–131.

(169) Kim, T. Y.; Kim, D. W.; Chung, J. Y.; Shin, S. G.; Kim, S. C.; Heo, D. S.; Kim, N. K.; Bang, Y. J. Phase I and Pharmacokinetic Study of Genexol-PM, a Cremophor-Free, Polymeric Micelle-Formulated Paclitaxel, in Patients with Advanced Malignancies. *Clin. Cancer Res.* **2004**, *10* (11), 3708–3716.

(170) Tsai, H. C.; Chang, W. H.; Lo, C. L.; Tsai, C. H.; Chang, C. H.; Ou, T. W.; Yen, T. C.; Hsiue, G. H. Graft and Diblock Copolymer Multifunctional Micelles for Cancer Chemotherapy and Imaging. *Biomaterials* **2010**, *31* (8), 2293–2301.

(171) Mohan, P.; Rapoport, N. Doxorubicin as a Molecular Nanotheranostic Agent: Effect of Doxorubicin Encapsulation in Micelles or Nanoemulsions on the Ultrasound-Mediated Intracellular Delivery and Nuclear Trafficking. *Mol. Pharm.* **2010**, *7* (6), 1959–1973.

(172) Cummings, J.; Smyth, J. DNA Topoisomerase I and II as Targets for Rational Design of New Anticancer Drugs. *Ann. Oncol.* **1993**, *4*, 533–543.

(173) Fornari, F. A.; Randolph, J. K.; Yalowich, J. C.; Ritke, M. K.; Gewirtz, D. A. Interference by Doxorubicin with DNA Unwinding in MCF-7 Breast Tumor Cells. *Mol. Pharmacol.* **1994**, *45* (4), 649–656.

(174) Gabizon, A.; Shmeeda, H.; Barenholz, Y. Pharmacokinetics of Pegylated Liposomal Doxorubicin: Review of Animal and Human Studies. *Clinical Pharmacokinetics*. 2003, pp 419–436.

(175) Gabizon, A. A. Liposomal Drug Carrier Systems in Cancer Chemotherapy: Current Status and Future Prospects. *J Drug Target* **2002**, *10* (7), 535–538.

(176) Lorusso, D.; Di Stefano, A.; Carone, V.; Fagotti, A.; Pisconti, S.; Scambia, G. Pegylated Liposomal Doxorubicin-Related Palmar-Plantar Erythrodysesthesia ('hand-Foot' Syndrome). *Annals of Oncology*. 2007, pp 1159–1164.

(177) Izolda, M. D.; Elzbieta, N.; Beata, K. "Hand-Foot" syndrome - after Liposomal Pegylated Doxorubicin in Patients with the Ovarian Cancer Recurrence (Own Experiences). *Ginekol. Pol.* **2008**, *79* (5), 332–337.

(178) Liu, J.; Lee, H.; Allen, C. Formulation of Drugs in Block Copolymer Micelles: Drug Loading and Release. *Curr. Pharm. Des.* **2006**, *12* (36), 4685–4701.

(179) Gao, Z. G.; Fain, H. D.; Rapoport, N. Controlled and Targeted Tumor Chemotherapy by Micellar-Encapsulated Drug and Ultrasound. *J. Control. Release* **2005**, *102* (1), 203–222.

(180) Rapoport, N. Combined Cancer Therapy by Micellar-Encapsulated Drug and Ultrasound. In *International Journal of Pharmaceutics*; 2004; Vol. 277, pp 155–162.

(181) Rapoport, N. Physical Stimuli-Responsive Polymeric Micelles for Anti-Cancer Drug Delivery. *Progress in Polymer Science (Oxford)*. 2007, pp 962–990.

(182) Holliday, D. L.; Speirs, V. Choosing the Right Cell Line for Breast Cancer Research. *Breast Cancer Res.* **2011**, *13*, 215.

(183) Tuzlali, S. Pathology of Breast Cancer. In *Breast Disease: Diagnosis and Pathology*; 2015; Vol. 1, pp 241–266.

(184) Hilger, I.; Hergt, R.; Kaiser, W. A. Use of Magnetic Nanoparticle Heating in the Treatment of Breast Cancer. *IEE Proc Nanobiotechnol* **2005**, *152* (1), 33–39.

(185) Onda, N.; Kemmochi, S.; Morita, R.; Ishihara, Y.; Shibutani, M. In Vivo Imaging of Tissue-Remodeling Activity Involving Infiltration of Macrophages by a Systemically Administered Protease-Activatable Probe in Colon Cancer Tissues. *Transl Oncol* **2013**, *6* (6), 628–637.

(186) Mieog, J. S.; Hutteman, M.; van der Vorst, J. R.; Kuppen, P. J.; Que, I.; Dijkstra, J.; Kaijzel, E. L.; Prins, F.; Lowik, C. W.; Smit, V. T.; van de Velde, C. J.; Vahrmeijer, A. L. Image-Guided Tumor Resection Using Real-Time near-Infrared Fluorescence in a Syngeneic Rat Model of Primary Breast Cancer. *Breast Cancer Res Treat* **2011**, *128* (3), 679–689.

(187) Reubi, J. C. Peptide Receptors as Molecular Targets for Cancer Diagnosis and Therapy. *Endocr. Rev.* **2003**, *24* (4), 389–427.

(188) Tung, C. H.; Bredow, S.; Mahmood, U.; Weissleder, R. Preparation of a Cathepsin D Sensitive near-Infrared Fluorescence Probe for Imaging. *Bioconjug. Chem.* **1999**, *10* (5), 892–896.

(189) Lee, S.; Park, K.; Lee, S. Y.; Ju, H. R.; Jong, W. P.; Hyung, J. A.; Ick, C. K.; Youn, I. C.; Kim, K.; Choi, K. Dark Quenched Matrix Metalloproteinase Fluorogenic Probe for Imaging Osteoarthritis Development in Vivo. *Bioconjug. Chem.* **2008**, *19* (9), 1743–1747.

(190) Bremer, C.; Tung, C. H.; Weissleder, R. In Vivo Molecular Target Assessment of Matrix Metalloproteinase Inhibition.[see Comment]. *Nat. Med.* **2001**, *7* (6), 743–748.

(191) Lee, S. K.; Han, M. S.; Tung, C. H. Layered Nanoprobe for Long-Lasting Fluorescent Cell Label. *Small* **2012**, *8* (21), 3315–3320.

(192) Rakash, S. Role of Proteases in Cancer: A Review. *Biotechnol. Mol. Biol. Rev.* **2012**, *7* (4), 90–101.

(193) Ge, L.; Shenoy, S. K.; Lefkowitz, R. J.; DeFea, K. Constitutive Protease-Activated Receptor-2-Mediated Migration of MDA MB-231 Breast Cancer Cells Requires Both β-Arrestin-1 and -2. *J. Biol. Chem.* **2004**, *279* (53), 55419–55424.

(194) Su, S.; Li, Y.; Luo, Y.; Sheng, Y.; Su, Y.; Padia, R. N.; Pan, Z. K.; Dong, Z.; Huang, S. Proteinase-Activated Receptor 2 Expression in Breast Cancer and Its Role in Breast Cancer Cell Migration. *Oncogene* **2009**, *28* (34), 3047–3057.

(195) Matěj, R.; Manďáková, P.; Netíková, I.; Poučková, P.; Olejár, T. Proteinase-Activated Receptor-2 Expression in Breast Cancer and the Role of Trypsin on Growth and Metabolism of Breast Cancer Cell Line MDA MB-231. *Physiol. Res.* **2007**, *56* (4), 475–484.

(196) Morris, D. R.; Ding, Y.; Ricks, T. K.; Gullapalli, A.; Wolfe, B. L.; Trejo, J. Protease-Activated Receptor-2 Is Essential for Factor VIIa and Xa-Induced Signaling, Migration, and Invasion of Breast Cancer Cells. *Cancer Res.* **2006**, *66* (1), 307–314.

(197) Olsen, J. V; Ong, S.-E.; Mann, M. Trypsin Cleaves Exclusively C-Terminal to Arginine and Lysine Residues. *Mol. Cell. Proteomics* **2004**, *3* (6), 608–614.

(198) Kaszuba, M.; Corbett, J.; Watson, F. M.; Jones, A. High-Concentration Zeta Potential Measurements Using Light-Scattering Techniques. *Philos. Trans. R. Soc. A Math. Phys. Eng. Sci.* **2010**, *368* (1927), 4439–4451.

(199) Wang, P.; Henning, S. M.; Heber, D. Limitations of MTT and MTS-Based Assays for Measurement of Antiproliferative Activity of Green Tea Polyphenols. *PLoS One* **2010**, *5* (4).

(200) Maeda, H. Macromolecular Therapeutics in Cancer Treatment: The EPR Effect and beyond. *Journal of Controlled Release*. 2012, pp 138–144.

(201) Porumb, H. The Solution Spectroscopy of Drugs and the Drug-Nucleic Acid Interactions. *Prog. Biophys. Mol. Biol.* **1979**, *34*, 175–195.

(202) Olson, E. S.; Jiang, T.; Aguilera, T. A.; Nguyen, Q. T.; Ellies, L. G.; Scadeng, M.; Tsien, R. Y. Activatable Cell Penetrating Peptides Linked to Nanoparticles as Dual Probes for in Vivo Fluorescence and MR Imaging of Proteases. *Proc. Natl. Acad. Sci.* **2010**, *107* (9), 4311–4316.

(203) Funovics, M.; Weissleder, R.; Tung, C. H. Protease Sensors for Bioimaging. *Analytical and Bioanalytical Chemistry*. 2003, pp 956–963.

(204) Choi, Y.; Weissleder, R.; Tung, C. H. Selective Antitumor Effect of Novel Protease-Mediated Photodynamic Agent. *Cancer Res.* **2006**, *66* (14), 7225–7229.

(205) Saini, S.; Singh, H.; Bagchi, B. Fluorescence Resonance Energy Transfer (FRET) in Chemistry and Biology: Non-Forster Distance Dependence of the FRET Rate. *J. Chem. Sci.* **2006**, *118* (1), 23–35.

(206) Haver, T. Förster Resonance Energy Transfer. *Chemphyschem A Eur. J. Chem. Phys. Phys. Chem.* **2011**, *12*, 427–434.

(207) Shaikh, H. K.; Kshirsagar, R. V; Patil, S. G. Mathematical Models for Drug Release Chracterization: A Review. *World J. Pharm. Pharm. Sci.* **2015**, *4* (4), 324–338.

(208) Dash, S.; Murthy, P.; Nath, L.; Chowdhury, P. Review Kinetic Modeling On Drug Release From Controlled Drug Delivery Systems. **2010**, *67* (3), 217–223.

(209) Korsmeyer, R. W.; Gurny, R.; Doelker, E.; Buri, P.; Peppas, N. A. Mechanisms of Solute Release from Porous Hydrophilic Polymers. *Int. J. Pharm.* **1983**, *15* (1), 25–35.

(210) Missirlis, D.; Kawamura, R.; Tirelli, N.; Hubbell, J. A. Doxorubicin Encapsulation and Diffusional Release from Stable, Polymeric, Hydrogel Nanoparticles. *Eur. J. Pharm. Sci.* **2006**, *29* (2), 120–129.

(211) Kataoka, K.; Matsumoto, T.; Yokoyama, M.; Okano, T.; Sakurai, Y.; Fukushima, S.; Okamoto, K.; Kwon, G. S. Doxorubicin-Loaded Poly(ethylene Glycol)-Poly(β-Benzyl-L-Aspartate) Copolymer Micelles: Their Pharmaceutical Characteristics and Biological Significance. In *Journal of Controlled Release*; 2000; Vol. 64, pp 143–153.

(212) Moffatt, S.; Cristiano, R.; Boyle, R. Combined Formulation of Doxorubicin-Arg-Gly-Asp (RGD) and Modified PEGylated PLGA-Encapsulated Nanocarrier Improves Anti-Tumor Activity. In *Proceedings - 2012 IEEE International Conference on Bioinformatics and Biomedicine Workshops, BIBMW 2012*; 2012; pp 903–909.

(213) Siddharth, S.; Nayak, A.; Nayak, D.; Bindhani, B. K.; Kundu, C. N. Chitosan-Dextran Sulfate Coated Doxorubicin Loaded PLGA-PVA-Nanoparticles Caused Apoptosis in Doxorubicin Resistance Breast Cancer Cells through Induction of DNA Damage. *Sci. Rep.* **2017**, *7* (1), 2143.

(214) Boyle, J. Lehninger Principles of Biochemistry (4th Ed.): Nelson, D., and Cox, M. *Biochem. Mol. Biol. Educ.* **2005**, *33* (1), 74–75.

(215) Cherukuri, A.; Frye, J.; French, T.; Durack, G.; Voss, E. W. FITC-Poly-D-Lysine Conjugates as Fluorescent Probes to Quantify Hapten- Specific Macrophage Receptor Binding and Uptake Kinetics. *Cytometry* **1998**, *31* (2), 110–124.

(216) Huang, B. X.; Kim, H.-Y.; Dass, C. Probing Three-Dimensional Structure of Bovine Serum Albumin by Chemical Cross-Linking and Mass Spectrometry. *J. Am. Soc. Mass Spectrom.* **2004**, *15* (8), 1237–1247.

(217) Promega Corporation. CellTiter-Blue® Cell Viability Assay Protocol. *Promega.Com* **2013**, 1–15.

(218) Forget, M. a; Desrosiers, R. R.; Béliveau, R. Physiological Roles of Matrix Metalloproteinases: Implications for Tumor Growth and Metastasis. *Can. J. Physiol. Pharmacol.* **1999**, *77* (7), 465–480.

(219) Edwards, J. G.; McLaren, J.; Jones, J. L.; Waller, D. A.; O'Byrne, K. J. Matrix Metalloproteinases 2 and 9 (Gelatinases A and B) Expression in Malignant Mesothelioma and Benign Pleura. *Br. J. Cancer* **2003**, *88* (10), 1553–1559.

(220) Kousidou, O. C.; Roussidis, a E.; Theocharis, a D.; Karamanos, N. K. Expression of MMPs and TIMPs Genes in Human Breast Cancer Epithelial Cells Depends on Cell Culture Conditions and Is Associated with Their Invasive Potential. *Anticancer Res.* **2004**, *24* (6), 4025–4030.

(221) Yao, J.; Xiong, S.; Klos, K.; Nguyen, N.; Grijalva, R.; Li, P.; Yu, D. Multiple Signaling Pathways Involved in Activation of Matrix Metalloproteinase-9 (MMP-9) by Heregulin-beta1 in Human Breast Cancer Cells. *Oncogene* **2001**, *20* (56), 8066–8074.

(222) Edwards, D.; Hoøer-Hansen, G.; Blasi, F.; Sloan, B. F. *The Cancer Degradome: Proteases and Cancer Biology*; 2008.

(223) Popescu, N. C.; King, C. R.; Kraus, M. H. Localization of the Human erbB-2 Gene on Normal and Rearranged Chromosomes 17 to Bands q12-21.32. *Genomics* **1989**, *4* (3), 362–366.

(224) English, D. P.; Roque, D. M.; Santin, A. D. HER2 Expression Beyond Breast Cancer: Therapeutic Implications for Gynecologic Malignancies. *Mol. Diagn. Ther.* **2013**, *17* (2), 85–99.

(225) Wright C., N. S. A. B. S. J. R. C. F. J. C. J. H. A. L. H. C. H. W. Relationship between c-erbB-2 Protein Product Expression and Response to Endocrine Therapy in Advanced Breast Cancer. *Br. J. Cancer* **1992**, *65* (1), 118–121.

(226) Montemurro, F.; Di Cosimo, S.; Arpino, G. Human Epidermal Growth Factor Receptor 2 (her2)-Positive and Hormone Receptor-Positive Breast Cancer: New Insights into Molecular Interactions and Clinical Implications. *Ann. Oncol.* **2013**, *24* (11), 2715–2724.

(227) Ariazi, E. A.; Clark, G. M.; Mertz, J. E. Estrogen-Related Receptor Alpha and Estrogen-Related Receptor Gamma Associate with Unfavorable and Favorable Biomarkers, Respectively, in Human Breast Cancer. *Cancer Res.* **2002**, *62* (22), 6510–6518.

(228) Nahta, R.; Esteva, F. J. HER2 Therapy: Molecular Mechanisms of Trastuzumab Resistance. *Breast Cancer Res.* **2006**, *8* (6), 215.

(229) Santosh, B.; Yadava, P. K.; Santosh, B.; Yadava, P. K. Nucleic Acid Aptamers: Research Tools in Disease Diagnostics and Therapeutics, Nucleic Acid Aptamers: Research Tools in Disease Diagnostics and Therapeutics. *BioMed Res. Int. BioMed Res. Int.* **2014**, *2014*, *2014*, e540451.

(230) Ray, P.; Viles, K. D.; Soule, E. E.; Woodruff, R. S. Application of Aptamers for Targeted Therapeutics. *Arch. Immunol. Ther. Exp. (Warsz).* **2013**, *61* (4), 255–271.

(231) Ng, E. W. M.; Shima, D. T.; Calias, P.; Cunningham, E. T.; Guyer, D. R.; Adamis, A. P. Pegaptanib, a Targeted Anti-VEGF Aptamer for Ocular Vascular Disease. *Nat. Rev. Drug Discov.* **2006**, *5* (2), 123–132.

(232) Krishnamurti, U.; Silverman, J. F. HER2 in Breast Cancer: A Review and Update. *Adv. Anat. Pathol.* **2014**, *21* (2), 100–107.

(233) Garrett, J. T.; Arteaga, C. L. Resistance to HER2-Directed Antibodies and Tyrosine Kinase Inhibitors: Mechanisms and Clinical Implications. *Cancer Biology and Therapy*. 2011, pp 793–800.

(234) Nahta, R.; O'Regan, R. M. Evolving Strategies for Overcoming Resistance to HER2-Directed Therapy: Targeting the PI3K/Akt/mTOR Pathway. *Clin. Breast Cancer* **2010**, *10*, S72–S78.